High Power THz Generation in a GaP waveguide and the THz Carrier Dynamics in Epitaxial Graphene

by

Charles John Divin

A dissertation submitted in partial fulfillment
of the requirements for the degree of
Doctor of Philosophy
(Electrical Engineering)
in The University of Michigan
2009

Doctoral Committee:

Professor Theodore B. Norris, Chair
Professor Roberto Merlin
Professor Herbert G. Winful
Research Scientist John F. Whitaker

To Mary…

Acknowledgements

The work presented in this thesis would not have been possible with the numerous contributions from my colleagues and friends.

I would like to thank my mentor Dr. Theodore Norris for his guidance, inspiration, support, and patience during my time as a graduate student. Ted allowed me to work independently on a wide range of projects, only a few of which made it into this thesis. From quantum mechanics to biosensors, Ted encouraged successful collaborations with others when my own projects reached an impasse. I am immensely grateful for his advice and perpetual optimism during my graduate time.

I would especially like to thank those individuals who have collaborated with me to enhance the strength of my research: Steve Williamson, Dave Zimdars, and everyone else at Picometrix for the multiple THz receivers and their continued technical support. The high power THz generation work would not have been possible without the weeks of laser time donated by Tom Sosnowski at Clark MXR. I would also like to thank Dr. Walt de Heer, Dr. Phillips First and Dr. Claire Berger's group at the Georgia Institute of Technology for providing the graphene samples and scientific support. In addition to providing the theoretical foundation for optical coherent control in graphene, Professor John Sipe and his student Julien Rioux have provided numerous insights and helpful interpretations for our occasionally confusing experimental data.

Thank you also to my committee members, Dr. Herb Winful, Dr. John Whitaker and Dr. Roberto Merlin, for all your contributions and suggestions in the development of my research. I am extremely thankful to my fellow research group members for the often helpful, usually entertaining discussions we've had: Noah Chang, Hyunyong Choi, Malakeh Musheinish, Dong Sun, Yunbo Guo, and Jessica Ames. In particular, I'm deeply indebted to both Noah and Dong for their help during my graduate time. Noah's permanent optimism helped tremendously during my early years, and his later collaboration led directly to the high power THz work and my first successful experiment. As Noah helped with the first half of my research, Dong helped with the second. Dong provided valuable insight into the interpretation of the THz carrier dynamics and was

directly responsible for half of the coherent control work. Without Dong's expertise on the mid-IR optics, I can't image the coherent control would have been as successful as it was. I'd like to wish the new student Pacha and Momchil the best of luck as the take over my work.

I would like to thank my parents, Cherri and Donnie Divin, for your love and encouragement, and showing me the parent I would like to be. I would like to thank my wife Mary for her love, encouragement, and patience through all the long nights, and extended writing. Without her encouragement, I never could have finished. Lastly, I would like to thank my daughter, Emily. Her smiling face means the world to me.

Contents

List of Figures

List of Appendices

Abstract

The generation and detection of ultrafast time domain (TD) THz pulse trains is an active area of research, with recent developments pushing sources to higher power and greater bandwidth. This thesis presents research in two frontiers of the science and technology of THz radiation; the generation of high power TD-THz pulses and the dynamic THz spectroscopy of an emerging new material, epitaxial graphene. To increase the SNR of conventional time domain (TD) THz sources, a novel method is proposed for high average power, high repetition rate, TD-THz generation based on an ultrafast fiber laser and optical rectification inside a GaP waveguide. A model for the THz generation is developed by combining a finite-difference frequency-domain mode solver with the 1D generation equation. The measured 150-μW average power and 3 THz bandwidth represent nearly a two order of magnitude increase over conventional TD-THz systems, and are in good agreement with the theoretical model.

Since the demonstration of the isolation of single atomic sheets of graphite, graphene has received tremendous attention due to its unique mechanical and electrical properties. These unique properties indicate graphene is a highly promising material for high-speed (THz-bandwidth) electronic devices. This thesis presents TD-THz spectroscopy of multilayer epitaxial graphene samples, with the goals of identifying the presence of a possible bandgap opening at low energies and of measuring the hot carrier recovery dynamics on picosecond timescales. The graphene transmission spectrum is shown to be remarkably flat and is used to verify the absence of a bandgap at meV energies. Optical pump – THz probe measurements of the temperature-dependent recovery dynamics show a biexponential recovery with which is compared with theoretical predictions.

Lastly, THz detection of coherent controlled photocurrents is demonstrated for the first time in epitaxial graphene. Optical coherent control provides a method for contactless injection of ultrafast current bursts into semiconductor materials. The associated radiated THz pulse is used to verify the unique polarization independence and power scaling with theoretical predictions. The effect of background hot carriers on the coherent generation process is explored and the dephasing of the coherent current injection is observed for the first time.

Chapter 1
Introduction

In 2008, eighteen major international airports in the United States supplemented their security procedures with mm-wave imaging systems. These systems operate at 94 GHz using arrays of emitters and detectors to create a full three dimensional image of the subject [1, 2]. While the first generation devices caused an uproar among privacy groups, the imagers represented a significant milestone for far infrared (far-IR) imaging applications [3, 4]. Unfortunately, the system's long wavelength and narrow bandwidth limits the image resolution and prevents spectroscopic identification of materials. Ideally, one would like to use broadband illumination at a shorter wavelength which would allow a high resolution reconstruction with full far-IR spectroscopic information. Such a system would greatly improve the ability to identify small concealed regions of interest.

Time domain terahertz (TD-THz) systems are able to meet both of these requirements. Typical systems are able to generate and detect broadband pulses with wavelengths between 100 μm and 2,000 μm and, using coherent detection techniques, are able to achieve signal to noise ratios (SNR) in excess of 60 dB [5, 6]. Unfortunately, this sensitivity is only achieved in a confocal geometry. In order to achieve a similar sensitivity at 1 THz in a backscatter configurative, either the emitter density or the emitter power would need to increase 1,000 fold from an average power of 1 μW to 1 mW [7]. Beyond imaging, a high power TD-THz system would benefit spectroscopy and sensing applications by allowing for faster acquisition time at current SNRs, or greatly improved SNR at current acquisition times. In particular, the improved SNR would greatly benefit spectroscopic applications involving thin or weakly absorbing materials.

One particularly interesting area requiring high SNR THz spectroscopy is in the characterization of single atomic layers of graphite. Graphite is a carbon allotrope where the carbon atoms are arranged into a stack of flat 2D sheets with the atoms arranged into a hexagonal honeycomb lattice within each sheet. Since the isolation of high quality

individual sheets in 2004, single- and few-layer samples have received tremendous attention due to their unique electrical and mechanical properties. The high carrier mobility, excellent thermal conductivity [8], and long ballistic lifetime [9] in epitaxial graphene offer interesting new opportunities for ballistic THz resonators, ballistic field effect transistors, *pn*-junction diodes, and other high speed electronics [10, 11]. However, the performance of many of these devices depends heavily on two factors. First, high speed devices will require knowledge of carrier conductivity at THz frequencies. Second, the performance of photosensors, FETs, and other devices is critically dependent on the behavior of hot carriers and the subsequent cooling and recombination dynamics. Measurement techniques, such as optical transmission and reflection, have the temporal resolution necessary for measuring the carrier behavior on picoseconds timescales and faster, however they are only able to measure changes in heavily doped layers or the effect of very energetic carriers. On the other hand, TD-THz spectroscopy is extremely well suited to measuring changes in the conductivity of thin films, and a high power TD-THz spectroscopy system would provide an ideal tool for measuring the ultrafast carrier dynamics in graphene. In addition to standard THz spectroscopy, this thesis explores a method for optically generating ballistic photocurrents, which can provide further insight into the dephasing and scattering rates in epitaxial graphene.

History of Optical Rectification and Time Domain THz Generation

The origin of optical rectification can be traced to the development of the laser, which offered tremendous improvements in spatial and temporal coherence over contemporary light sources, allowing focused intensities far surpassing anything before. Further refinements and new techniques such as modelocking and chirped pulse amplification led to ever shorter and more intense optical pulses, enabling the study of nonlinear physical and chemical interactions on extremely short time scales. However even before these developments, the field of nonlinear optics was already well established.

In 1961, Franken et al. observed the second optical harmonic of a ruby laser beam incident on a quartz crystal [12]. The following year, the first optical rectification experiment was performed by Bass et al. in a KDP crystal with a ruby laser [13]. As the available laser pulse durations shrank, higher and higher frequencies were generated

through optical rectification. In 1971, Yang et al. generated several picoseconds microwave pulses by focusing 2 ps pulses from a Nd:glass mode-locked laser into a lithium niobate ($LiNbO_3$) crystal [14]. The crystal was phase-matched for optical rectification, and using an FTIR setup, they reported peaks in the power spectrum for this sample at 75, 195, and 315 GHz. In 1984, Auston and co-workers generated true THz bandwidth pulses via Cherenkov waves in a lithium tantalate ($LiTaO_3$) crystal which was pumped with 100 fs pulses from a ring mode-locked dye laser [15].

During this time, the low average power and low photon energy prevented absolute measurements of the THz pulse train. Improvements were quantified by measuring the signal increase relative to older techniques [16, 17]. This method of measurement emphasizes power-on-detector rather than the intrinsic power generation of a method. While the detected power is arguably more useful, it is much more dependent on experimental variables. Differences between experimental setups can range from the unintentional, such as collection and focusing optics, to the deliberate, such as tailoring the detector response to match a proposed generation scheme. However further advancements in both the laser pump systems and the generation techniques improved the THz power, and by the late 1980's the power had increased to the point where it could be measured absolutely using common incoherent detectors. During this time, the average power had increased from nearly undetectable pW to μW levels [18] for high repetition rate systems, and the pulse energy has increased from fJ to sub-μJ for low repetition rate systems [19]. This enabled more quantitative comparison between generation schemes using cryogenic bolometers for high average power and pyroelectric detectors for high pulse energy systems.

Over the past 10 years, the THz power scaling has closely followed improvements to the pump lasers. A conventional photoconductive emitter which is pumped by a Ti:sapphire oscillator typically achieves an average power on the order of 1 μW [20]. Further average power scaling is significantly impeded by saturation effects at low repetition rates, and thermal dissipation of the pump at higher repetition rates [21]. In contrast, optical rectification of a femtosecond pulse train in a nonlinear crystal offers

much better THz power scalability [22-25]. To understand the direction of future power scaling, it's helpful to look at the basic power scaling relationship:

$$P_{THz} \propto N_{rr}\, z_L^2\, d_{eff}^2\, I_{pump}^2 \tag{1.1}$$

where d_{eff} is the nonlinear coefficient, z_L is pump/THz interaction length with the crystal, N_{rr} is the laser repetition rate, and I_{pump} is the laser pulse intensity.

One approach for THz power scaling is to scale the pump laser to very low repetition rates and very high pulse energies. In this scheme, the average pump power is held constant, $I_{pump} = 1/N_{rr}$, which leads to an overall inverse relationship with the system repetition rate. This method has proven very successful at generating high average power THz pulses, however the low repetition rate prevents the use of many common noise reduction techniques [26]. In this thesis, I will focus on a technique that scales primarily by using a high-power, high-repetition-rate, pump laser in conjunction with long crystals. By focusing on a system with a high repetition rate, we maintain the ability to use mature noise reduction techniques so that the system SNR scales with increasing power.

Graphene Fabrication Methods

One of the primary reasons for the tremendous attention focused on graphene is due to the unique electronic properties of individual sheets. One of the most interesting aspects of graphene is that at low energies, the charge carriers behave as massless, chiral, Dirac fermions [27]. This dispersion relationship is formally equivalent to many of the relationships in quantum electrodynamics (QED) with the exception that the carriers move 300 times slower than the speed of light. This allows testing of the fundamental theory [28] as well as new physical phenomena such as integer quantum Hall effect [29].

Perhaps the most interesting feature for future THz devices is represented in the Klien paradox; whereby Dirac fermions are insensitive to external electrostatic potentials, i.e. impurities, and long range scattering is suppressed. This leads to long range ballistic travel similar to carbon nanotubes, with early samples reporting ballistic lengths in excess of several microns with corresponding ballistic lifetimes in excess several picoseconds [30]. Ballistic transport can be exploited to create field effect devices [31-33] and micron

sized THz resonators [34, 35]. Furthermore, recent advances in anisotropic etching have allowed the creation of graphene nano-ribbons with crystallographic edges [36], where the conduction properties depend on the edge shape [37]. Although graphene development is still in its infancy, the potential for new and exciting THz devices is immense.

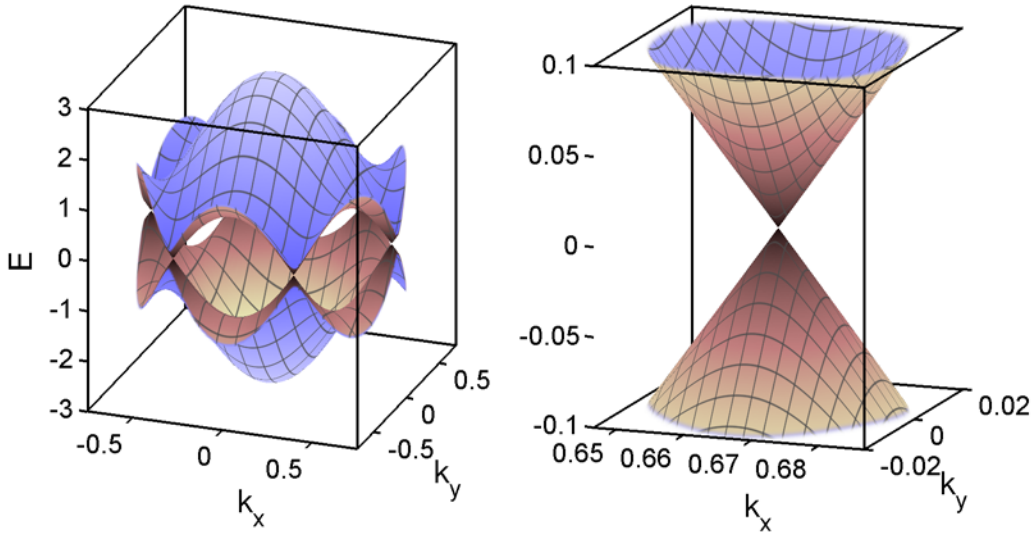

Figure 1.1 shows the energy spectrum of graphene in units of eV and the inverse lattice constant, $1/a$. The right panel shows a magnified view around the Dirac point.

In the conventional tight binding model, the electron dispersion relationship is given by:

$$E = \pm\sqrt{\gamma_0^2\left(1 + 4\cos^2\pi k_y a + 4\cos\pi k_y a \cdot \cos\pi k_x\sqrt{3}a\right)} \tag{1.2}$$

with the nearest-neighbor hopping energy $\gamma_0 \approx 2.8$ eV and the lattice separation $a \approx 2.4$ Å, with positive sign for the conduction band and negative for the valence band, as shown in Figure 1.1. The above equation leads to the conduction and valence band touching at 6 points in K space, which are referred to as the Dirac points. At wavenumbers in the vicinity of the of the Dirac points, the dispersion is linear and simplifies to

$$E = \pm v_F|\boldsymbol{k}_\Delta| \tag{1.3}$$

where $\mathbf{k}_\Delta$ is the wavevector relative to the Dirac point, and v_F is the energy independent Fermi velocity and is typically ~10^8 cm/s in high quality samples. When discussing the linear dispersion of graphene, one implicitly assumes the momentum is measured relative to the Dirac point, and for simplicity, the Δ subscript is dropped. With the tight binding model, further relationships can be derived such as the density of states, electron heat capacity, and conductivity. These relationships will be presented in further detail in Chapter 3.

Despite the relatively recent isolation of high quality samples, graphene has been a theoretical curiosity for nearly 70 years [27], and an unintended byproduct of daily human activity for much longer. The production of small graphene flakes is as trivial as drawing with a pencil; however, the challenge lies in isolating and identifying these monolayer flakes among the larger population of debris.

There are several methods for fabricating graphene: exfoliate separation, chemically-derived, chemical vapor deposition (CVD), and epitaxial growth. Perhaps best known as the original and simplest methods for high quality fabrication, exfoliate graphene is a simple method that involves the mechanical separation of individual graphene layers from bulk graphite. In the original method [30], flakes from a synthetic highly ordered pyrolytic graphite sample are mechanically rubbed against a Si wafer with a 300 nm SiO_2 overcoat. The overcoat allows regions with few and monolayer thickness to be identified visually thorough a microscope due to interference effects between the graphite layers and the substrate. Suspected monolayer flakes can then be verified by unique Raman spectra for monolayer and multilayer stacks. At present, the micromechanical method is capable of producing high quality but irregular samples up to 100 μm is diameter.

Prior to the success of mechanical separation, researchers met partial success using chemical methods. One method used the intercalation of external molecules in between the graphene layers [38]. For large molecules the layers become electrically separated and behave as isolated layers in a larger 3D metamaterial. Unfortunately, the intercalation compounds sufficiently perturb the graphene to destroy most of the interesting electrical properties. Subsequent removal of the intercalation compound yields an interesting graphitic sludge, however the uncontrolled nature of the resulting

compound has prevented significant interest. Alternatively, graphene can be visualized as the limiting case of an infinitely large polycyclic aromatic hydrocarbon (PAH). To this end, chemists have synthesized PAHs with 60, 78, 120 and 222 carbon atoms [39], which resemble graphene 'dots.' UV absorbance spectra from the smaller three show a discrete PAH electronic structure, but the larger 222 atom PAH has Raman bands similar to those in graphite.

An alternative to the problem of isolating pristine graphene sheets among massive debris is to carefully grow sheets in a controlled environment free of contaminants. Recently researchers have tried to adapt the mature chemical vapor deposition (CVD) technique for nanotube growth to graphene [40-42]. In this method, few layers graphene samples are grown via ambient pressure methane-based CVD on polycrystalline Ni films on quartz substrates. Researchers have been able to demonstrate the growth of continuous films across large substrates (~cm^2). Subsequent etching of the Ni layer allows transfer of the graphene films to nonspecific substrates. At the moment, CVD is a promising method for graphene fabrication however samples show higher than expected optical absorption [43].

The most promising method for high quality graphene fabrication is epitaxial growth on single crystal silicon carbide. In this method, ultrapure SiC crystals are hydrogen etched to remove surface impurities and the cleaned crystals are heated in a vacuum furnace above 1300 °C. Under these conditions, Si atoms desorb from the surface which allows the remaining carbon rich region to form graphene layers. Interestingly, multilayer epitaxial graphene samples have a unique rotational stacking between the layers that electronically decouples the layers.

Epitaxial Graphene

Epitaxial growth of carbon monolayers on catalytic surfaces was demonstrated as early as 1974 [44]. Early processes were based on the catalytic decomposition of hydrocarbons (typically methane) on metal surfaces (Ni, Ru, Ir) [45]. At high temperatures, the hydrogen and oxygen atoms desorb from the surface and the remaining carbon forms a graphene monolayer. Early samples showed electronic states different

from bulk graphite and intercalated graphite compounds. Pure metal substrates showed significant charge transfer arising from the work function difference at the graphene-metal interface. Other surfaces such as Ti-terminated TiC (111) [46] and SiC [47] showed the band structure of the graphite monolayer was modified primarily through orbital hybridization of the graphene monolayer and the catalytic substrate.

The interest in epitaxial graphene grew tremendously when high quality samples with excellent electronic properties were demonstrated on SiC substrates [10] in early 2004. Upon heating of cleaved, cleaned, polished, and etched SiC substrates, Si atoms desorb from the crystal lattice, and the carbon rich film assembles in to graphene sheets with several micron sized grains [48]. The number of layers and layer quality can be controlled by the heating time, temperature and crystal face. Graphene samples grown on initially carbon terminated substrates produce thin stacks with few layers and low mobility, while samples grown on Si terminated substrates produced thicker stacks with higher mobility. On both sides, the very first graphene layer is tightly bonded to the SiC substrate with a covalent bond length slightly larger than diamond (1.65 Å vs. 1.54 Å). This buffer layer exhibits strong out of plane warping and unfavorable electrical properties, but helps to shield higher layers. The next layer sits 3.1 Å above the buffer layer which is in good agreement with the weaker van der Waals bonding seen in bulk graphite [49]. This layer which is highly doped with electrons from the SiC graphene interface exhibits excellent electric properties and is commonly referred to as the 'first' graphene layer. Despite the existence of multiple graphene layers there is strong evidence that epitaxial graphene grown on SiC substrates maintains the electronic properties of isolated graphene sheets.

At first glance, one would expect thick graphene stacks grown on SiC substrates to behave similar to thin film graphite samples grown via other methods. However experimental evidence has shown that the layers remain electrically isolated, with each layer maintaining the properties of an isolated graphene sheet. This fortunate coincidence arises from a unique interaction between the graphene lattice and the atomic spacing in the SiC substrate. In bulk graphite, the layers are arranged on top of one another with each layer offset by $\sqrt{3}\boldsymbol{a_0} \times \sqrt{3}\boldsymbol{a_1}$, where $\mathbf{a_0}$ and $\mathbf{a_1}$ are the unit vectors in

graphene plane. This thermodynamically preferable arrangement leads to ABABA… stacking and is referred to as Bernal stacking. However in epitaxial graphene, the slightly 0.14% smaller SiC substrate leads to a new thermodynamically preferable stacking arrangement with a 30° ± 2.2° rotation (R30/R2), relative to the SiC substrate. This leads to a larger rotated 13×13 graphene cell that is commensurate with the underlying SiC in addition to other graphene layers. The larger graphene 'fault cell' is shown in Figure 1.2a, along with normal and high resolution STM images of C-face epitaxial graphene samples.

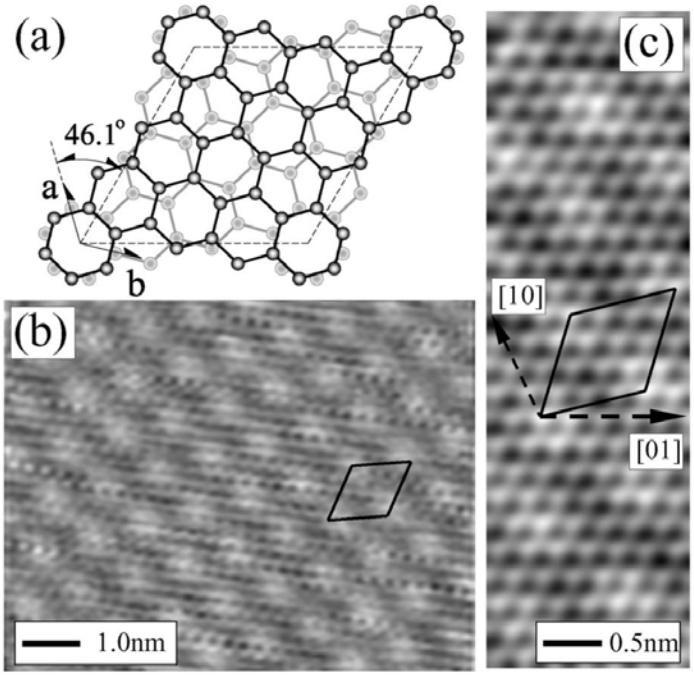

Figure 1.2 shows the layer orientation of multilayer epitaxial graphene, including the 'fault cell' and rotational stacking. A diagram of the larger 'fault pair' unit cell illustrates the rotation between adjacent layers (a). Normal (b) and high resolution (c) STM images of C-face epitaxial graphene samples with the unit cell in black, and the graphene unit vector **a** and **b** indicated by the dashed arrows. (from Hass et. al. [50])

In high quality films with the R30/R2 rotational stacking, the electronic properties differ significantly from bulk graphite with Bernal stacking. In the rotational fault stacking, only 2 out of 52 per unit cell have a high degree of interlayer symmetry which leads to a much weaker electronic interlayer coupling. Ab initio calculations of the band structure for three forms of graphene were performed by Hass et. al. and are shown in Figure 1.3. Both the single layer graphene and the rotational fault bilayer show the linear band structure associated with single sheet graphene, with subtle differences only

appearing at large energies. In contrast, the AB bilayer exhibits touching parabolic bands and secondary bands appearing a few hundred meV above the primary bands in good agreement with tight binding calculations [51].

One significant difference between epitaxial graphene stacks and isolated graphene sheets is an extrinsic charge density originating from the SiC interface [52]. The large work function difference between the SiC substrate and the graphene stack leads to a significant charge transfer into the stack with a layer dependent charge density. Early magnetoresistant measurements indicated a charge density of 3.8×10^{12} electrons/cm^2 in the first graphene layer above the buffer layer [53], while Landau level spectroscopy measured a charge density of 1.5×10^{10} cm^{-2} in the top lightly doped layers [54, 55]. Recently, the doping profile of the first several layers has been measured using mid-IR pump-probe spectroscopy. These measurements show an exponential like doping profile that asymptotically approaches the lightly doped density, with a 1.7 layer charge-density screening length. Prior mid-IR pump-probe experiments have measured the Fermi level of the bottom four layers at 365 meV, 220 meV, 140 meV, and 93 meV relative to the Dirac point.

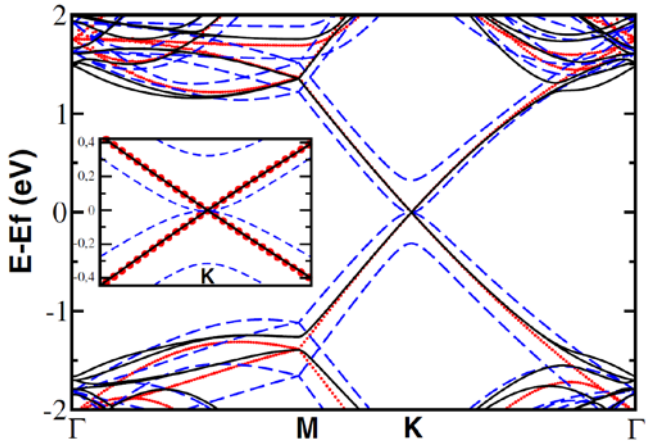

Figure 1.3 shows the calculated band structure for an isolated graphene sheet (red dots), graphene bilayer with Bernal stacking (blue dashed lines) and a bilayer with R30/R2 stacking (solid black lines). (from Hass et. al. [50])

Dissertation Outline

In chapter 2, I examine the challenges in scaling current TD-THz systems to high repetition rate and high average power. I present a system based on optical rectification

in a low-loss phase-matched crystal, gallium phosphide. In order to improve the spatial overlap and interaction length between the diverging THz and the optical pump, a novel air clad waveguide geometry is proposed where the high permittivity of the GaP crystal is used to confine generated THz while allowing pseudo-free-space propagation of the optical pump beam. Confinement of the THz modifies the propagation by introducing several forms of dispersion: modal, waveguide, polarization. A theoretical model for the THz generation is derived by combining the 1D generation equation with a numerical FDFD simulator which calculates the modes and propagation constants for the GaP waveguide. The theoretical model is confirmed by measuring the power generated in two 6 mm long GaP waveguide with rectangular cross sections using a high average power fiber laser, and the generated waveforms and their spectra are shown to be in good agreement with the model.

Chapter 3 focuses on exploring the direct and differential transmission of epitaxial graphene samples in the THz region. Further background information on our graphene samples is provided and a few basic models for the temperature dependent transmission and reflection are provided. Experimentally, both the graphene transmission and differential transmission are shown to be remarkably flat and are used to verify the absence of a bandgap at meV energies. Measurements of the recovery dynamics and nonlinear transmission threshold are presented along with a comparison to several cooling models.

In chapter 4, we demonstrate coherent control of photocurrents in epitaxial graphene. By interfering a fundamental (ω) and second harmonic (2ω) beam on the graphene sample, photoexcited carriers are given a controllable net average momentum, giving rise to a macroscopic current. The ultrafast coherent current radiates a THz pulse which is then used to verify the theoretical power scaling and polarization relationship between the ω, 2ω, and coherent current. An optical prepulse is introduced to investigate the effect background hot carriers and estimates of the dephasing contribution are determined.

Final conclusions and future work are presented in Chapter 5. Following the chapter, Appendices A–F provide a record of commonly used calibration and measurement techniques used in the THz spectroscopy setup.

Chapter 2
Broadband Terahertz Generation in GaP waveguides

Time-domain terahertz (TD-THz) methods using single- or few-cycle THz pulses have found promising applications in spectroscopy, imaging, and sensing [56, 57]. The use of broadband THz pulse trains in a TD-THz system enables time-gated coherent detection, which offers sensitivity orders of magnitude higher than the incoherent detection of narrowband THz [58]. However, the lack of high power broadband THz sources has hampered the development of convenient and versatile TD-THz systems for many applications. A high power THz source will improve both the signal-to-noise ratio (SNR) and the dynamic range of imaging and sensing systems by providing the capability to penetrate deeper into strongly scattering or absorbing materials. Furthermore, high power THz sources promise to drastically reduce the data acquisition time at current SNR, which opens up the possibility for real-time imaging of objects.

Present TD-THz emitters exploit either a current surge in a photoconductive antenna or optical rectification in a nonlinear optical crystal. A conventional photoconductive emitter which is pumped by a Ti:sapphire oscillator can only achieve an average power on the order of 1 μW [20]. Further average power scaling is significantly impeded by thermal effects due to the absorbed pump power [21]. In contrast, optical rectification of a femtosecond pulse train in a nonlinear crystal offers much better THz power scalability [22-25].

Both of the aforementioned THz generation methods are based on the conversion of an ultrafast optical pulse into a THz pulse. For the past ten years, this has been accomplished most readily using solid-state Ti:sapphire laser systems and tailoring THz generation devices to the characteristics of these lasers [22-24]. In recent years, the rapid advancement of ultrafast fiber lasers has motivated efforts to incorporate them into TD-THz systems [25, 59-63]. Due to their advantages over solid-state lasers, such as high wall-plug efficiency, diffraction-limited beam quality, compactness, robustness, and

superior heat dissipation due to the large surface-to-volume ratio of a fiber, ultrafast fiber amplifiers operate at much higher average power levels than can be implemented in the Ti:sapphire system [64]. In this chapter I will describe a system that uses the inherent power scaling of fiber lasers to achieve a high-power, high repetition rate, time domain THz system with a 100 fold power increase over conventional systems

Electrooptic Detection

Before beginning with THz generation, we need to look at the arguably more difficult task of coherent THz detection. One of the primary methods for measuring the temporal shape of propagating THz fields is through free space electrooptic sampling (FS-EOS). This method uses the linear electrooptic effect to rotate the polarization of an ultrafast probe beam in proportion to the instantaneous THz field. Using a differential intensity technique, the induced ellipticity in the probe beam and hence the instantaneous THz field can be measured with high precision. By scanning the relative delay between the THz and optical pulses, the complete THz waveform can be sequentially sampled.

The relationship between the THz field and the differential probe intensity can be derived by beginning with the index ellipsoid equation. In crystals belonging to the $\bar{4}3m$ point group, such as ZnTe and GaP, the equation for the index ellipsoid is given by:

$$\frac{x^2 + y^2 + z^2}{n^2} + 2r_{41}\left(yzE_z + xzE_y + xyE_z\right) = 1 \tag{2.1}$$

Following the notation of Planken [65], it can be shown that a pair of coordinate transforms can recast the index ellipsoid in a rotated coordinate system. For optical beam propagating along the (110) crystal direction and polarized at an angle ϕ with respect to the (001) axis, as shown in Figure 2.1, the THz induced birefringence is:

$$\begin{aligned} n_{y''}(\alpha) &\approx n + \frac{n^3}{2} E_{THz} r_{41} [\cos\alpha \sin^2\theta + \cos(\alpha + 2\theta)], \\ n_{z''}(\alpha) &\approx n + \frac{n^3}{2} E_{THz} r_{41} [\cos\alpha \cos^2\theta - \cos(\alpha + 2\theta)] \\ 2\theta &= -\arctan(2\tan\alpha) \end{aligned} \tag{2.2}$$

where $n_{y''}$ and $n_{z''}$ are the indices of refraction in the new coordinate system, and α is the angle between the THz electric field and the crystal (001) axis. For ZnTe, the index of refraction (n) and the linear electrooptic coefficient (r_{41}) are approximately 2.79 and 4 pm/V.

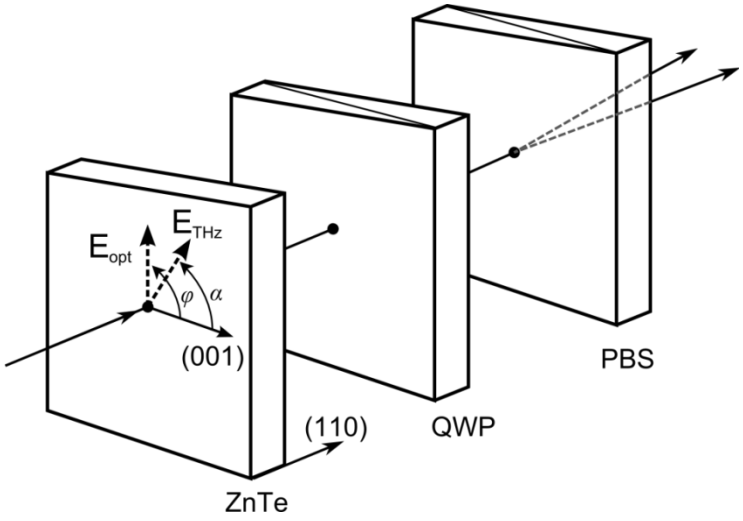

Figure 2.1 Free space electrooptic sampling setup. An ultrafast optical pulse and THz pulse copropagate through a ZnTe crystal. The induced ellipticity in the optical pulse is measured using a quarter wave plate (QWP), a polarizing beam splitter (PBS), and a pair of differential photodiodes (not shown).

As the optical probe beam copropagates with the THz beam inside the detection crystal, the probe beam acquires an elliptical polarization due to the THz induced birefringence. In a standard balanced electrooptic detection setup, the optical beam is polarized at 45° to the THz induced birefringent axes. As the beam propagates, the acquired ellipticity is measured by passing the probe beam through a quarter wave plate and a polarizing beam splitter. The difference in the intensity between the horizontal and vertical polarizations is detected using a pair of photodiodes and the differential intensity is given by,

$$\frac{\Delta \mathrm{I}(\alpha)}{\mathrm{I_p}} \approx \left(\frac{2\pi}{\lambda}\right) n^3 E_{THz} r_{41} L(\cos\alpha \sin 2\varphi + 2\sin\alpha \cos 2\varphi) \tag{2.3}$$

The electrooptic sensitivity is maximized when the THz is polarized along the $(1\bar{1}1)$ axis, $\alpha = 90°$, and the optical beam is either co-polarized or orthogonal to the THz polarization, $\varphi = 0°, 90°$.

If the (100) crystal axis is known, the THz polarization state can be measured by a 90° rotation of the ZnTe crystal and probe beam. For example, with the probe beam aligned to the (100) axis, the probe is only sensitive to the orthogonal component of the THz field, $\varphi = 0 \ \therefore \Delta I \propto \sin\alpha$. By rotating the probe beam in step with the crystal, the time dependent polarization, $\vec{E}_{THz}(\alpha, t)$, can be mapped out. This method works well for strong signals, but the non-negligible birefringence inherent in commercial ZnTe crystals can complicate the rotation procedure.

THz Generation via Optical Rectification

Like many nonlinear systems, it is difficult to fully and accurately model optical rectification (OR) without simplifying assumptions. In general, simple and tractable solutions exist if one neglects either spatial or temporal dispersion, or assumes a simplified relationship between them. For example, in isotropic media with simple non-dissipative, Lorentz-form dispersion relationship, one can calculate the effective Cherenkov radiation modes. The radiated THz field can then be determined by spatially convolving these modes with the optical pulse [66]. Alternatively, one can neglect diffraction and begin with the one dimensional wave equation, which allows for more realistic material dispersion.

For ZnTe, GaP, and other zincblende crystals, the same strong nonlinearities that make these crystals attractive electrooptic materials also make them effective crystals for optical rectification. For these crystals, the optimal generation occurs when the optical beam is polarized along the $(\bar{1}11)$ direction and propagates along the (110) axis. In this geometry, the nonlinear polarization is copolarized with the optical beam and the effective nonlinear optical coefficient is $d_{eff} = \frac{2}{\sqrt{3}} d_{14}$. For GaP at 1.06 μm and ZnTe at 800 nm, the nonlinear optical coefficients are $d_{14}/\epsilon_0 = 70$ pm/V and 60 pm/V, respectively [67].

Modeling optical rectification begins with the one dimensional wave equation:

$$\frac{\partial^2 E(z,t)}{\partial z^2} - \epsilon\mu \frac{\partial^2 E(z,t)}{\partial t^2} - \mu\sigma \frac{\partial E(z,t)}{\partial t} = \mu \frac{\partial^2}{\partial t^2}(P_{NL}) \,. \tag{2.4}$$

Here, E is the combined field from the optical and THz waves, $E(z,t) = E_o(z,t) + E_T(z,t)$. The material permeability, permittivity and conductivity are represented by μ, ε, and σ, respectively. For experimental conditions to date, the optical field is much larger than the THz field so that the nonlinear polarization can be approximated as $P_{NL} \approx 2d_{eff}\,|E_o(z,t)|^2$.

Applying the slowly varying envelope approximation to the optical beam, the time domain field can be expressed as the product of an envelope function, $e_L(z,t)$, and a carrier wave, $\exp(-i\omega_0 t)$ with the following Fourier transform relationships,

$$e_L(z,t) = \int E_L(z,\omega)\, exp(ik(\omega+\omega_0)z - i\omega t)\, \mathrm{d}\omega \tag{2.5}$$

$$E_T(z,t) = \int E_T(z,\omega_T)\, exp(ik(\omega_T)z - i\omega_T t)\, \mathrm{d}\omega_T \tag{2.6}$$

It is important to note that the wavevectors, $k(\omega)$, in the above equations are the true material- and frequency-dependent wavevectors. Substituting into equation 2.4, the one dimensional equation describing the evolution of the THz field is,

$$\begin{aligned}\frac{\partial}{\partial z}E_T(z,\omega_T) = & -\frac{\alpha_T}{2}E_T(z,\omega_t) + \\ & i\frac{\mu d_{eff}\,\omega_T^2}{2k(\omega_T)}\int E_o(z,\omega+\omega_T)E_o^*(z,\omega)\, exp(i\Delta k_T z)\, \mathrm{d}\omega\end{aligned} \tag{2.7}$$

Where the phase mismatch is given by, $\Delta k_T = k(\omega+\omega_0+\omega_T) - k(\omega+\omega_0) - k(\omega_T)$, and the THz *power loss* is given by α_T. If the initial optical power is low enough that other nonlinear processes can be ignored, the above equation integrates to

$$E_T(z,\omega_T) = i\frac{\mu d_{eff}\,\omega_T^2}{2k(\omega_T)}\int \frac{E_o(\omega+\omega_T)E_o^*(\omega)\left(e^{(i\Delta k_T-\alpha_o)z} - e^{-\alpha_T z/2}\right)}{\left(\frac{\alpha_T}{2}\right) - \alpha_o + i\Delta k_T}\,\mathrm{d}\omega \tag{2.8}$$

assuming pump spectrum is constant, $E_o(\omega) \equiv E_o(z=0,\omega)$, and zero initial THz field, $E_T(z=0,\omega_T) = 0$. For thin crystals or select media where the phase mismatch is minimal and the THz absorption can be neglected, the above equation can be further simplified to,

$$E_T(z,\omega_t) = i\frac{\mu c d_{eff}\,\omega_T z}{2n(\omega_T)}\int E_o(\omega+\omega_T)E_o^*(\omega)\;\mathrm{d}\omega \tag{2.9}$$

In the limiting case of materials with negligible THz dispersion, the index of refraction dependence is constant and the above equation can be Fourier transformed to the equation below.

$$E_T(z,t) = -\frac{\mu c d_{eff}\,z}{2n_T}\cdot\frac{\partial}{\partial t}|e_o(t)|^2 \tag{2.10}$$

In its simplest form, the one dimensional generation equation shows us that the THz field is proportional to the derivative of the optical pulse envelope. This form only applies to very thin crystals or rarified gasses where the phase mismatch and absorption are negligible.

The advantage of using optical rectification is the inherent power scalability of the approach. Since optical rectification is a non-resonant phenomenon, the bandwidth is not constrained by material response or saturation. Likewise, many potential crystals have minimal optical absorption and easy heat dissipation which allows for significant power scaling through increases in the average power of the pump. However, increasing the pump average power from a few watts to ten or one hundred watts requires transitioning from Ti:sapphire lasers to Yb-doped fiber systems. As we switch to a 1 μm laser system, GaP has been theoretically demonstrated to be the optimal optical rectification crystal. GaP offers many advantages over ZnTe, such as a broad velocity-matching bandwidth, absence of two-photon absorption at the pump wavelength, and negligible nonlinear refractive index effect [68].

It is well known that efficient THz generation via optical rectification can be described as difference frequency generation within the optical pulse, which requires the group velocity of the optical pump pulse to match the terahertz phase velocity. Figure 2.2a shows the frequency dependent refractive index profiles for ZnTe and GaP with the Sellmeier coefficients taken from Palik, 1991 [69]. The much flatter index curve of GaP compared to that of ZnTe indicates a broader velocity-matching bandwidth and a smaller dispersion. This broader velocity-matching bandwidth allows the generation of single-

cycle THz pulses in GaP while ZnTe tends to emit multi-cycle THz pulses, as shown in Figure 2.2b. The inset plot shows the amplitude spectrum for each pulse. The unexpectedly larger bandwidth in ZnTe is due to a drastically shorter pump pulse. On the other hand, the GaP system is currently limited by the pump pulse duration. As fiber laser technology matures, one would expect the pump pulses available at 1.0 μm to improve and the GaP signal should increase accordingly. Meanwhile, the smaller dispersion permits the distortionless propagation of THz pulses within the crystal, which combined with the broad velocity-matching bandwidth implies potential THz power scaling using a thicker crystal.

As we scale to thicker crystals, it is useful to examine the limits of the one dimensional equation derived above (Eq 2.8). One of the primary limitations of the equation is the assumption of diffractionless propagation. A simulation of this behavior is shown in Figure 2.3. Assuming a Gaussian pump beam and diffractionless generation in GaP, the average THz field as a function of radial distance and crystal length is shown in green. For short crystals, the on-axis intensity grows quadratically as expected. Eventually phase matching constricts the bandwidth and the average power peaks at ~1cm. Beyond this length, spectral loss outpaces any gain over the remaining phase-matched bandwidth. Since the beam is diffractionless, the waist or 86% encircled power remains constant with propagation.

Alternatively, one can accurately model the diffraction in a dispersive media using Cherenkov waves [66]. A simulation based on Cherenkov waves is shown by the blue curves in Figure 2.3. This simulation assumes identical experimental conditions with the exception of material dispersion. In place of the true material dispersion, a simpler Lorentz model was assumed that accurately modeled the material response below 2 THz. With short crystals, the Cherenkov model agrees with the one dimensional simulation; however beyond 1 mm the models diverge rapidly with the Cherenkov model converging to the typical cone wavefront. Since the velocity mismatch in GaP is less than 2%, the cone angle is extremely shallow, and the typical $1/r$ field dependence is not obvious. As would be expected the models begin to diverge at the Rayleigh range for the spectral peak wavelength.

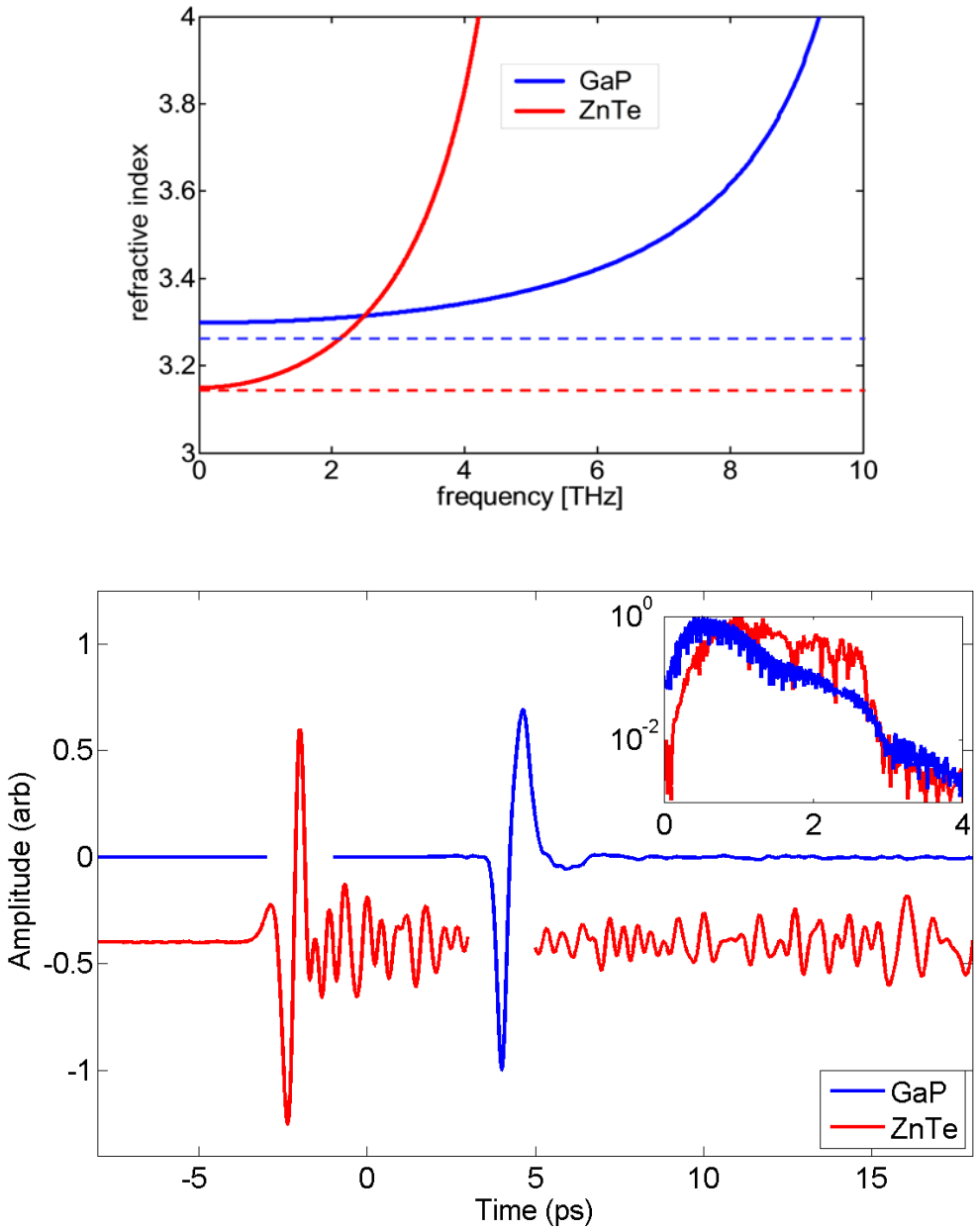

Figure 2.2 shows the index mismatch and waveforms for ZnTe and GaP. The top panel shows the phase mismatch between the THz phase index (solid) and the optical group index (dashed) for ZnTe at 800 nm and for GaP at 1.064 μm, respectivly. b) Typical waveforms from 1 mm ZnTe and GaP, pumped by 65 fs and 200 fs optical pulses, respectively.

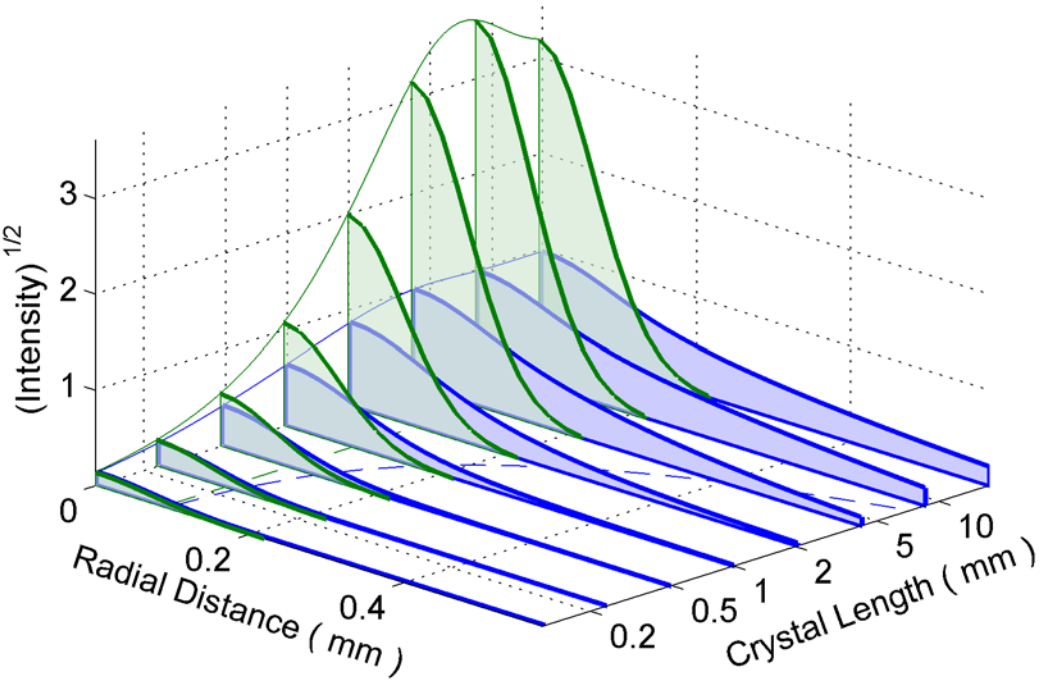

Figure 2.3 compares the results from 1+2D calculation (green) and a true 3D simulation based on Cherenkov waves (blue). The on-axis intensity is shown by the solid lines. The 86% encircled power radius is shown by the dashed lines.

Optical Rectification in a Waveguide

Since optical rectification is a second order nonlinear optical process, it is expected that further THz power scaling can be achieved by increasing the crystal length. However, previous studies have shown that the optimal optical spot size should be roughly equal to the peak THz wavelength inside the crystal [70]. In this regime, the THz only remains collimated for a few wavelengths within the bulk crystal. As shown in Figure 2.4 any THz generated near the entrance face of the crystal quickly diffracts which reduces spatial overlap with subsequent generation and frustrates coherent buildup. Furthermore, diffraction not only reduces the power scaling benefits of using a longer crystal by preventing the coherent buildup of THz radiation, it also degrades the quality of the THz beam at the exit face of the crystal by spatially chirping it. One solution for mitigating the detrimental effects of diffraction is to reduce the crystal cross-section and thus confine the radiated THz in a waveguide. It is important to note that only the THz radiation is confined by the waveguide, and not the optical pump. The concept of using a narrow waveguide to confine the THz during generation was first explored in narrowband

generation via difference frequency generation [71]. Here, researchers showed that transitioning to waveguide geometry improved efficiencies nearly an order of magnitude.

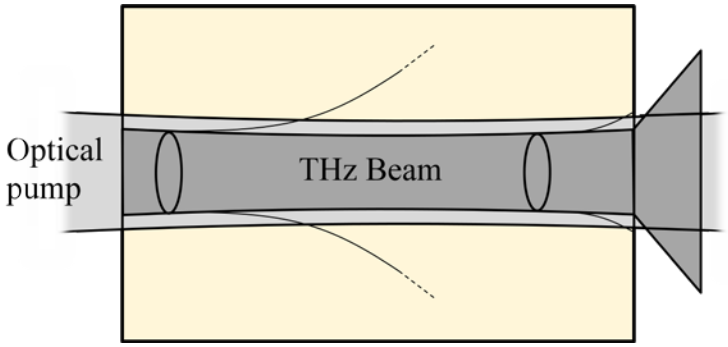

Figure 2.4 Diagram of the terahertz generation inside a thick, bulk crystal. Generation near the entrance face (first ellipse) quickly diffracts and is a negligible contribution to the final emitted beam.

As shown in the previous section, efficient THz generation via optical rectification requires the group velocity of the optical pulse to match the phase velocity of the THz pulse. To quantify this velocity matching, a coherent length is introduced as

$$L_c = \frac{\lambda_{THz}}{2\left|n_{THz} - n_g\right|} \tag{2.11}$$

where λ_{THz}, n_{THz}, and n_g denote the free space THz wavelength, the refractive index for the THz wave, and the group index for the optical pump pulse, respectively. Phenomenologically, the coherence length is the crystal length at which point the instantaneous THz generation is out of phase with the previous generation and the total field begins to decrease. The requirement of velocity matching can be satisfied for specific combinations of nonlinear crystals and laser systems. For example, ZnTe has become the most popular optical rectification crystal for Ti:Sapphire lasers due to a much longer coherent length at 0.8 μm as compared to other crystals with similar nonlinearity. For THz systems based on 1.0 μm lasers, GaP becomes the optimal crystal for broadband optical rectification. Figure 2.2b shows the frequency dependent refractive index of bulk GaP and ZnTe with the Sellmeier coefficients taken from Palik 1991 [69]. For reference, the optical group index for GaP at 1.064 μm and ZnTe at 0.8 μm is shown by the dashed lines. Owing to the higher optical phonon resonance (11 THz for GaP versus 5.3 THz for ZnTe [72]), GaP has a much flatter index curve, which indicates a broad velocity-

matching bandwidth with less dispersion. The broader velocity-matching bandwidth allows efficient generation of broadband THz pulses; meanwhile, the smaller dispersion allows those pulses to propagate through a longer GaP crystal with less distortion. It is these two distinct properties that make it possible to implement broadband THz emitters using GaP waveguides.

One approach to modeling the dielectric waveguide is based on a finite difference frequency domain (FDFD) method [73]. This method solves a discrete form of Maxwell's equations using an eigenvalue approach, and allows one to calculate the propagating modes and their dispersion in a waveguide with a given cross-section. Figure 2.5 shows the results from the FDFD calculation for a square $1\,mm^2$ GaP waveguide. As expected the waveguide modifies the effective refractive index curve by introducing several new sources of dispersion. For example, within a single mode the index curve shows signs of waveguide dispersion. At high frequencies, the large permittivity difference between the GaP rod and the surrounding air effective confines the THz entirely with the GaP waveguide and the effective refractive index closely tracks the bulk index (Figure 2.5a). However, as we shift to lower frequencies, the THz field begins to penetrate into the surrounding air and the effective refractive index drops in comparison to the bulk refractive index (solid black line), eventually crossing the optical group index at 1.064 μm (dashed horizontal black line). The waveguide dispersion reduces the phase mismatch near and above the crossing point and should manifest as a slight increase in the THz generation in that range. This gain, however, is offset by the steepness of the dispersion curve below the crossing point, which leads to strong oscillations in the THz spectrum at low frequencies.

In addition to the waveguide dispersion, THz propagation in the GaP rod will also suffer modal- and polarization-dispersion. As will be discussed later, the waveguides are fabricated by dicing thin slabs of single crystal GaP, into long rectangular waveguides. This method of fabrication tends to produce highly multimode waveguides as shown in Figure 2.5b. Depending on the pumping conditions, the modal dispersion can be exploited to produce high power spatially chirped beams, or lower power near-ideal Gaussian THz beams. As the optical pump pulse propagates down the waveguide, the

non-linear polarization source will couple to the different modes. Since each mode has a different dispersion curve, each mode will generate a unique THz pulse with different temporal and spatial distributions. The total THz field at the exit face of the waveguide is the coherent sum from each mode,

$$E_{total}\,(x, y, z = L, t) = \sum_{i=0}^{N} C_i\, A_i(x, y)\, E_T\big(z = L, t, n = n_{i,eff}\big) \tag{2.12}$$

Here, C_i is the coupling coefficient to the normalized modal distribution, $A_i(x, y)$. Up to this point the vector nature of the electric field has been ignored. However when summing the orthogonal modes, it important to maintain the vector nature of the electric field. $\boldsymbol{E}_{total}$ is the vector sum of the polarized mode, $\boldsymbol{E}_T$. Since the waveguide modes are orthogonal, the THz generation in each mode can be calculated by using equation 2.8 with the waveguide dispersion replacing the bulk material dispersion. The frequency dependent coupling coefficient to each mode can be estimated by integrating the overlap between the source and mode distributions. Assuming the optical pump has a Gaussian profile with a waist w_0, the coupling coefficient at 1.0 THz is shown in Figure 2.5c. By properly choosing the pump diameter, it is possible to generate nearly single mode operation. For waveguides larger than 200 μm, the target pump waist is 49% of the waveguide width. Under such conditions, over 95% THz power falls into the fundamental mode. While equation 2.12 will predict the spatially dependent THz field, it is often more helpful to calculate the average power contained within the THz pulse. If $E_{tot\,al}$ describes a single THz pulse, then the average power in the THz pulse train is given by,

$$P_{avg} \;=\; r_{laser} \iiint \frac{|E_{total}\,(x, y, t)|^2}{2 * \eta}\, \mathit{d}x\, \mathit{d}y\, \mathit{d}t \tag{2.13}$$

Where r_{laser} is the repetition rate of the laser and η is the impedance of free space. If the coupling coefficients in equation 2.12 are computed between normalized distributions, $\iint A(x, y)^2\, \mathit{d}A = 1$, one can use the orthogonality of the waveguide modes to simplify the above equation. Assuming a normalized pump with a Gaussian cross section, $I(x, y)$,

and a coupling coefficient, $C_i = \iint I(x,y) \cdot A(x,y)\, dA$, the average power is the incoherent sum of the power in each mode,

$$P_{avg} = 2\pi \left(\frac{w_0}{\sqrt{2}}\right)^2 r_{laser} \sum_{i=0}^{N} C_i \int \frac{|E_{i,THz}|^2}{2\eta} dt \tag{2.14}$$

For some applications such as spectroscopy and sensing, a significant increase in the total THz bandwidth and power is preferable to spatially pure beam. In these instances, it is possible to exploit the multimode capabilities of the waveguide to generate more power than the single fundamental mode can provide. As one reduces the optical beam diameter below the single mode radius, the coupling to higher order modes increases dramatically, as show in Figure 2.6. Starting with equation 2.12, the spatially dependent THz field was calculated at the exit face of a 6 mm long GaP crystal with a 1x1 mm cross section. The THz was then Fourier transformed and the magnitude was plotted in the upper panels of Figure 2.6. The optical beam polarization and crystal orientation were chosen to generate a horizontally polarized non-linear source. Although the waveguide is square, the $\vec{E}_{x,THz}$ modes are not symmetric due to the high contrast boundary conditions at the GaP / air interface. The optical beam cross section was assumed to propagate unmodified through the crystal despite clipping in the larger beams. Beginning with the 800 μm beam, the generated THz is near single mode at low frequencies. Higher frequencies on the other hand will preferentially generate in the higher order modes due to the smaller phase mismatch.

As we reduce the pump cross section, the coupling into higher order modes is enhanced and we see multimode behavior even at low frequencies despite a very strong phase mismatch. Theoretically the coupling to higher order modes in a large waveguide will allow near 100% source-to-mode efficiency for even very small pump cross sections. Assuming the total optical power is held constant, the increase in intensity leads to a $1/w_0^2$ THz power dependence as shown in the bottom left panel in Figure 2.6. This scaling continues until the optical spot shrinks below $\lambda_{peak}/2n$, which is the smallest feature a given mode may have. As an additional benefit, the higher order modes generate higher frequencies leading to a broadening of the overall THz bandwidth as shown in the bottom right panel.

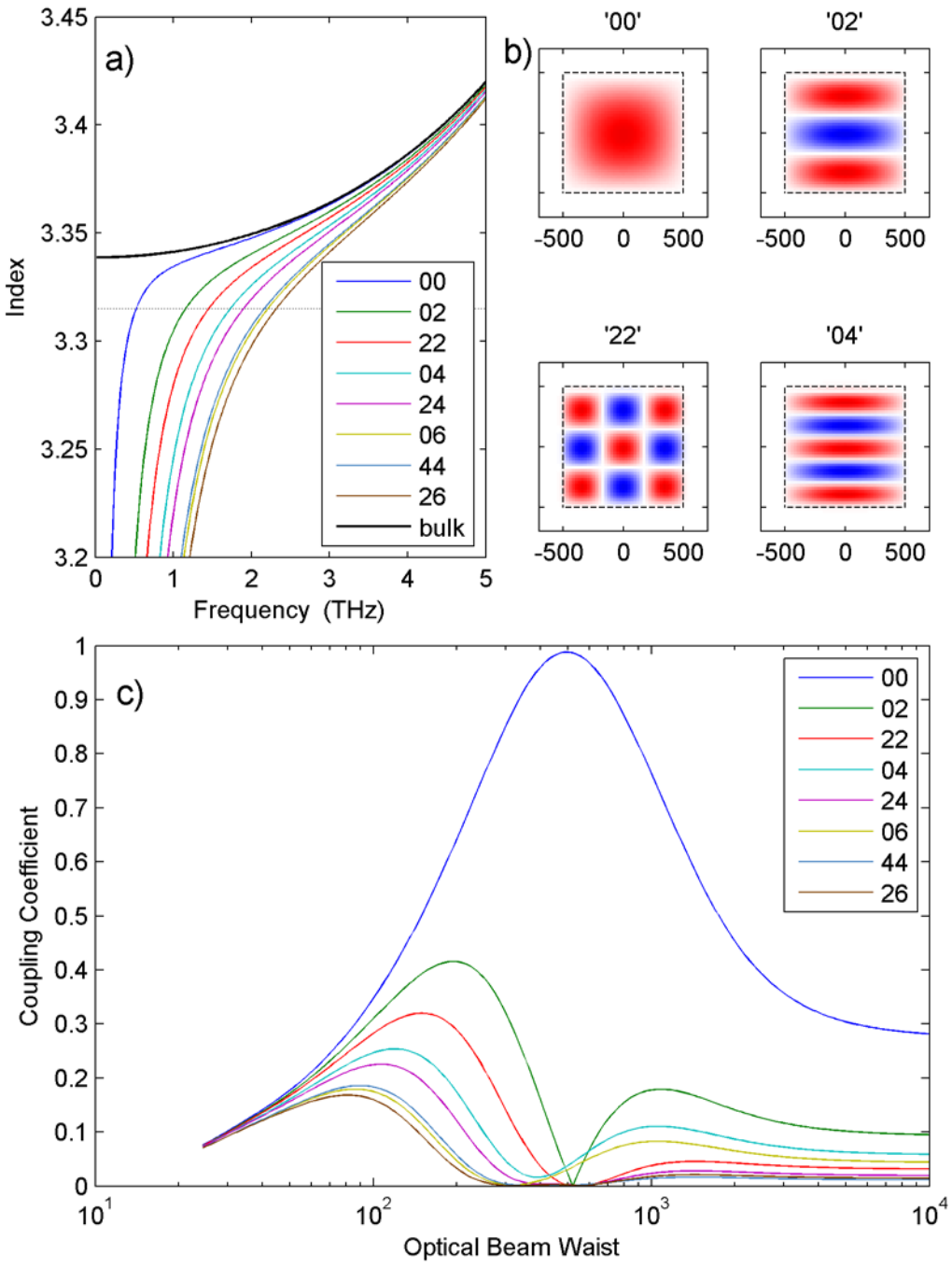

Figure 2.5 shows a sample of the calculated modes for a 1000 µm × 1000 µm GaP waveguide in air. The FDFD calculation yields the effective refractive indices (a) and field cross-sections (b) for the fundamental and higher order modes. A few example cross sections show the THz field distribution at 1.0 THz, relative to the GaP crystal (dashed lines). As pump pulse propagates down the waveguide, the source will couple to the different modes with an efficiency shown in part (c).

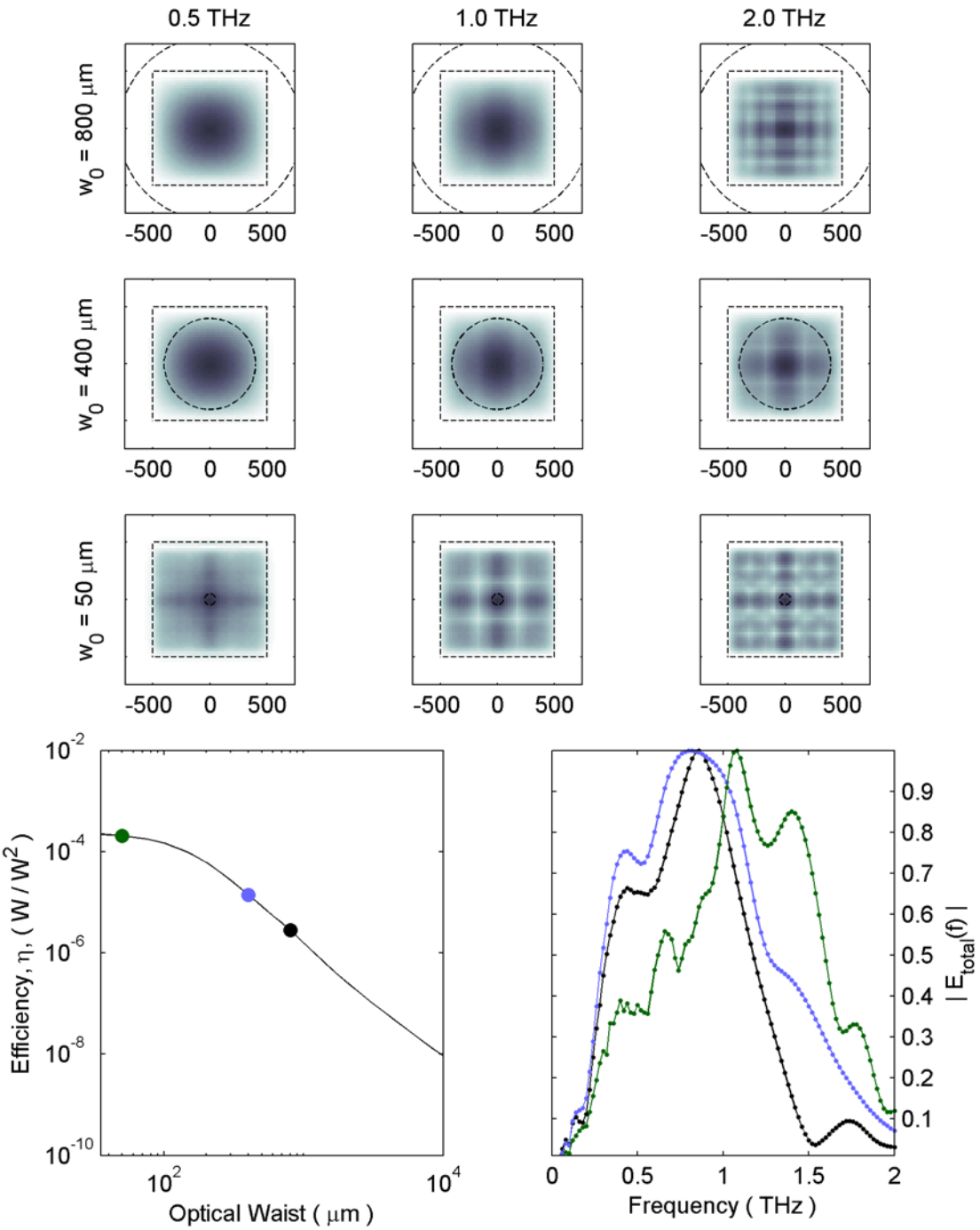

Figure 2.6 shows the magnitude of the generated spectrum across a 1×1×6 mm GaP cross section (dashed square). As the pump waist (dashed circle) shrinks, higher order modes are excited which coherently interfere at the exit of the crystal. The simulation assumed a 230fs Gaussian pulse centered at 1.03 μm, with the crystal oriented to generate a horizontal nonlinear polarization. The bottom left panel shows the conversion efficiency, P_{THz}/P_{opt}^2 and the right panel shows the normalized spectrum at the three pump conditions shown.

In addition to selective pumping, the generated THz spectrum can be tailored by controlling the waveguide cross section. Figure 2.7 illustrates the effective index of the fundamental modes versus THz frequency for square GaP waveguides with different cross-sections. For comparison, the optical group index at 1.035 μm is also shown in the same figure. As we shrink the waveguide cross-section, the effective index curve tends to bend and intersect with the optical group index curve at a higher THz frequency. For example, the intersection frequency shifts from 0.25 THz to 1.5 THz as the waveguide width changes from 2000 μm down to 250 μm. Since perfect velocity matching is achieved at the intersection point, the generated THz spectrum will be peaked around this point, as suggested by equation 2.8.

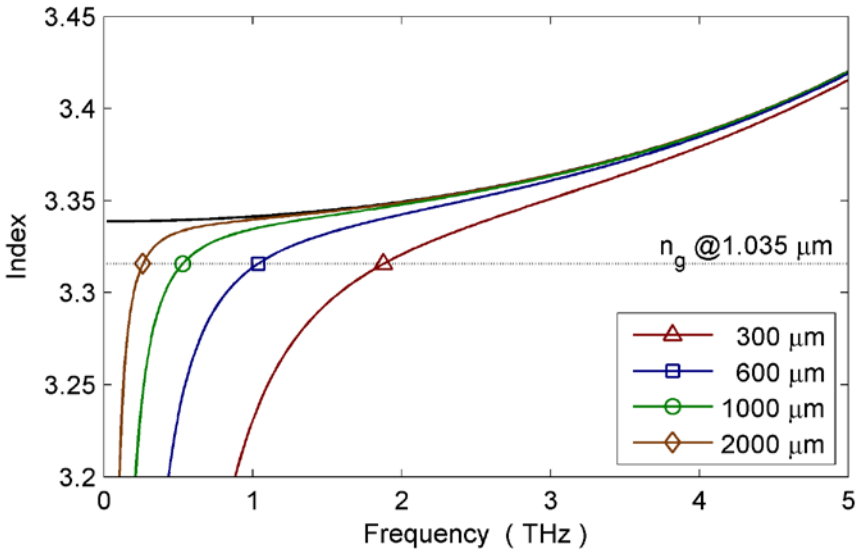

Figure 2.7 The dependence of THz indices on frequency. The solid black curve denotes the refractive index of bulk GaP. Four curves represent the calculated effective indices of the fundamental mode for GaP waveguides with different cross-sections. The dashed curve represents the group index of GaP at 1.035 μm.

One might speculate that the THz power would continue to scale with the waveguide length. Unfortunately as the GaP reaches a certain length, the material loss approaches the rate of generation, and the power scaling plateaus. Another drawback of using long waveguides is that dispersion narrows the generated THz spectrum and thus stretches the TD-THz pulse. An optimal length for a waveguide emitter should be chosen in order to achieve the best overall performance in terms of power scaling, THz pulse time duration, and THz spectrum width. With regards to a GaP waveguide, it can be shown that this optimal length falls between 5 mm to 1 cm depending on its cross-section.

Setup and Experimental Results

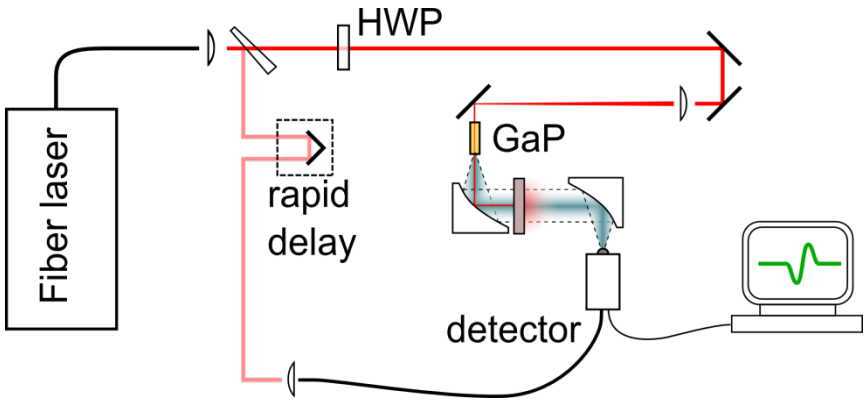

Figure 2.8 shows the experimental setup for THz wave generation and detection. The fiber laser is either the homebuilt parabolic pulse system or a commercial Clark MXR Impulse

Initial measurements of the GaP waveguide concept were performed on a homebuilt fiber laser system based on parabolic pulse amplification [74]. In this configuration, the pulse train from a fs-oscillator is non-linearly amplified by a Yb-doped fiber amplifier and then the linear chirp developed during amplification is removed by a compressor. In our setup, the seed to the fiber amplifier is a passively mode-locked Nd:glass oscillator (High-Q UC-100fs) with an average power of 120 mW and a repetition rate of 72 MHz. The optical pulse has duration 110 fs and its spectrum is centered at 1.064 μm. The fiber amplifier consists of a 6.5 m polarization maintaining fiber with a 30 μm Yb-doped core and a 400 μm hexagonal-shaped inner cladding. A 1.2-meter photonic bandgap fiber (PBGF) is employed to recompress the stretched, amplified pulse. The details for a similar parabolic fiber amplifier are described by Chang et al [25]. The entire fiber laser system is labeled “Fiber Laser” in the setup shown in Figure 2.8

During the parabolic pulse amplification, the pulse spectrum broadens and the amplified pulse may be compressed even shorter than the initial duration given a complete compensation of the pulse chirp. However due to the dispersion mismatch between the fiber amplifier and the PBGF compressor, the pulses in our current setup are only compressed to ~200 fs with an average power of 6 W. We prepared two 6-mm-long (110) oriented GaP rectangular waveguides with cross-sections of 1000 μm × 700 μm

and 600 μm × 400 μm. The waveguide emitters were mounted onto a gold mirror with their shorter edges touching the gold surface. In the experiments, the 6 W, ~200 fs compressed pulses were focused into the waveguide with ~200 μm beam diameter. At the exit face of the crystal, the diffracting THz and collimated optical beam were collected by a 3" paraboloid, and a high density polyethylene slab was used to separate the collinear beams. Coherent detection of the THz pulses was achieved using a photoconductive based receiver fabricated by Picometrix, which is optically gated with a few mW picked off early on.

Figure 2.9 shows the measured THz waveforms from the GaP waveguide emitters, normalized to the peak field of the larger waveguide. The Fourier transformed spectra of the two traces are shown in the lower plot, again normalized to the peak spectral intensity of the larger waveguide. As a reference, the calculated dispersion for the fundamental mode for each waveguide is shown in the inset. In the time domain, both waveforms exhibit multi-cycle oscillations with the larger waveguide clearly showing dispersion induced broadening. While the THz pulse from the smaller waveguide also experiences dispersion, its oscillations are primarily due to a reduction in the low frequency content. As can be seen from the inset, the narrow waveguide's steep dispersion at low frequencies will lead to rapid oscillations in the phase matching function and poor generation efficiency. Fortunately, the loss in low frequency is compensated by a significant increase at higher frequencies. Clearly the peaks of the two spectra coincide with the perfect velocity-matching frequencies where the corresponding phase matching functions are maximized, respectively. It is worth noting that the coherent length of a bulk GaP is enhanced as the pump wavelength shifts towards 1.000 μm [69]. Thus it is more convincing to compare the power scaling potential of a GaP waveguide emitter and its bulk counterpart at pump wavelength less than 1.064 μm, the operating wavelength of current parabolic fiber amplifier.

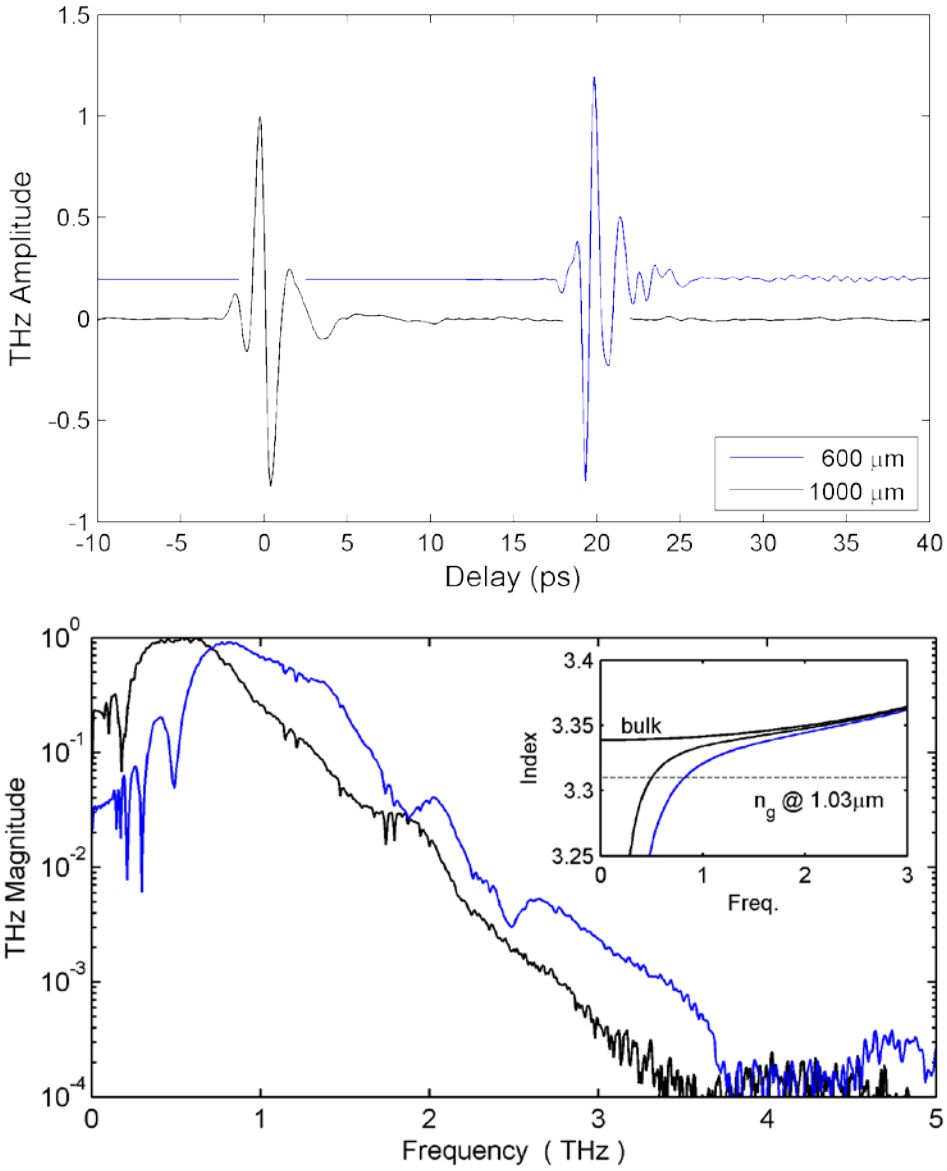

Figure 2.9. Measured THz temporal waveforms from two GaP waveguide emitters, under identical pumping. The Fourier transform calculated spectra are normalized to maximum spectral intensity (1000 μm @0.6 THz). The waveguide crosssections are 1000 × 700 μm and 600 × 400 μm.

For this purpose, we employed a commercially available Yb-doped fiber amplifier system (Clark-MXR Impulse) to pump the 1000 μm × 700 μm waveguide. This laser system was able to deliver up to 10 W, ~230 fs pulses centered at 1.035 μm with a repetition rate of 25 MHz. Two changes were made to the setup shown in Figure 2.8. First, the higher power optical beam began to melt the HDPE filter, so an alumina hyperhemisphere was placed at the exit face of the waveguide to help scatter the optical beam over a larger angle. With the hyperhemisphere, the optical beam fills the

paraboloid and the on-axis intensity is several orders of magnitude lower at the HDPE filter. Second, a liquid-helium-cooled silicon bolometer from IRLabs replaced the photoconductive receiver. Bolometers are typically used to measure long wavelength average power in the pW to μW range. Nonlinearity in the bolometer's response was avoided by placing metalized pellicle filters in the collimated beam between the paraboloids to keep the incident average power below 1μW. The pellicle transmission was calibrated over the expected frequency range using a separate TD-THz system, and normalized out in subsequent measurements. The waveguide power measurements are presented in Figure 2.10. For comparison, the power measurements from a 1 mm bulk GaP crystal are also shown. At an optical power of 10 W, we were able to generate broadband THz pulses with an average power of 150 μW from the larger waveguide and 120 μW from the narrower waveguide. This represents a 12-15x improvement over the thinner 1mm crystal.

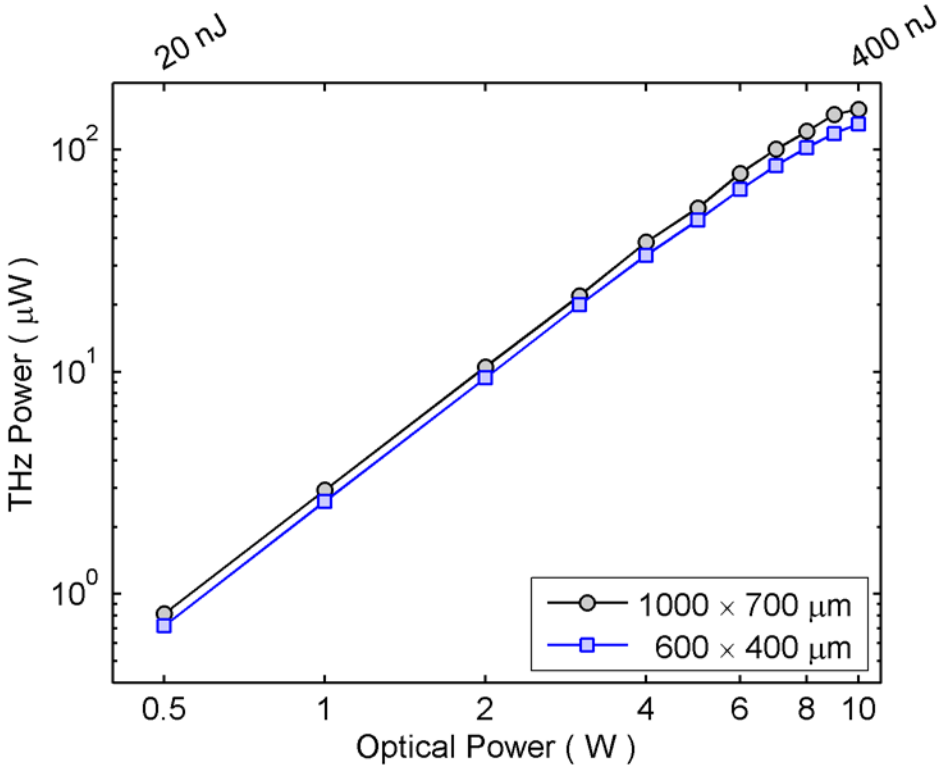

Figure 2.10 shows the THz power dependence on pump pulse energy. The two waveguides exhibit quadratic power scaling for pulse energies below ½ μJ.

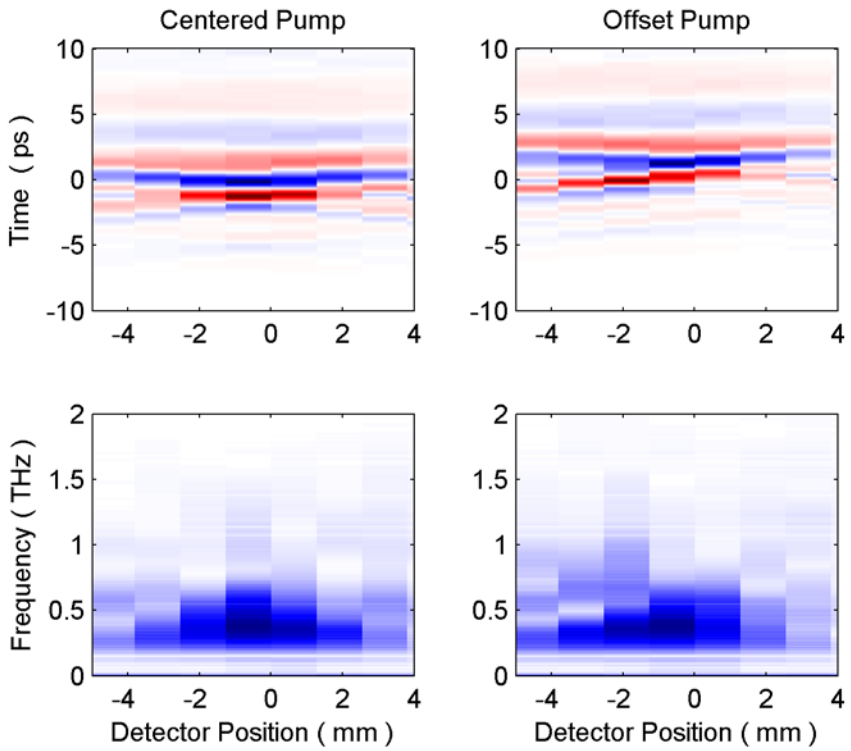

Figure 2.11shows the spatial chirp induced by an offset pump beam.

Previous simulations assumed multimode behavior, however experimentally verifying this can be challenging. In the previous measurements, special care was taken to ensure the optical beam was collinear and centered on the GaP waveguide. However, by offsetting a large diameter beam, one would expect to excite a superposition of the '00' and '10' modes. Figure 2.11 show the spatial chirp induced by an offset pump beam. A large 300 µm waist pump beam was offset by 150 µm in the larger 1000 µm × 700 µm waveguide. The detector was then horizontally scanned across the reimaged THz beam. Although the paraboloids should create a 1:1 imaging system, the THz extends well beyond the waveguide width in the image plane. This is due the limited numerical aperture of the imaging system as well as aberrations induced by the alumina hyperhemisphere [75] and the parabolic mirrors [76].

From simulations, the fundamental mode and the 10 mode generate similar spectra with the fundamental mode preferring lower frequencies. From the experimental conditions, the coupling and phase-matching should balance around 0.5 THz. Spatially the fundamental mode is horizontally and vertically symmetric, while the 10 mode has a sign about the vertical axis. Comparing the centered pump to the offset pump in Figure

2.11, we can see that the offset pump generates a spatially chirped beam, with the left side generating significantly less signal at 0.5THz.

Conclusion

In principle, the strong index contrast between the crystal and surrounding air combined with the relatively wide core creates a highly multimode waveguide. Fortunately by manipulating the spot size of the optical beam in the waveguide, one can optimize the THz excitation cross section to match the fundamental mode profile, and at optimal excitation the fundamental mode can carry more than 95% of total emitted THz power. Unfortunately, single mode excitation is unadvisable for waveguides wider than 600 μm, since the optical beam diameter must scale with the increasing waveguide width. Unless the pulse energy can be increased to maintain peak intensity, the THz conversion efficiency and power will drop with larger waveguides.

For a rectangular waveguide, the fundamental mode has two different spatial profiles corresponding to horizontal and vertical polarizations respectively. These two orthogonal modes propagate at slightly different speeds leading to modal dispersion. Although this detrimental effect is minimal for 6 mm long waveguides, a GaP emitter with square or circular cross-section is preferred in order to achieve a degeneracy of these two orthogonal modes.

In conclusion, we have demonstrated that GaP waveguides are capable of emitting broadband THz pulses, and we have investigated their power scalability. With a 6 mm emitter, a record average power of 150 μW is obtained by pumping it with a high power Yb-doped fiber laser system. We also demonstrated that the dispersion can be tailored by changing the waveguide cross-section, which opens the possibility of building compact broadband THz sources centered at a select frequency by engineering the dispersion of waveguide emitters. In fact, additional design flexibility can be achieved by encapsulating a GaP waveguide with other materials (dielectric or metal).

Chapter 3
THz Dynamics in Epitaxial Graphene

Numerous studies have probed bulk graphite's behavior in the THz region, from recent work such as the demonstration of ultrafast coherent photocurrents [77], to early spectroscopic measurements [78], and even to the study of centuries old paintings and murals [79]. However the recent isolation of single atomic layers of graphite should provide new opportunities for interesting physics. Of the several common graphene fabrication or isolation methods outlined in Chapter 1, only epitaxial growth is a controlled process that can produce large samples with excellent electronic properties and compatibility with standard lithography techniques. In particular, the high carrier mobility, excellent thermal conductivity [8], and long ballistic lifetime [9] in epitaxial graphene offer interesting new opportunities for ballistic THz resonators, field effect transistors, *pn*-junction diodes, and other high speed electronics [10, 11]. The performance of many of these devices depends heavily on the behavior of hot carriers and the subsequent cooling and recombination dynamics. Further development will require a significant understanding of the mechanisms responsible for the carrier recovery. THz differential spectroscopy, which is well suited to measure ultrafast thin film conductivity changes, is an ideal tool for measuring the recovery dynamics of hot photoexcited carriers in epitaxial graphene.

Theory of Hot Photoexcited Carrier in Graphene

The theory of graphene conduction at THz frequencies has been theoretically studied in a few limiting cases but not under the full experimental conditions. Several papers have been published with different models for graphene's conductivity at DC [29, 30] and at optical frequencies [80]. Further work has extended the range of these models by adapting the DC models to microwave frequencies [34] and the optical formulas to infrared frequencies [81]. A large number of competing theories claim to accurately model our experimental conditions, however many diverge at low frequency or high

temperature. In this section I will present a subset of the published models for the thermoconductivity and carrier cooling dynamics in graphene.

Thermoconductivity of a Single Graphene Layer

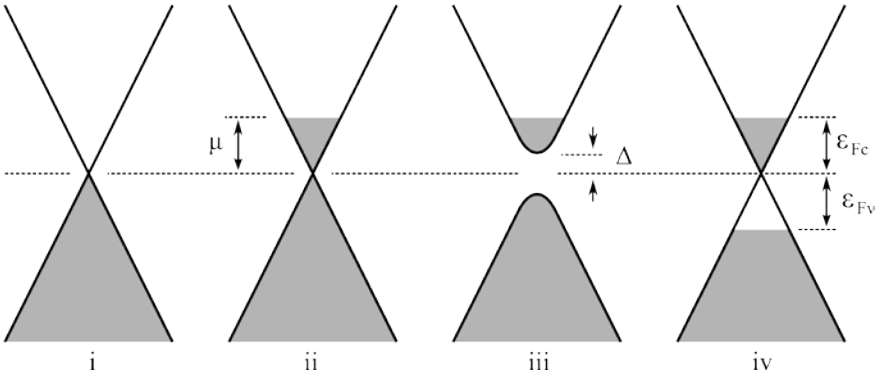

Figure 3.1 shows different models for the band structure of 'undoped' graphene near the Dirac point. The first model (i) assumes intrinsically doped graphene with equivalent electron and hole densities. The second model (ii) allows for extrinsic doping up to a Fermi level, μ. Substrate or multi-layer interactions can potentially open a bandgap at small energies (iii). While photoexcitation can lead to non-equilibrium populations in the valence and conduction bands with quasi Fermi levels, ε_{Fv} and ε_{Fc}.

Theoretical models for the conductivity show a dependence on both interband and intraband transitions. However in the THz range, the response is expected to depend primarily on the intraband conductivity in the large number of undoped layers [34, 81]. An early model for the thermoconductivity of graphene was presented by Gusynin et al. [34, 82-85]. Assuming a frequency dependent scatting rate, *Γ(ω)*, the thermoconductivity for a graphene monolayer is

$$\begin{aligned}\sigma(\Omega,T) = \frac{e^2}{2\pi\hbar}\int_{-\infty}^{\infty} d\omega \frac{f(\omega)-f(\omega')}{\Omega} \\ \times\left[\frac{2\Gamma}{\Omega^2+4\Gamma^2(\omega)} - \frac{2\Gamma}{(\omega+\omega')^2+4\Gamma^2(\omega)}\right] \\ \times(|\omega|+|\omega'|)(\omega^2+\omega'^2), \qquad \omega' = \omega+\Omega\end{aligned} \tag{3.1}$$

where the Fermi function is defined as, $f(\omega) = 1/(1+\exp((\hbar\omega-\mu)/k_bT))$ with a Fermi level, μ. Additionally, Gusynin also proposed a model for a finite bandgap where the quasiparticle energy spectrum is given by, $E(k) = \sqrt{\hbar^2 v_F^2 k^2 + \Delta^2}$, where Δ is the half-gap opening in the graphene bandstructure. In this instance, the thermo-conductivity due to ***massive*** Dirac quasiparticles acquires the form:

$$\sigma(\Omega) = \frac{2\pi e^2}{h} \cdot \frac{(\mu^2 - \Delta^2)\ \Theta(\mu^2 - \Delta^2)}{|\mu|} + \frac{\pi e^2}{2h} \frac{(\Omega^2 + 4\Delta^2)}{\Omega^2}\ \Theta\left(\frac{|\Omega|}{2} - \max(|\mu|, \Delta)\right) \tag{3.2}$$

where Θ, is the unit step function and cuts off the interband contribution below 2μ or 2Δ. The above function only applies for temperatures well below the gap or Fermi energy. In a later work, the full temperature dependence is derived [85].

A second model for the thermoconductivity of graphene was proposed by Falkovsky et. al. [81]. In this work, the graphene reflectivity is calculated as a function of frequency, temperature, and carrier density, while accounting for both interband and intraband transitions. Following the notation of Falkovsky, the interband and intraband contributions to the conductivity can be expressed as:

$$\begin{aligned} \sigma_{\text{inter}} &= \frac{e^2}{4\hbar}\left[G(\omega/2) - \frac{4\omega}{i\pi}\int_0^\infty G(\epsilon) - \frac{G(\omega/2)}{\omega^2 - 4\epsilon}\,d\epsilon\right] \\ \sigma_{\text{intra}} &= i\frac{2e^2T}{\pi\hbar\omega}\ln\left[2\cosh\left(\frac{\mu}{2T}\right)\right] \end{aligned} \tag{3.3}$$

where the function $G(\omega)$ is the integral of the difference of two Fermi-Dirac Distributions, $\int_0^\infty f_0(-\epsilon) - f_0(\epsilon)$. In the limiting cases of high or low temperature the difference asymptotically approaches a hyperbolic tangent and unit step function, respectively. A more numerically stable form of the difference is expressed as,

$$G(\epsilon) = \begin{cases} \tanh(\epsilon/2T) & \mu \ll T \\ \dfrac{\sinh(\epsilon/T)}{\cosh(\mu/T) + \cosh(\epsilon/T)} & otherwise \\ Heaviside(\epsilon - \mu) & \mu \gg T \end{cases} \tag{3.4}$$

A third model has been used to describe the measured transmission from visible to THz. Choi [86] derived a simplified expression for the optical conductivity based on the model by Stauber [87]. In the earlier work, Stauber computed the optical conductivity of

graphene beyond the usual Dirac-cone approximation to include the effect of next-nearest-neighbor hopping and nonlinearities in the bandstructure. Following the notation of Choi, the real part of the conductivity can be expressed as:

$$\Re(\sigma) = \sigma_0 \frac{8k_b T}{\pi\hbar} \ln\left(e^{-\frac{E_F}{2k_b T}} + e^{+\frac{E_F}{2k_b T}}\right) \frac{1}{\omega^2\tau + \frac{1}{\tau}} + \frac{1}{2}\left[\tanh\left(\frac{\hbar\omega + 2E_F}{4k_b T}\right) + \tanh\left(\frac{\hbar\omega + 2E_F}{4k_b T}\right)\right] \tag{3.5}$$

Recovery of Hot Photoexcited Carriers

Recently, the behavior of hot carriers and the identification of the dominant cooling mechanism in epitaxial graphene has received considerable attention. Both degenerate pump/probe at 800 nm [88] and nondegenerate experiments at mid-IR wavelengths [89] have attempted to illuminate the dominant mechanisms and rates associated with carrier recombination and cooling. From a theoretical standpoint, the proposed models fall into two groups.

The first group of models approaches graphene from the view of a semimetal, by describing the hot carrier population in terms of a single hot thermal distribution [89]. An initial ultrafast optical pulse excites carriers high above the Dirac point leading to a non-thermal distribution as shown in Figure 3.2 (i). Within a few picoseconds, carrier-carrier scattering rapidly thermalizes both electrons and holes into a single hot distribution with identical Fermi energies and temperatures (ii). The distribution cooling is then dominated by optical phonon emission at high temperatures ($T_{carrier}$ > 180 K) and acoustic phonon emission at low temperatures [90], eventually recovering the initial pre-excitation distribution (iii). In the few highly doped layers at the bottom of the stack, the carrier cooling is described by a simple exponential recovery; however in lightly doped top layers, the recovery is described by a pair of coupled rate equations. Following the notation of Bistritzer,

$$I_n^{(\pm)} \equiv \int \frac{k^n \, dk}{2\pi} [f_k^c \mp (1 - f_k^v)] \tag{3.6}$$

$$-3v_g T_e \partial_t \left(\frac{1}{T_e}\right) I_2^{(-)} + 2T_e \partial_t \left(\frac{\mu}{T_e}\right) I_1^{(+)} = \frac{D^2}{(\rho v_g^2)} (T_e - T_L) I_3^{(-)} \quad (3.7)$$

The first equation described conservation of charge, i.e. $\partial_t n = 0$, while the second describes the rate of energy transfer between the carrier distribution and the acoustic phonon bath. By limiting the heat transfer to acoustic phonons only, the second equation is only valid for carrier temperatures, T_e, and lattice temperatures, T_L, below 180K. The screen deformation potential, D, is typical between 10 eV and 50 eV.

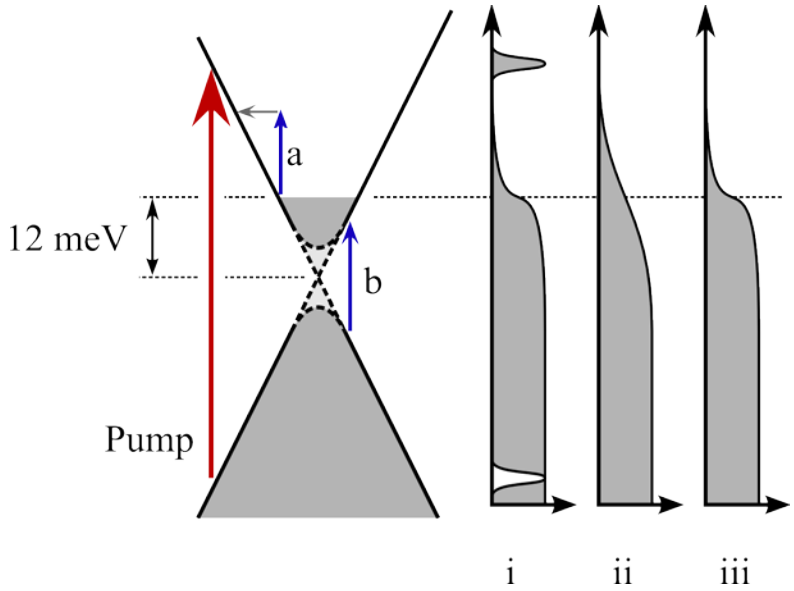

Figure 3.2 shows the band structure and carrier distribution after optical excitation. The pump photon (red, greatly reduced) excites carriers (i) which rapidly thermalize establishing a new hot thermal distribution (ii). The hot distribution slowly cools (iii) until the original distribution is recovered. During the distribution's evolution, probe photons can interact through interband transition (b) or through intraband transitions (a) via a scattering event.

The second group of models approaches graphene from the view of a semiconductor, by describing the distribution of electrons and holes separately. Following the same excitation, electrons and holes separately thermalize within the conduction and valence bands leading to quasi-Fermi levels. These two populations can then recombine via Auger processes [91] or phonon scattering [92], quickly recovering the initial pre-excitation distribution. Similar to the first model, the dynamics are described by a series of coupled rate equations.

In addition to the above models which assume thermal distributions, recent work using density matrix theory has modeled the initial non-thermal distribution immediately following excitation [93, 94]. Microscopic calculations indicate that electron-phonon coupling leads to an initially ultrafast energy dissipation and non-thermal carrier and phonon distributions. Within 50 fs, half of the excitation energy is lost to recombination and phonon emission and within 500 fs, 90% of the energy is lost. As the distribution cools, the reduced density of states and partial filling of the phonon modes leads to drastic reduction in the cooling rate with a recovery lifetime greater than one picosecond.

Multilayer Transmission with Transfer Matrices

In order to translate between the thermoconductivity of graphene and the THz transmission measurements, a model for the THz transmission of a thin conducting film is needed. The transfer matrix approach is a simple method for calculating the transmission through a multilayered structure. This approach works well for structures where the incoming and outgoing fields of an optical element can be expressed as a linear combination of the fields on the other side of the element. Mathematically, the fields for a single layer are related through a 2×2 matrix and the total field through the stack is simply the matrix product for each layer. Beginning with a single graphene layer at normal incidence, the boundary conditions for the transverse electric fields is:

$$E_i^+ + E_i^- = E_j^+ + E_j^- \tag{3.8}$$

Where E_i^+ and E_i^- are in incident forward and reflected waves, and E_j^+ and E_j^- are the transmitted and backward propagating waves. Similarly, the continuity equation for the magnetic field gives the following relation,

$$H_i + H_j = \frac{E_i^+ - E_i^-}{\eta_i} + \frac{E_j^+ - E_j^-}{\eta_j} = \sigma(E_i^+ + E_i^-) \tag{3.9}$$

where $\eta_i = \sqrt{\mu_i/\epsilon_i}$ is the impedance and σ is the conductivity. The transfer matrix for a single graphene layer, $\boldsymbol{M}_i$, is then,

$$\begin{bmatrix} E_i^+ \\ E_i^- \end{bmatrix} = \boldsymbol{M}_i \begin{bmatrix} E_j^+ \\ E_j^- \end{bmatrix} = \begin{bmatrix} \left(\frac{1}{2} + \frac{\eta_i}{2\eta_j} + \frac{\eta_i \sigma}{2}\right) & \left(\frac{1}{2} - \frac{\eta_i}{2\eta_j} + \frac{\eta_i \sigma}{2}\right) \\ \left(\frac{1}{2} - \frac{\eta_i}{2\eta_j} - \frac{\eta_i \sigma}{2}\right) & \left(\frac{1}{2} + \frac{\eta_i}{2\eta_j} - \frac{\eta_i \sigma}{2}\right) \end{bmatrix} \begin{bmatrix} E_j^+ \\ E_j^- \end{bmatrix} \tag{3.10}$$

which agrees with the results from the Dyadic Green function method [95]. The total field transmission through the graphene stack can be expressed as the product of the individual matrices, $M_{total} = \prod_{i=1}^{N} M_i$. The amplitude transmission through and reflection from the stack can be expressed as

$$\begin{aligned} M_{total} &= \begin{bmatrix} A & B \\ C & D \end{bmatrix} \\ t &= \frac{E_j^+}{E_i^+} = \frac{1}{A} \\ r &= \frac{E_i^-}{E_i^+} = \frac{C}{A} \end{aligned} \tag{3.11}$$

For THz spectroscopy of thick graphene stacks, the response is dominated by the large number of undoped layers. In the limit of thick stacks, the total conductivity is the sum of the undoped layers [96] and the above equations simplify to:

$$\mathrm{t} = \frac{2}{1 + \mathrm{n_{SiC}} + \mathrm{N}\eta_0\sigma} \tag{3.12}$$

where η_0 is the impedance of free space and σ is the conductivity of a single layer. The transmission of graphene is commonly normalized to the bare substrate transmission [86, 88, 97, 98], which yields:

$$\begin{aligned} \mathrm{t_{graphene}} / \mathrm{t_{SiC}} &= \frac{1 + \mathrm{n_{SiC}}}{1 + \mathrm{n_{SiC}} + \mathrm{N}\eta_0\sigma} \\ &\approx \frac{1}{1 + \mathrm{N}\eta_0\sigma/(1 + \mathrm{n_{SiC}})} \end{aligned} \tag{3.13}$$

where the approximation is valid for few layer samples.

Equation 3.11 can be evaluated for typical values of the graphene conductivity [11, 80, 81, 99]. Figure 3.3 shows amplitude transmission and reflection coefficients for a 63 layer or a 13 layer sample, assuming a uniform purely real or purely imaginary

conductivity. Unlike the dynamic conductivity at optical frequencies, at THz frequencies, the conductivity is expected to be dominated by intraband transitions which contribute a strong imaginary component to the total conductivity. However theoretical models are incomplete at the experimental conditions where the chemical potential, the carrier temperature, and the probe wavelength are all comparable, $\mu \approx \hbar\omega \approx k_B T \approx$ few meV. Numerical evaluation of the conductivity equations in Ref [81], is effectively imaginary although the magnitude diverges at low probe wavelengths and does not replicate the spectral shape observed.

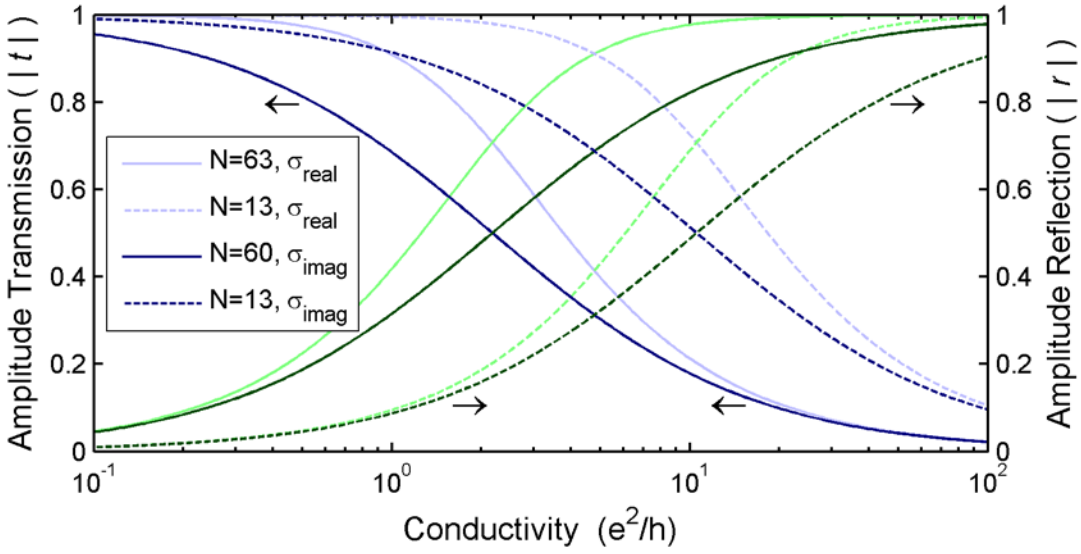

Figure 3.3 shows the amplitude transmission and reflection coefficients for a 63 (solid lines) and 13 (dashed lines) layer graphene stack, assuming either a purely real conductivity (light color) or a purely imaginary conductivity (dark color). The amplitude reflection coefficient is shown in green, and the amplitude transmission coefficient is shown in blue.

Differential THz Transmission Setup

Ideally, the graphene transmission would be measured using the high power system developed in the previous chapter. However it was unavailable at the time of this experiment, so a new setup was built around a Ti:sapphire regen and a photoconductive emitter. The THz transmission is measured using the time domain spectrometry setup shown in Figure 3.4. Ultrafast 60-fs pulses from a Ti:sapphire amplifier (RegA) centered at 800 nm are used to trigger a large area photoconductive emitter. The generated THz is collected with a 6” 90° gold paraboloid that was chosen to match the divergence angle of

the emitter (see Appendix C). The collimated THz is refocused with a 3" paraboloid concentrating the THz field. As with any broadband beam, the limited numerical aperture of the imaging optics creates a highly frequency-dependent focal spot. For detailed measurements of the probe spot, refer to Appendix B.

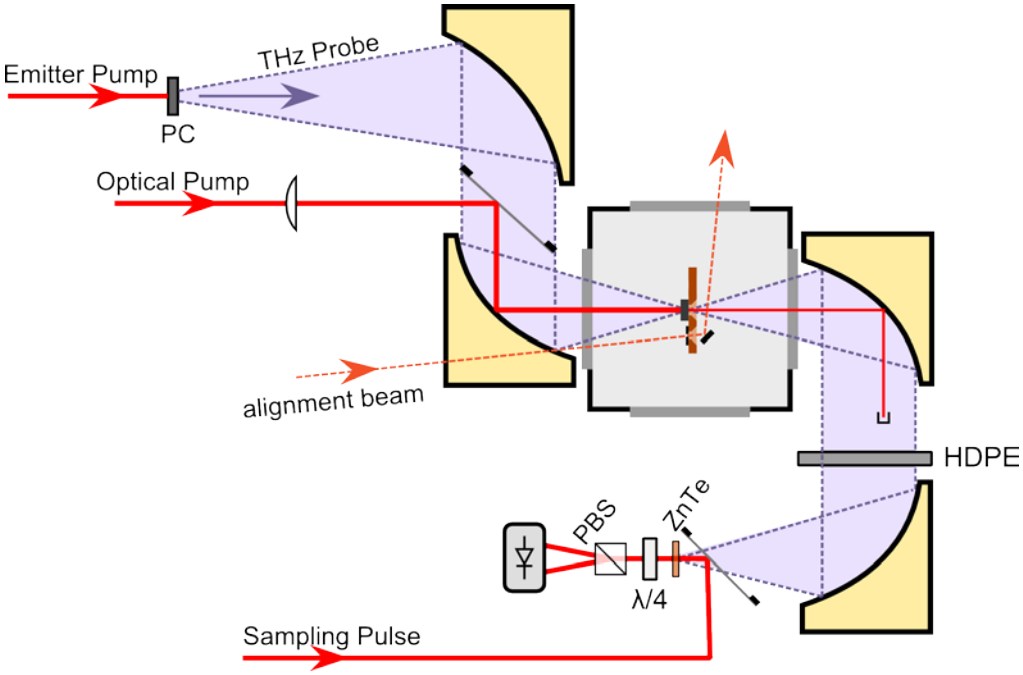

Figure 3.4 shows the THz differential transmission setup.

A high reflectivity pellicle is used to combine the optical and THz beams with a 97% optical power reflectivity and an 85% THz amplitude transmission. The focal spots are overlapped on the sample with a 2.0 mm and 0.8 mm spot size for the optical pump and the RMS THz probe, respectively. The slight angle between the beams is sufficiently small to prevent temporal walkoff across the relatively large probe spot. A 10 cm lens is used to create a pseudo-collimated optical pump after the focusing paraboloid.

The spherical lens / backwards-paraboloidal-mirror telescope introduces significant aberrations on the pump beam, although the short propagation distance and nature of the THz probe mitigate most of these problems. The aberrations manifest as a temporal smearing and non-uniform pumping via wavefront and cross-section distortion, respectively. The wavefront distortion primarily introduces a non-uniform arrival time across the pump beam. Numerical simulations using Zemax suggest the wavefront error is on the order of 3-4 λ at 800 nm or 10 fs, which is much smaller than the temporal

resolution of the THz probe system. On the other hand the coma shifts the Gaussian cross-section into a teardrop shape. Fortunately the THz probe spot fits well within the central lobe of the optical pump, minimizing the effect. One final difficulty arises from the surface quality of the paraboloid. Residual machining groves cause a high spatial frequency modulation across the spot as seen in upper left panel of Figure B.1 and Figure B.2.

The sample is mounted inside a liquid helium cryostat positioned at the THz beam waist. A high density polyethylene filter and beam block are used to separate the transmitted THz and residual pump light. The transmitted THz pulse is detected using electrooptic sampling in a 1.0 mm ZnTe crystal. The effective bandwidth of the sampling system is limited to 2 THz by phasematching in the ZnTe crystal and absorption in the cryostat's fused silica windows. To increase the signal to noise ratio, the TeraSED pump or the optical prepulse beam are mechanically chopped at 1.2 kHz and detected using a lockin amplifier (see Appendix D for the chopping frequency selection). The sample alignment is maintained during temperature adjustments by monitoring the transmission through a 100 μm pinhole mounted to the sample holder.

One of the early difficulties we encountered was sample heating at high average power from the optical pump beam. The beam-splitting and delay optics not shown in Figure 3.2, allowed a limited ability to adjust the relative power of each beam. The ultrahigh repetition rate RegA system generates >4 μJ pulses, from which 1 μJ is used to pump the THz emitter, 40 nJ are used in the ZnTe EO crystal and up to 2.2 μJ are used to pump the sample. When compared to conventional optical pump/probe techniques, the extremely large THz probe diameter requires a similarly large pump diameter, significantly reducing the peak pump fluence to more conventional levels (~10 $\mu J/cm^2$). For room temperature experiments, the regenerative amplifier repetition rate was set to 250 kHz, which allowed a peak transmission SNR in excess of 10^4. At this repetition rate, the heat load in the darkest graphene sample (#7J8) is 200 mW which exceed the cryostat's removal capacity. For cryogenic experiments below 100 K, the system repetition rate was dropped to 50 kHz, which reduced the heat load to manageable levels.

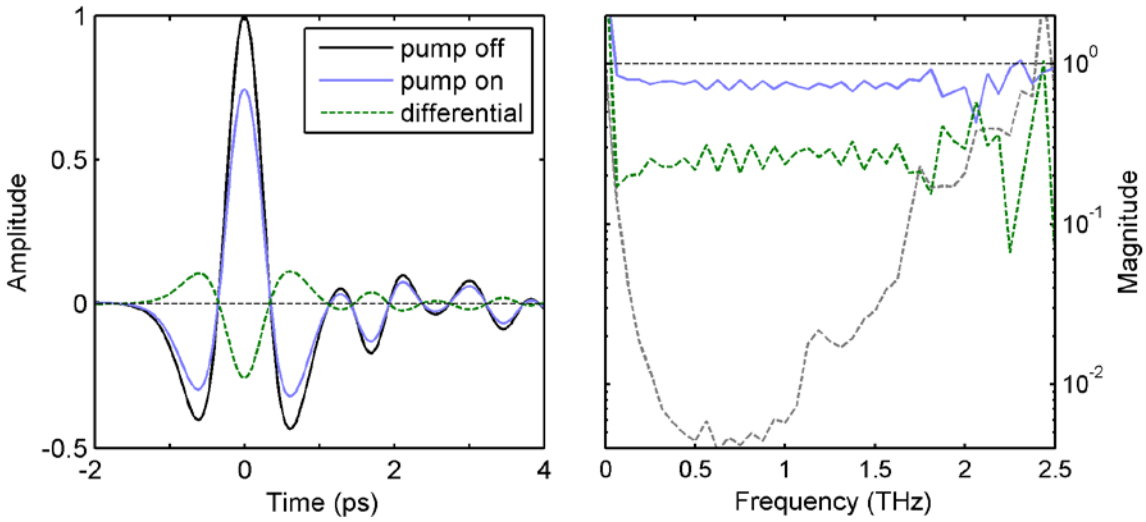

Figure 3.5 shows the induced change in the transmitted THz at maximum modulation (full pump at 4K) in the left panel. The right panel shows the normalized spectrum of the pump-on and the differential signals relative to the pump off spectrum. The noise floor of the system (1/pump-off spectrum) is shown by the gray dashed line.

An example time domain THz trace is shown in the left panel of Figure 3.5. The black curve shows the transmitted waveform through the 63 layer sample (#7J8) at cryogenic temperatures and for a 1 second acquisition with no signal averaging. Using lockin techniques, the attenuated signal can be either measured directly by chopping the emitter or indirectly by chopping the optical pump and measuring the differential signal. While the direct measurement produces a more intuitive result, the 2% pulse to pulse stability limits the SNR associated with this approach. By measuring the differential signal, the noise floor is reduced by over an order of magnitude enabling the detection of very weak signals. The differential spectrum is computed by first calculating the spectra of each time domain trace via FFT after proper windowing (see below).

Compared to conventional ultrafast pump probe measurements, the nature of the THz probe pulse can complicate the measurement process. For example, etalon effects from optical elements are much more pronounced when measuring the field of an electromagnetic wave rather than the intensity. At each interface of the SiC substrate, the optical pulse experiences a 22% intensity reflection, while the THz pulse experiences a 50% amplitude reflection. This leads to a round trip optical echo with only 5% of the peak intensity of the main pulse, but the THz echo will contain 25% of the peak amplitude. Each optical element will create echoes following the main pulse,

characterized by the round trip time inside the optical element. Experimentally, there are echoes at 6.8 ps, 15 ps, 21 ps, and 24 ps, originating from the SiC substrate, the photoconductive emitter, the ZnTe detection crystal, and the cryostat windows, respectively. Spectrally, these echoes create strong Fabry-Pérot oscillations in the transmitted spectrum. Fortunately, these oscillations can be minimized by properly windowing the data before Fourier transforming. Unless otherwise specified, a 14 ps Tukey window ($\alpha = 0.8$) was applied before calculating any displayed spectra. The normalized differential spectrum is then computed by taking the ratio of FFTs between the direct transmission ('pump off') and the differential signal.

In addition to monitoring the differential transmission spectra, it is often useful to measure the instantaneous differential transmission. Typically this would involve deconvolving the transmitted waveform with the incident pulse to recover the impulse response of the system. Fortunately, since the differential transmission is effectively dispersionless and the temporal waveform remains similar at all delays, quantifying the instantaneous graphene response only requires measuring the relative change in the peak of the transmitted THz waveform (rather than requiring spectral deconvolution), thereby reducing the real-time bandwidth requirements of the setup. Figure 3.6 shows the change in the peak transmitted THz ($t_{sample} = 0$). The upper panel shows the differential THz waveform normalized to the peak transmitted waveform (not shown) for different optical pulse delays. It's worth noting that the optical pulse delay is measured relative to the peak THz field, with *positive* delays indicating earlier arrivals. For example, in the top '+10 ps' trace, the optical pulse arrives at sampling delay -10 ps, or before the probe pulse. At early times, when the THz probe arrives before the optical pump, the differential signal is zero. As the pump delay is scanned forward, the differential signal turns on with the arrival of the optical pulse. The relative change in the peak THz signal is shown in the lower panel. As expected, before the arrival of the optical pulse, the differential signal is essentially zero, and quickly rises when the optical pulse and THz peak coincide. This is followed by an exponential-like recovery as the hot photoexcited carriers cool until a second impulse at 7 ps, which corresponds to the round trip time for the optical pulse within the SiC substrate. Experimentally we see secondary excitations

at 7 ps, 24 ps, and 200 ps, with the first two corresponding to secondary optical pump pulses from the SiC substrate and the cryostat window.

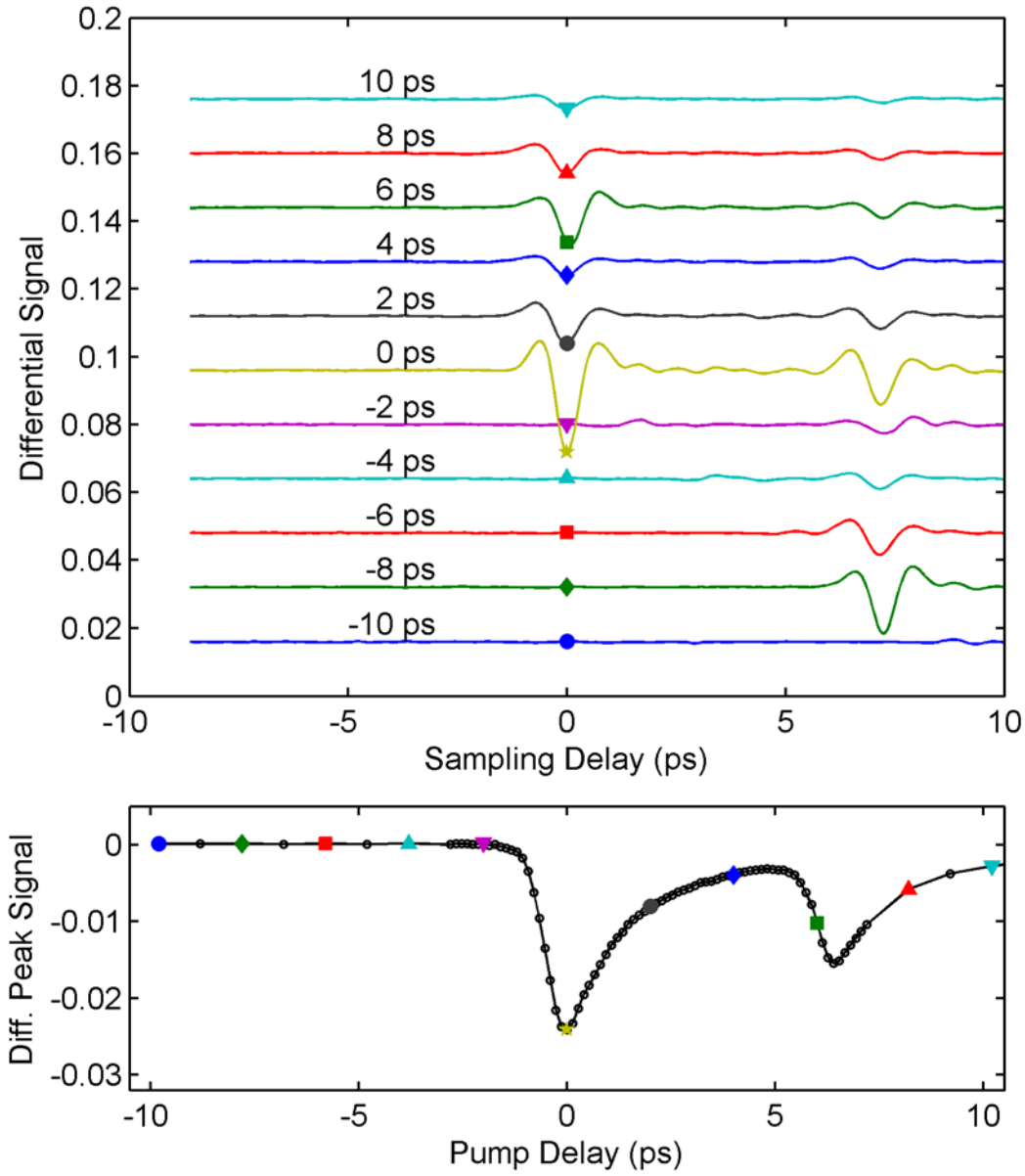

Figure 3.6 shows the normalized differential THz transmission at different pump delays on the #8B2 sample at room temperature in the upper panel. The lower panel shows only the change in the peak THz field ($t_{samples}$ = 0) as a function of the pump delay.

Graphene Transmission

Before measuring the THz recovery dynamics, it's helpful to examine the direct graphene transmission spectrum. For this data, the optical pump beam was blocked and a room temperature reference THz waveform was taken along with the transmitted THz waveform through the 63 layer sample and a blank SiC substrate as shown in the upper panel of Figure 3.7. The transmission spectrum in the lower panel was computed in the previously discussed manner.

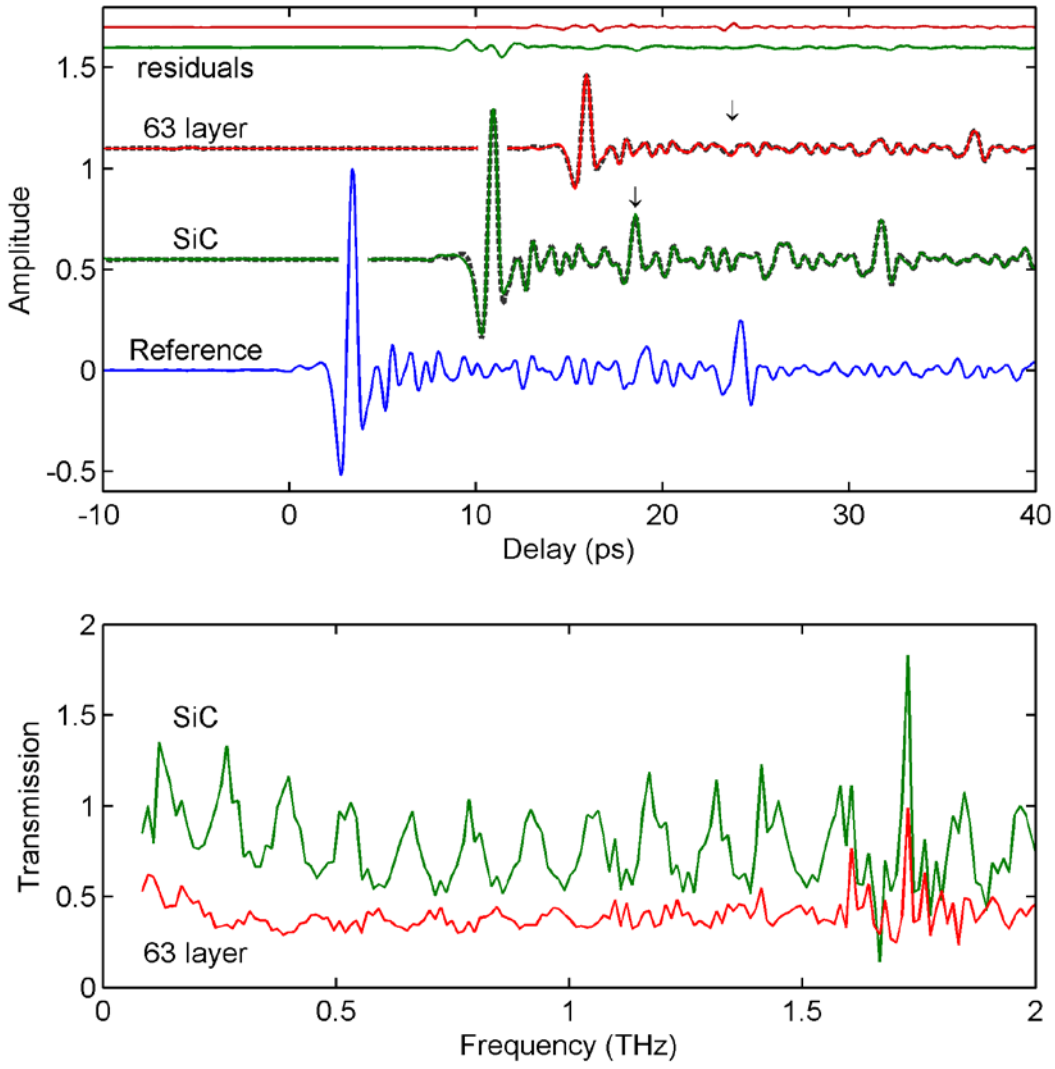

Figure 3.7 shows the transmission through the 63 layer #7J8 sample. The upper panel shows the transmitted time domain waveforms for the graphene sample and a separate blank SiC substrate. Fits to the two samples are shown by the thick dashed lines with the arrows indicating the 7.6 ps roundtrip THz echo. The lower panel shows the THz transmission spectrum for the two samples.

Measuring the graphene transmission was complicated by significant etalon effects in the SiC substrate. The bare SiC transmission shows deep oscillations at 130 GHz spacing, consistent with the 7.6 ps roundtrip echo in the SiC as indicated by the arrow in Figure 3.7. In order to separate the effect of the SiC substrate from the graphene transmission, the data was fit with a Fabry-Pérot transmission function. For an etalon at angle θ_i with amplitude reflection and transmission coefficients, *r* and *t*, at each interface the amplitude transmission is

$$t_{FP}(k_0) = \frac{tt\, e^{\frac{in^2 k_0 L}{\beta}}}{1 - rre^{i2k_0 L\beta}} \qquad (3.14)$$
$$\beta = \sqrt{n^2 - 1 + \cos^2(\theta_i)}$$

where L is the etalon thickness, k_0 is the free space wavevector at a frequency f, and n is the frequency dependent index of refraction. The above equation differs from the traditional Fabry-Pérot transmission formula in that the total phase accumulated by reflection within the etalon is used instead of only the phase difference between subsequent round trips.

The SiC and graphene transmission spectrum were fit simultaneously in the time domain with five free parameters: the substrate index of refraction n, the substrate thickness for each sample L_{bare} and $L_{graphene}$, and the graphene transmission $A_{graphene}$. The Fabry-Pérot amplitude transmission and reflection coefficients for each sample were calculated from the Fresnel reflection at a dielectric interface, except that the graphene etalon contained the equivalent of an additional single-pass reflection and transmission term, $t^2 = t_{graphene} \cdot t_{Fresnel}^2$ and $r^2 = r_{graphene} \cdot r_{Fresnel}^2$. The optimal fit required a 3.01 index of refraction, a 377.9 μm thick bare substrate, a 378.5 μm thick graphene substrate, and a 0.47 and -0.45 amplitude transmission and reflection coefficient, respectively. The time domain fits are shown as thick dashed lines under each data trace and the fitting residues are shown above the traces. The fits show excellent agreement with the data traces, and are very close to the expected *average* reflection and transmission coefficients 0.49 and -0.49, respectively.

A potentially more robust method for measuring the graphene transmission was used by Choi et al. [86]. Rather than measuring the direct THz transmission, the graphene transmission is measured relative to a bare SiC substrate. The advantage arises from using a single spatially modulated graphitized/bare sample. By translating the graphitized section into and out of the THz beam and using a lockin amplifier tuned to the modulation frequency, the graphene transmission relative to the bare SiC substrate can be measured with a high degree of accuracy. For comparison, the normalized graphene transmission for the 63 layer sample (#7J8) is shown in Figure 3.8. Unlike the previous work, the samples available for this work are much smaller; 3mm x 4 mm vs. 5 mm x 12 mm. The small sample size in conjunction with the large THz probe diameter prevented us from using a single partially graphitized substrate. Instead, separate transmission curves for bare and graphitized samples were measured and then numerically divided.

Identifying a Bandgap Using THz Transmission

One of the primary unanswered questions about epitaxial graphene is whether a bandgap exists in the undoped layers. Does the linear dispersion shown in Figure 3.2 extend to the Dirac point, or is there a potential bandgap opening with a separation on the order of a few meV? Ab initio density function calculations show a substrate-induced band gap in single layer graphene on hexagonal boron nitride [100]. Similar calculations on few layer SiC epitaxial graphene show that any defects that break the symmetry between the A and B sublattices can also give rise to a bandgap [101]. Experimentally ARPES measurements on few layer epitaxial graphene showed a substrate induced bandgap opening that rapidly closes with a few layers. For single to triple layer epitaxial graphene, the bandgap decreases from 260 meV, to 140 meV, to 66 meV [102, 103]. For thick samples the bandgap is expected to be 8 meV or less.

Using the method outlined in the previous section, a comparison between the normalized direct graphene transmission and a theoretical model is also shown in Figure 3.8. The theoretical transmission is computed using the thermoconductivity model by Gusynin (simplified form Eq 3.2, full form [82]) and the conductivity dependent transmission (Eq. 3.13). At low temperature, the data is best fit by assuming a small

bandgap opening, $\Delta_{\text{half gap}} \approx 2$ meV, and a slight 10% increase in the total conductivity. However, the qualitative agreement disappears at room temperature. The disagreement is likely explained by an experimental error in measuring two different samples. As discussed in Appendix B, at frequencies below 300 GHz, the probe spotsize approaches the sample diameter. Any misalignment of the sample will manifest as a change in the amplitude transmission at low frequencies. *In contrast, a negligible bandgap is predicted (<1 meV) if the fitting is limited to the flat spectral response above 500 GHz, where the probe spot size is sufficiently small.* In order to overcome the experimental difficulties associated with direct transmission measurements, optical pump – THz probe techniques were used to measure the differential spectra of a single sample.

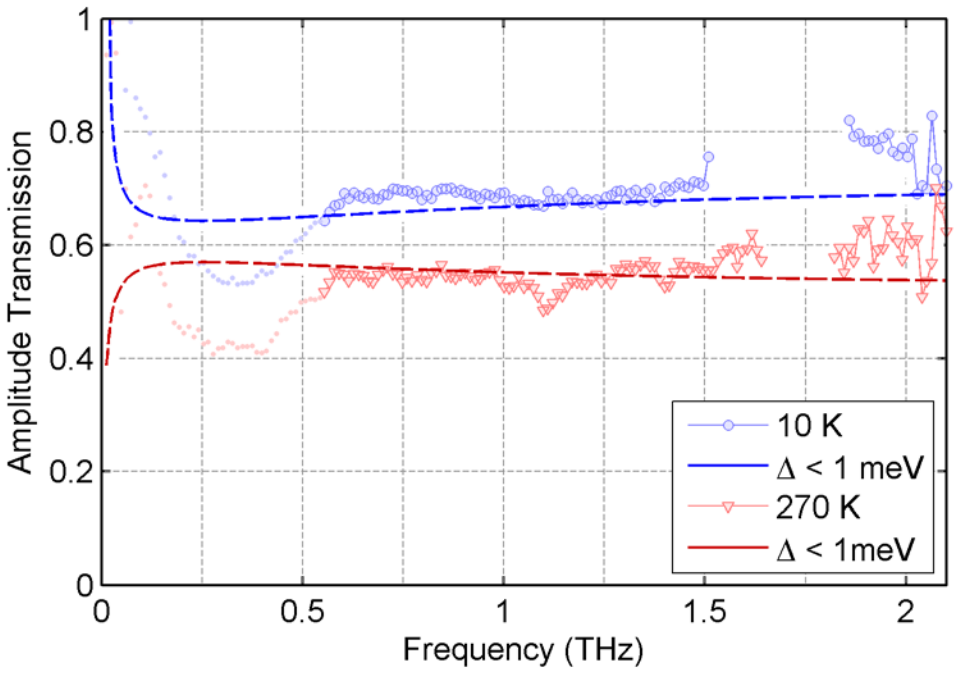

Figure 3.8 show the amplitude transmission of #7J8 (63 layers), normalized to the bare SiC substrate at low and near-room temperature. Fabry-Pérot oscillations from the SiC substrate have been numerically removed (Eq 3.14). The dashed line shows the predicted transmission from the thermoconductivity model by Guysnin (simplified form Eq 3.2)

To address the limitations of the direct measurements, the differential THz transmission was measured between 200 GHz and 2 THz (0.8 meV to 8.25 meV) from 10K to 300K (k_BT = 0.8 meV to 25 meV) and with optical pumping between 0.1 μJ/cm^2 and 30 μJ/cm^2. The interband contribution to the differential signal is expected to be negligible at probe energies below the bandgap and the intraband contribution, which is

spectrally flat, is weaker at cold temperatures. These effects combine to produce a step in the transmission function which should be more pronounced at lower lattice temperatures and higher carrier temperatures (stronger pumping).

The differential transmission of the 63 layer sample (#7J8) is shown in Figure 3.9. Each of the six panels shows the differential transmission at a fixed substrate (lattice) temperature and at different optical pump delays: 0, 10, 30, 60, 120, and 500 ps. At room temperature, the differential spectrum is flat although the lower signal magnitude and relatively hot initial carrier distribution could mask the appearance of a bandgap. As we move to colder lattice temperatures, the differential spectrum remains uniform even at cryogenic temperatures. At 40 K, the average magnitude at 0 ps has increased by 8 fold to 20%, indicating a strong modulation of the carrier density and temperature, however the differential spectrum still remains flat. The anomalous spike at 1.8 THz corresponds to a strong water vapor absorption line and is attributed to a temporary increase in the humidity when the 40K reference transmission trace was taken.

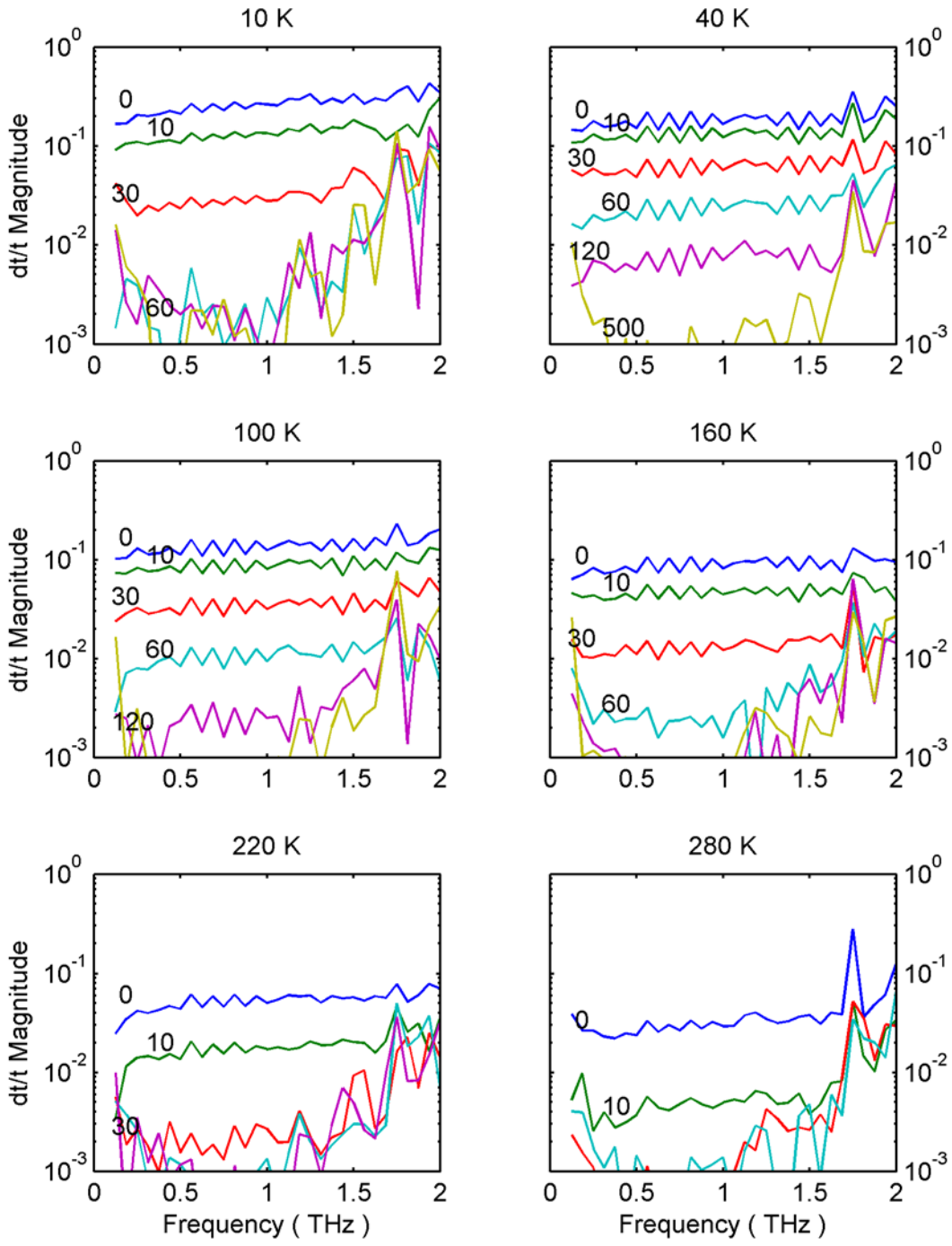

Figure 3.9 shows the differential spectrum of the 63 layer sample (#7J8) with a 100 mW optical pump.

At 10 K, there appears to be a reduction in the differential signal at low photon energies as one would expect for a bandgap. Unfortunately this is likely due to experimental error. First, the slope is much too shallow, which would indicate a lattice temperature much warmer (~100 K). Second, the same effect can be achieved by

uncorrected thermal expansion (or contraction) of the cryostat cold finger. As discussed in Appendix B, the probe spotsize at low frequencies easily exceeds the sample aperture (2 mm diameter). If the sample alignment drifts between the reference trace and the differential scans, the most pronounced effect is a change in the low frequency transmission. Using the same thermoconductivity model as before, but calculating the differential transmission the upper limit of the bandgap can be estimated. Despite the anomalous readings at 10 K, the data places a 0.7 meV upper limit on the potential bandgap size.

THz Transmission Recovery Dynamics

Measurements of the ultrafast recovery of photogenerated carriers in epitaxial graphene can potentially reveal important information about the interband and intraband carrier relaxation dynamics. Measurements with degenerate [88] and non-degenerate [89] probes in the near- and mid-infrared have revealed interesting dynamics associated with the interband conductivity recovery in the doped and undoped layers. Furthermore, recent work by George [98] on 6H-SiC epitaxial graphene samples showed disorder enhanced recovery rates at very low probe energies. Additional measurements by Choi et. al. [86] similarly showed an accelerated recovery rate which was also attributed to sample disorder. In this section, we expand on the previous optical pump / THz probe experiments by extending to higher pump intensities, measuring the recovery temperature dependence, and correcting methodology problems in the original work.

In the work by George et. al., 6H-SiC graphene samples were pumped by low energy pulses from a Ti:sapphire oscillator running at 81 MHz. For experimental simplicity, the researchers elected to use a non-normal incidence pump at 15° angle to the sample, with a sub-400 μm pump spot in the sample plane. The peak observed differential transmission signal was 0.9% with a 37 layer sample, and the dynamics showed a rapid recovery. From an experimental standpoint, the high repetition rate of the system forced non-optimal compromises in the experimental design. First, the low pulse energy requires tight focusing in order to achieve moderate pump fluences. Under these focusing conditions, the probe spot would be comparable to the pump spot at frequencies above 2 THz; however for a majority of the probe bandwidth, the pump spot is several

times smaller than the probe, leading to a nonuniform excitation across the probe spot. Second, the small 15° pump beam angle of incidence is acceptable for shorter wavelength probes where the probe diameter is < 50 µm; however with larger spots, there is a noticeable arrival time difference between the left and right edges of the pulse. At 15°, the temporal walkoff between the right and left edges of the beam is greater than 300 fs, significantly exceeding the claimed 50 fs temporal resolution of the system [97]. Lastly, part of the nonlinear pump power dependence may be explained by the high heat load on the sample. For the thicker 37 layer sample, the peak pump power was 1300 mW of which the sample *absorbed* over 750 mW. With such a high heat load concentrated in such a small spot, it's likely that the substrate and lattice temperature varied significantly with the pump power.

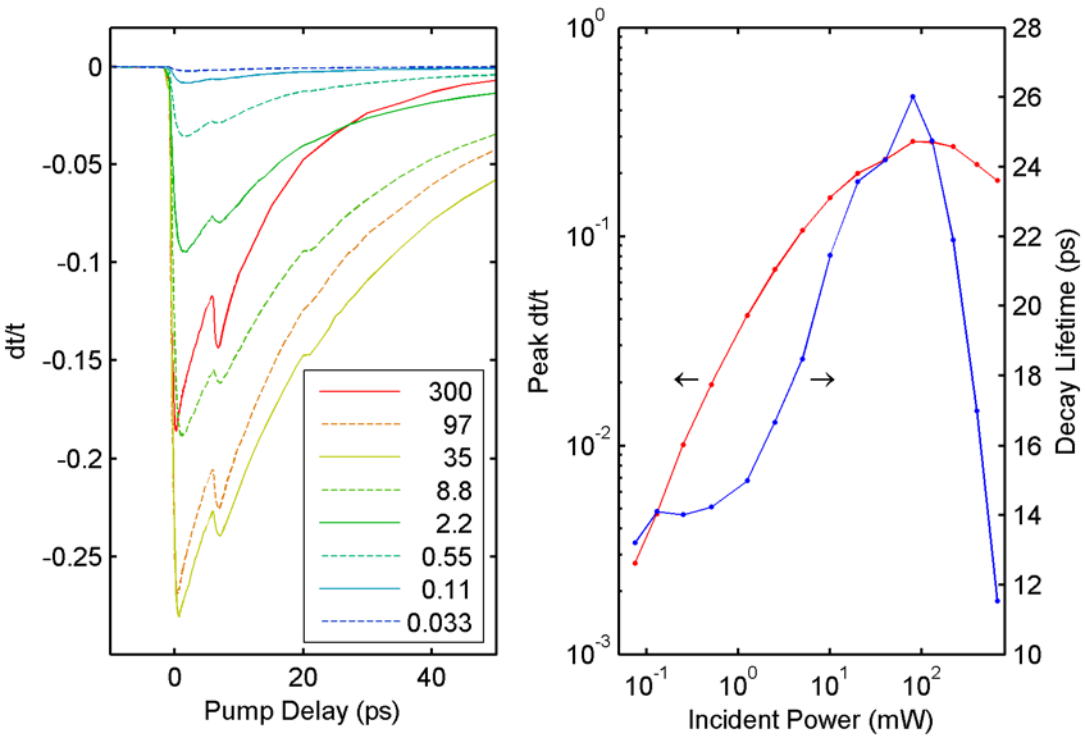

Figure 3.10 shows the effect of high average pump power on sample heating. The left panel shows the normalized differential transmission at several average pump power levels (in mW) at 80 K. The right panel shows the peak differential signal (left axis) and decay rate (right axis) for each curve in the left panel.

To measure the effect of sample heating in our experiment, the peak differential transmission through the 63 layer sample was measured at 80 K using liquid nitrogen (LN_2). The liquid nitrogen flow rate was double over typical levels and a shield was

placed around the cryostat exhaust to deflect the stream away from the surrounding optics. The cryostat thermocouple was removed from the cold finger and thermally fixed to the sample holder using low temperature vacuum grease. Due to the high LN_2 flow, the sample holder temperature was stable at 77K for all pump levels. Figure 3.10 shows the normalized differential transmission through the 63 layer sample at increasing pump powers. As expected, after excitation there is a rapid reduction in the THz transmission, followed by an exponential-like recovery. The peak reduction (at $t_{pump} = 0$), and recovery rate for the first 40 ps is shown in the right panel. Beginning with low pump power, we see a linear increase in the differential transmission with increasing pump power, while the recovery dynamics show a similar recovery lifetime. Interestingly, above 1 mW average power ($\sim 1\ nJ / mm^2$) we still see a linear scaling with pump intensity, but the recovery dynamics begin to slow down. However as we approach and exceed 10 mW we see a rapid reduction in the differential signal and the recovery lifetime. As later data will show, this is consistent with an elevated lattice and substrate temperature, despite the high LN_2 flow rate *and* the stable temperature of the sample holder. To reduce the effects of high pump average power in our experiment, the system repetition rate was reduced to 50 kHz and the maximum heat load was limited to 3 mW.

Figure 3.11 shows the THz transmission recovery dynamics of sample #7J8. As before, following the initial rapid reduction, the transmission recovers at a rate that is dependent on the pump power and substrate temperature. At high pump fluence, the secondary excitation at 6.5 ps is more apparent. A similar secondary excitation at the same time delay is observed in optical pump – mid-IR probe experiments and is attributed to Fabry-Perot pump reflections inside the SiC substrate [104]. At room temperature, the differential signal fully recovers within 20 ps, which agrees well with early prior experiments by Choi and George. However as we cool to colder lattice temperatures and excite to higher initial carrier temperatures, the recovery stalls and a second slow recovery process appears. At the highest incident power ~15 mW, the pump fluence is approximately twice the fluence used by George et al. and Choi et. al.; however the peak room temperature differential signal is an order of magnitude higher (15 x). This large discrepancy is likely due to a combination of sample quality in the work by Choi et al. and experimental limitations in the work by George et. al.

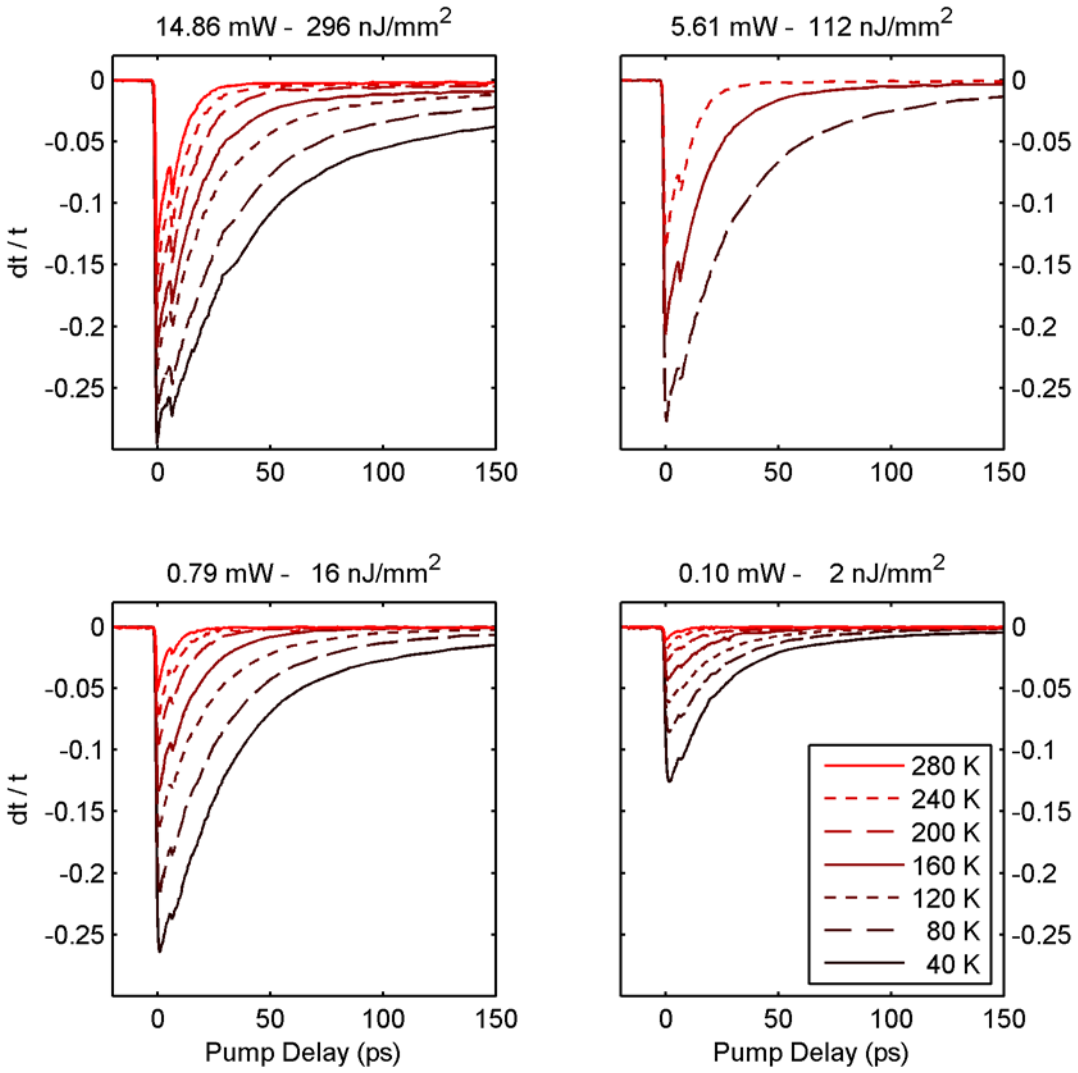

Figure 3.11 shows the THz transmission recovery dynamics of sample #7J8 (63 layers), at different substrate temperatures and pump power.

Prior experiments by Choi and George showed room temperature recovery dynamics that are well represented by a single exponential lifetime. Figure 3.12 shows the least squares fit to the differential signal using a single exponential, stretched exponential and biexponential fit. At room temperature, the recovery is well characterized by a single exponential recovery, in agreement with prior results. However at colder lattice temperatures, the long recovery tail requires a biexponential to fit the data accurately. At 20 K, the normalized RMS residual errors for a single, stretched, and biexponential are: 1, 0.5, and 0.04, respectively.

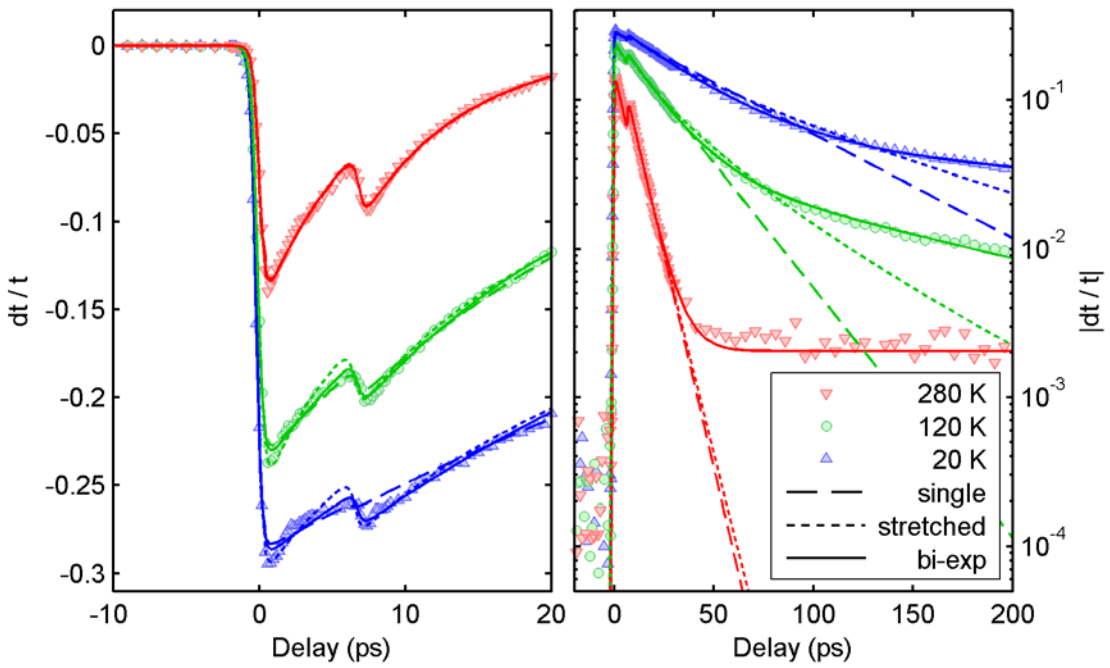

Figure 3.12 shows phenomenological fits to the THz transmission recovery dynamics at 14 mW average pump. All three fits agree with the dynamics near time zero (left panel), however only the biexponential agrees at long delays and cold substrate temperatures (right panel)

As the prior work has identified, accurately reproducing the graphene recovery using theoretical models is difficult due to inhomogeneity within a single sample and even larger variations between samples. However we would expect appropriate models to be able to replicate the observed trends in the data. For comparison, the biexponential fitting parameters for a subset of measured conditions are shown in Figure 3.13. Beginning at room temperature, the peak differential reduction increases with decreasing lattice temperature and increasing initial carrier temperature, with a peak differential signal exceeding 30%. While our samples showed significantly stronger differential transmission, the room temperature recovery rates are in general agreement with previous work; Choi: 2.5 ps, George: 3.0 ps. Interestingly, as the initial lattice temperature is reduced, the recovery process slows significantly, and below 200 K a second much slower process appears.

Two competing theoretical models for the recovery of hot photoexcited carriers have received significant attention. Ideally the predicted recovery based on either the carrier recombination or phonon cooling could be matched to the observed recovery. However attempts at numerically evaluating both models produced highly non-exponential

recoveries. The Auger recombination model predicts an initial fast recovery with lifetimes between 1 and 30 ps for carrier concentrations above 10^{10} cm^{-2}. On the other hand, the acoustic phonon emission model predicts a two part recovery, although with much longer lifetimes. Following an initial 'fast' power-law recovery with lifetimes as short as 50 ps, the recovery shifts to an exponential decay with a lifetime exceeding several nanoseconds. Comparing these predictions with the recovery lifetimes observed in Figure 3.13, it is apparent that each model different aspect of the data. Near time zero, the rapid recovery is consistent with Auger recombination, in agreement with previous work [98]. However at colder temperatures and long delays, the recovery is more consistent with energy loss due to phonon emission. Additionally, the appearance of the slower recovery component occurs very close to the predicted onset of acoustic phonon cooling (180 K), although this is likely due to the particular SNR of the system and the strength of the slow recovery at room temperature.

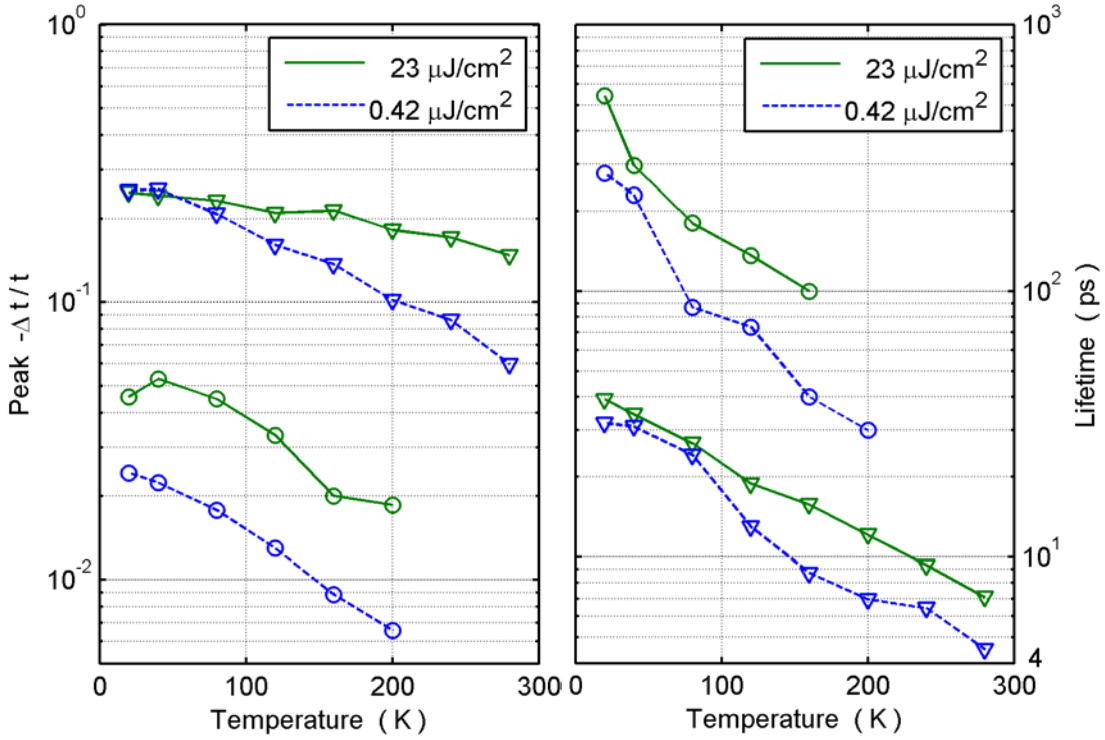

Figure 3.13 shows the biexponential fit parameters to differential transmission of the 63 layer sample (#7J8, Figure 3.11). The left panel shows the amplitude of the fast (triangle) and slow (circle) components. The right panel shows the associated recovery lifetimes. Above 200 K, the amplitude of the slow component is less than 5% of the fast component and quickly sinks below the SNR of the experiment.

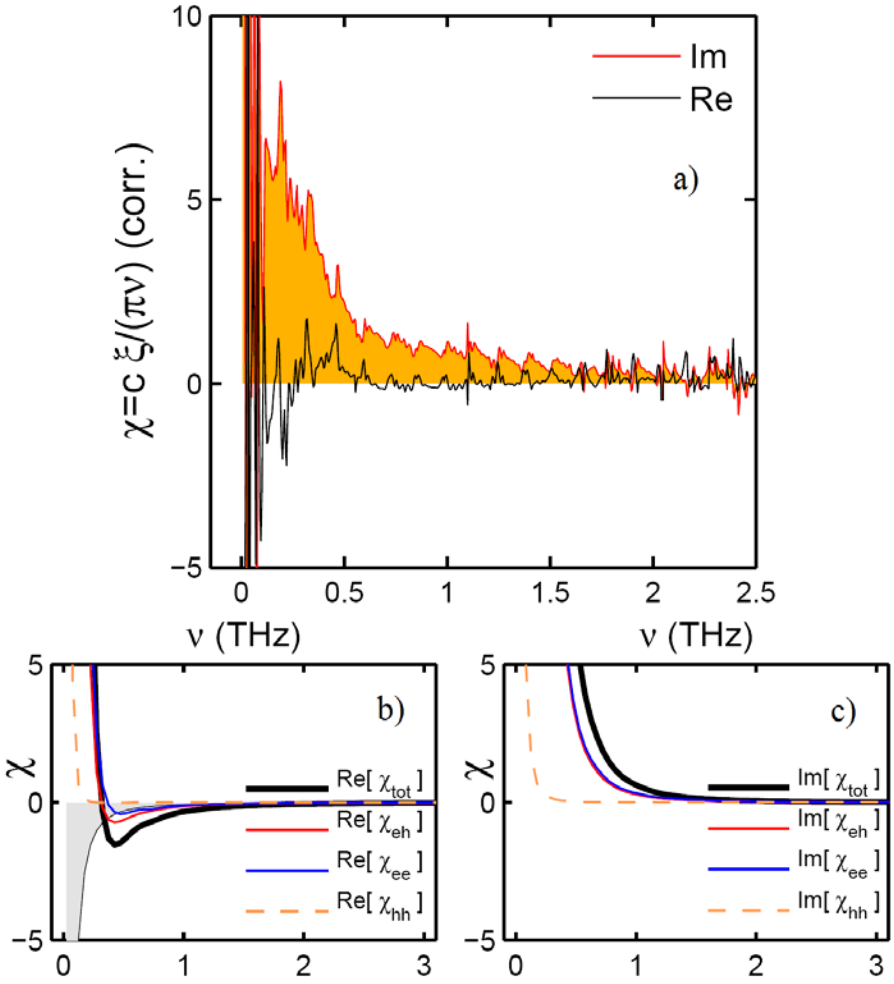

Figure 3.14 show a comparison between the measured susceptibility and results from microscopic simulations. The real and imaginary part of the susceptibility is shown in the top panel. The real and imaginary parts of the computed susceptibility are shown in the lower panel, broken down by carrier-carrier interaction.

In addition to the above models which assume thermal distributions, calculations based on density matrix theory are able to incorporate many body effects and non-thermal distributions. Figure 3.14 shows a comparison between the measured susceptibility $\chi(f) = -i\frac{c}{\pi L f}\frac{\Delta E(f)}{E(f)}$, and a microscopic calculation based on the experimental conditions by Hanno et. al. [94]. As before, the strong Fabry-Perot oscillations in the measured spectra were numerically removed leaving small residual oscillations in the measured spectra with ~70 GHz spacing. Comparing the results to the simulated susceptibility, both the imaginary and real parts of the susceptibility show a strong qualitative agreement.

Low Threshold Nonlinear THz (linearity check)

In the past two years, recent advances in the generation of broadband single cycle THz pulses have created focused field strengths exceeding 100 kV/cm [26]. These newly accessible fields have allowed researchers to probe cascaded generation and other nonlinear processes, that had only been theoretically modeled before [105]. Even in crystals with exceptionally large nonlinear coefficients like $LiNbO_3$ the changes on the pulse shape induced by harmonic generation and self phase modulation are barely perceptible. Interestingly, the predicted nonlinearity in graphene is orders of magnitude larger than conventional optical rectification crystals.

Theoretical modeling by Mikhailov [106] using a self consistent electromagnetic field for propagation and quasi-classical kinetic model for graphene's response, predicts a significantly lower threshold for nonlinear effects. At room temperature the threshold for harmonic generation in the undoped layers is only 200 V/cm. The threshold scales with the square root of the electron density, so the threshold should remain low for all but the bottom few layers which require a few kV/cm for harmonic generation. However, the quasi-classical approach essentially ignores interband contribution to the dynamic conductivity, which is only valid when $\hbar\Omega \ll \max\{\mu, T\}$, where Ω is the central frequency of the radiation and μ is the chemical potential of the graphene layer.

As shown in previous sections, the transmission spectrum of graphene is remarkably gray and featureless. However as a check for nonlinearity, we monitored the peak graphene transmission and differential signal as a function of the incident field strength. In order to increase the incident field strength, the laser repetition rate was dropped to 50 kHz and the photoconductive emitter bias was increased from 10 V to 20 V. Since broadband neutral density THz filters are generally unavailable [107], and changing the electrical bias changes the THz spectrum [108], the incident field strength was adjusted by controlling the optical pump to the THz emitter. At each pump level, the transmission was measured with and without the 63 layer sample (#7J8), and the results are shown in the left panel of Figure 3.15. The absolute field strength in the left panel was calibrated by measuring the average THz power and beam diameter using the liquid helium bolometer and an iris. The indicated peak field represents a worst case scenario, by

assuming a top hat distribution with a radius larger than the real distribution. If one uses the real distribution as measured in Appendix B, the peak on-axis field at focus is 300 V/cm instead of the indicated 160 V/cm.

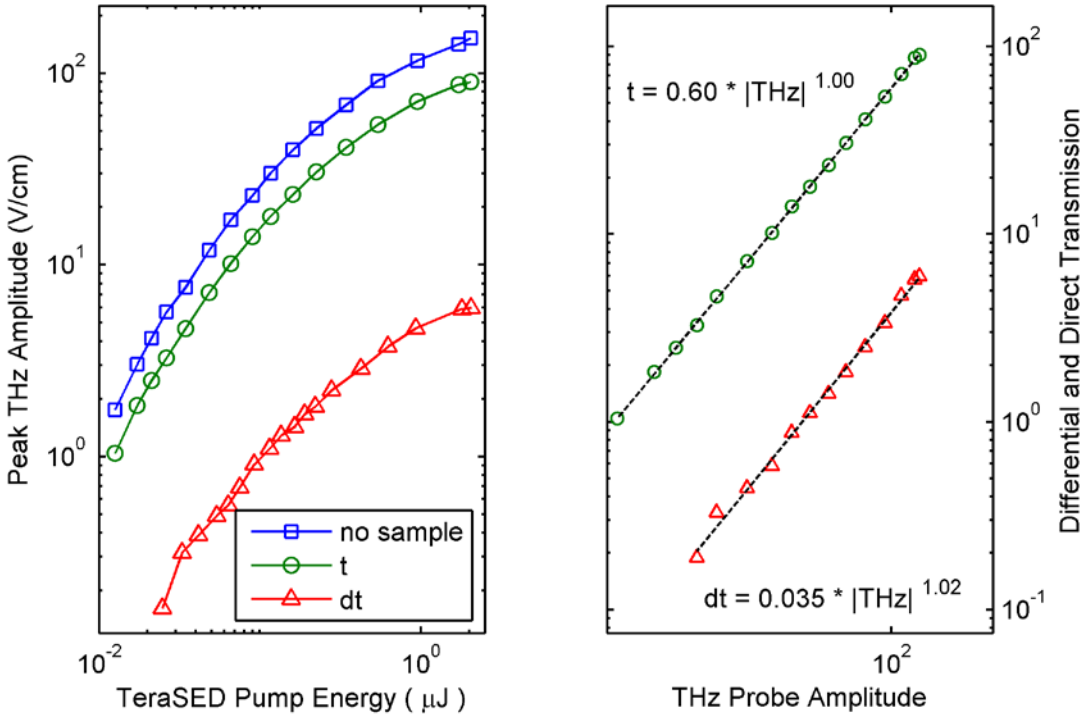

Figure 3.15 shows the linearity of the transmitted THz from #7J8 at 290 K. The peak transmitted amplitude as a function of the THz emitter pump is shown in the left panel. The right panel shows the ratio of the direct and room temperature differential signal

The nonlinear dependence on the optical pump energy can be factored out by taking the ratio between the direct or differential transmission and the reference transmission, as shown in the right panel. Disappointingly, both the direct and differential graphene transmission is highly linear even as we approach the threshold for nonlinearity. There are several possible reasons we didn't see the expected nonlinearity. First, multiple nonlinear process could cancel in a way that maintains the peak field. Second, the bolometer could be off and we could be grossly over-estimating the average power and consequently the peak field. However this would imply that the power measurements from the GaP waveguide generation were also exaggerated, which is unlikely since they agreed well with theory and the measured power was in agreement with other measurements based on pyroelectric energy meters [26]. Lastly, the most likely

explanation is that the experimental conditions violate an implicit assumption in the calculations by Mikhailov.

Sample Dependence

The samples used in this thesis are all epitaxially grown on 4H-SiC substrates. During the course of experiments, we received four different samples, beginning with the first arrival: #7J8 (63 layers), #1133 (35 layers), #8B2 (9 layers), and #1104 (13 layers). The first sample was received nearly a year before the other three and the vast majority of experimental data is taken with this sample. Due to the large time gaps between samples, the sample variation arises not only from natural variations in fabrication, but from an evolution of the fabrication methodology itself. Continual refinements to the fabrication process including better characterization of the initial SiC substrates, improved vacuum furnace control and a much better understanding of the optimal growth conditions, which led to the fabrication of samples with vastly different behavior. Oddly, of the samples, #7J8 was the most homogeneous and repeatable despite its earlier fabrication. Perhaps the improved performance is due to the thickness since the defect density tends to decrease with increasing thickness [101], or perhaps this sample was uncharacteristically good.

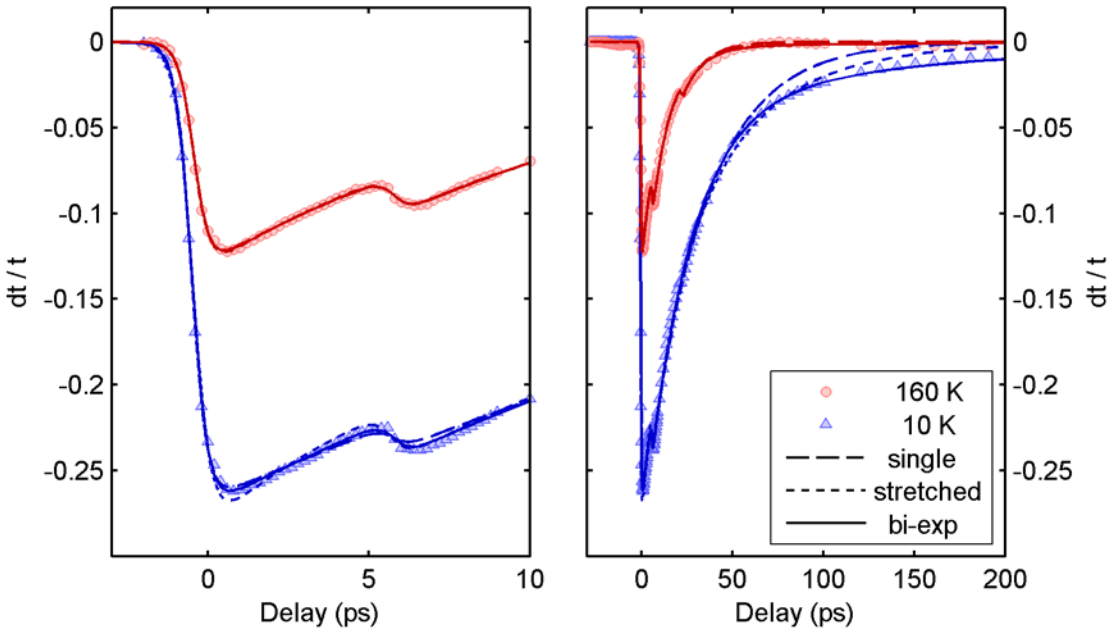

Figure 3.16 shows the recovery dynamics for the 35 layer sample (#1133).

As the sample thickness decreases, fitting the recovery dynamics becomes more difficult. The weaker signal and stronger Fabry-Perot echoes reduce the accuracy in the fitting, especially for the slow recovery process. The recovery dynamics and fit parameters for sample #1133 (35 layers) are shown in Figure 3.16 and Figure 3.17, respectively. Comparing the recovery parameters to the thicker 63 layer sample, it's apparent that in addition to the weaker signal, the recovery process is ~4x faster. There are a number of possible reasons for the accelerated recovery. First, the ratio of undoped to doped layers is lower. Both the Auger recombination model and the acoustic phonon emission model predict faster recovery in the highly doped layers, and in thinner stacks the doped layers can contribute significantly to the THz response. Second, the quality of the thinner samples is lower. In situ measurements during fabrication indicate possible flaws in the hydrogen etch stage prior to graphitization. Prior work had shown that defects accelerate the recovery process [86, 98]. Extending the analysis to the thinner 13 and 9 layer samples shows the same trend of shrinking signals and faster recoveries. With further work and more samples, distinguishing between the true graphene response and individual sample variations should become more apparent.

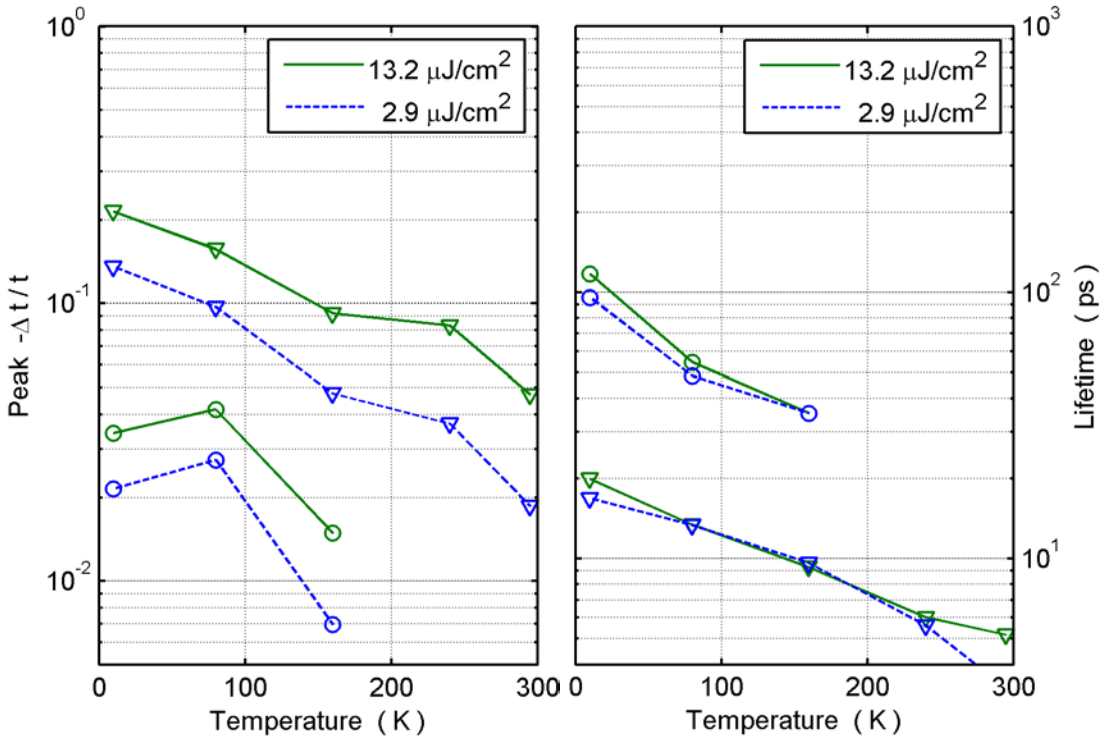

Figure 3.17 shows the biexponential fit parameters to differential transmission of sample # 1133 (30 layer). The left panel shows the amplitude of the fast (triangle) and slow (circle) components. The right panel shows the associated recovery lifetimes. Above 200 K, the amplitude of the slow component is less than 5% of the fast component and quickly sinks below the SNR of the experiment

Conclusion

For the first time, temperature dependence of the THz dynamic conductivity in high quality epitaxial graphene samples has been measured. Using the TD-THz differential spectroscopy system several important new properties have been identified. First, both direct and differential transmission measurements have reduced the upper limit for a potential bandgap opening from 10 meV to below 1 meV. Second, we have identified a new slow recovery process for the relaxation of hot carriers. The measured room temperature recovery dynamics are in general agreement with previous measurements and are well modeled by a single exponential recovery with lifetimes consistent with Auger recombination. However, at cryogenic temperatures and long delays, the observed slower recovery is more consistent with energy loss due to phonon emission. Lastly, we have begun to investigate the nonlinear transmission of graphene.

Chapter 4
THz Emission from Coherently Controlled Photocurrents in Epitaxial Graphene

In a conventional semiconductor when a carrier is photoexcited to the conduction band, the average carrier direction is uniformly distributed. As entire populations of carriers are excited, the individual momentums cancel and the net momentum of the population is zero. Optical coherent control is the process of controlling the net momentum of photoexcited carriers through interference of one- and two-photon absorption processes. By controlling the phase between these excitation pathways, the direction and magnitude of the net momentum can be controlled, giving rise to a measureable macroscopic current.

Historically, optical coherent control was demonstrated as early as 1964 in discrete energy level systems, [109-115] and was eventually exploited in molecules with intention of manipulating chemical reactions [116-122]. Later optical control of discrete to continuum transitions was demonstrated in quantum wells [123] and extended to continuum-to-continuum transitions in bulk GaAs [124, 125]. Optical coherent control in indirect bandgap semiconductor like silicon has also been demonstrated experimentally recently using a THz detection technique [126].

Although coherently controlled photocurrents have been demonstrated in a variety of materials, ballistic photocurrents in epitaxial graphene have a number of compelling advantages. First, due to the symmetry of the graphene lattice, the direction of the injected current can be fully controlled by adjusting the polarization of the fundamental (ω) and second harmonic (2ω) fields [127]. Second, quantitative studies of the magnitude and dynamics can serve as a confirmation of mid-IR pump-probe measurement of hot photoexcited carrier scattering properties. Third, the method provides the means for ballistic current injection without electrical contacts.

Theory of Coherent Photocurrents in Graphene

Optical coherent photocurrents can be understood in terms of interference between two excitation pathways. Electrons are excited by single- or two-photon transitions to states of different parity. These symmetric and antisymmetric wave-functions can in turn interfere constructively in one spatial direction and destructively in the other direction depending on the relative phase between the processes.

Calculation of the coherent current in graphene using the tight-binding approach has been done separately by Rioux et al. [128] and E. J. Mele et al. [127]. The bandstructure of graphene, can be described by the effective Hamiltonian

$$H_{\text{eff}} \rightarrow v_f \begin{pmatrix} 0 & \hbar k_- \\ \hbar k_+ & 0 \end{pmatrix} \tag{4.1}$$

where the wavevector is defined as $k_\pm = k_x \pm ik_y$. This model leads to linear energy bands $E(\boldsymbol{k}) = \pm v_F \hbar k$, where v_f is the energy-independent Fermi velocity and is typically on the order of 10^6 m/s.

In the tight-binding model, it is possible to calculate the optical absorption tensor, ξ, which is related to the imaginary part of the susceptibility by $Im[\,\chi(\omega)\,] = \frac{\hbar}{2}\xi_1(\omega)$. Beginning with the matrix elements above and applying Fermi's golden rule, the single photon absorption is given by $\dot{n}_1 = \bar{\xi}_1(\omega)|E_\omega|^2$, where $\bar{\xi}_1$ is defined as

$$\bar{\xi}_1(2\omega) = \frac{g_s g_v e^2}{8\hbar}(2\hbar\omega)^{-1} \tag{4.2}$$

The spin and valley degeneracies, g_s and g_v, are both equal to 2 for graphene. Similarly, The two photon absorption tensor is given by,

$$\bar{\xi}_2(\omega) = g_s g_v 8\hbar e^4 v_F^2 (2\hbar\omega)^{-5}. \tag{4.3}$$

While the single photon absorption rate is polarization independent, the two-photon absorption depends on the ellipticity of the incident light. Assuming a general elliptical polarization, $E_\omega = \frac{1}{\sqrt{2}}E_x\left(\hat{x} + \hat{y}e^{i\Delta\phi}\right)$, the two photon absorption rate is given by,

$$\dot{n}_2 = \bar{\xi}_2(\omega)|E_\omega|^4\left(1 + \sin\left(\Delta\phi_{ellipticity}\right)\right) \tag{4.4}$$

Interestingly, stronger ellipticity increases the two photon absorption and, in the limit of circular polarization $\left(\Delta\phi_{ellipticity} = \pm\frac{\pi}{2}\right)$, the absorption is two times greater than the absorption of linearly polarized light. The interference between one and two photon processes gives rise to the coherently controlled current. The coherent current generation rate, $\dot{\mathbf{J}}$, is given by,

$$\dot{J} = 2|E_\omega^2 E_{2\omega}^*|\,\eta_I(\omega)\ (\sin\Delta\phi)\ \left[\hat{e}_{2\omega,\parallel}\cos 2\theta + \hat{e}_{2\omega,\perp}\sin 2\theta\right], \qquad \eta_I(\omega) = i\, g_s g_v e^4 v_F^2 (2\hbar\omega)^{-3} \tag{4.5}$$

where $\eta_I(\omega)$ is the corresponding tensor component, $\Delta\phi = 2\phi_\omega - \phi_{2\omega}$ is the relative phase between the fundamental and second harmonic beams, θ is the angle between beam polarizations, and $\hat{e}_\perp$ and $\hat{e}_\parallel$ denote unit vectors relative to the second harmonic polarization. Unlike other materials, the symmetry of graphene allows for significant cross polarized interference. As can be seen from equation 4.5, both parallel and orthogonal polarized pump beams generate identical coherent currents, while the orthogonal coherent current is maximized when the beams are polarized at 45° with each other.

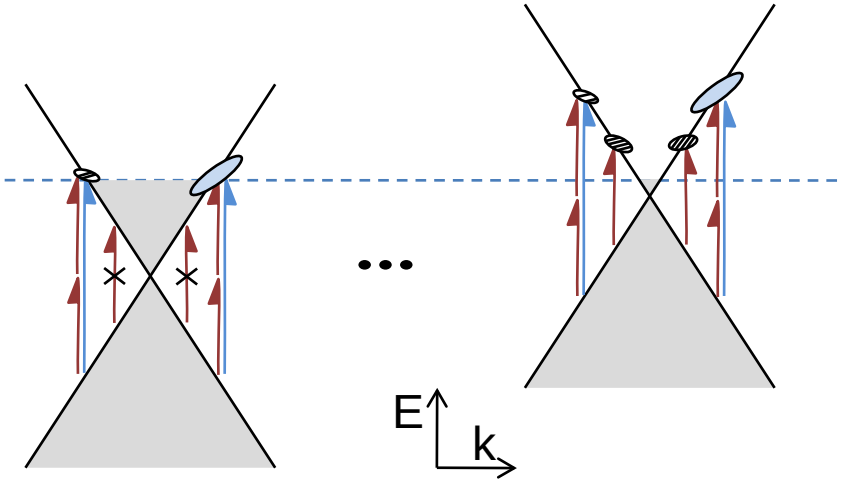

Figure 4.1 shows the band diagram of the bottom heavily doped (left) and upper 'undoped' layers (right) of epitaxial graphene near the Dirac point. Photons at the fundamental and second harmonic frequency are shown by dark red and light blue arrows, respectively. The asymmetric electron populations at $\pm k$ are indicated by shaded ovals with solid ovals indicating 'good' electron populations and hatched ovals indicating 'bad' electron populations. The dashed line shows the shared Fermi level of doped and undoped graphene layers.

One area of interest is the qualitative difference between photocurrents in the lower doped layers and upper undoped layers. In doped layers, carriers will be excited via the two higher energy processes: $\dot{n}_2$, and $\dot{\mathbf{J}}_I$, while in intrinsic graphene layers, carriers will be excited via all three processes: $\dot{n}_1, \dot{n}_2$, and $\dot{\mathbf{J}}_I$. Carriers excited through either one-photon or two-photon absorption alone will contribute to a stagnant background carrier density that will reduce the average excited carrier velocity. These 'bad' electron populations which negatively impact the coherent control signal are shown as hatched ovals in Figure 4.1, while the good populations are shown with solid ovals. We can define the average, or swarm velocity of an entire population as,

$$v_{swarm}(\omega) \equiv \frac{\dot{J}_I}{e\dot{n}} = \frac{e^{-1}\eta_I(\omega)}{x\xi_1(2\omega) + x^{-1}\xi_2(\omega)}\,\hat{\jmath}, \tag{4.6}$$

where $x = |E_{2\omega}|/|E_\omega|^2$, and $\hat{\jmath}$ is a unit vector in the direction of the coherent velocity (Eq. 4.5).

The above analysis assumes a monochromatic steady-state operation; however the intensities required for efficient two-photon processes are generally only achievable in pulsed systems. Since the detection system is highly dependent on the dynamics of the

coherent current pulse, a qualitative treatment of the dynamics can be very helpful. Intuitively, one would expect the leading edge of the current pulse to rise with the optical pulses and decay at a rate governed by the intrinsic properties of the medium. For graphene, several processes affect the decay rate. On sub-picosecond time scales, carrier-scattering and phonon processes dominate, while on longer time scales, space-charge effects potentially become important.

Measurements of the carrier-carrier scattering rate have been performed in both exfoliated [129] and epitaxial graphene [88]. In both systems, the measured scattering lifetime is below 100 fs at carrier densities of 10^{10} cm^{-2} and above. Fortunately, elastic e-e and h-h scattering does not change the net momentum of the swarm and hence the coherent current. On the other hand, the phonon scattering lifetime is expected to exceed several ps. For phonon scattering, the linear dispersion of graphene is advantageous over conventional semiconductors; only phonon scattering events where carriers undergo a large change in direction will affect the coherent current. Inelastic scattering with long-length scale disorder will be suppressed in graphene due to the conservation of pseudospin freedom. As suggested by Auston and Kaiser [130], the photocurrent lifetime may be much longer than any of the previous scattering times because only certain collision events will cause the swarm momentum to decay.

In addition to phonon and impurity scattering, the coherent current is expected to decay through the evolution of space-charge fields. Although we typically focus on electrons as the exclusive charge carriers, the band symmetry of graphene indicates that holes should generate an identical population counterpropagating with the electrons. As the oppositely charged carriers separate, an electric field is created that resists this motion. The effect should increase at higher excitation levels as larger populations participate. In a low resistivity material like graphene, the effect should manifest as a suboptimal power scaling and a power dependent THz waveform.

Several methods have been proposed for detecting the coherent current. In high resistivity materials, such as low temperature grown GaAs (LT-GaAs), the space-charge phenomena can be exploited to measure the coherent current. By focusing the optical beams between two closely spaced electrodes, opposite charge will accumulate at the

electrodes, leading to a measurable potential difference [131]. However the large minimum conductivity of graphene prevents macroscopic charge buildup. An alternative method for low resistivity materials was used by Cote et al. [132]; rather than integrating the total charge transfer, one can look for radiation from the rising and falling edges of the current pulse. For ultrafast optical pulses, the current magnitude tracks the optical pulse envelope. The rapid rise in the current generates an electromagnetic pulse at THz frequencies. Recently, this technique has been applied to thin graphite films, and the resulting photocurrent was much weaker than conventional semiconductors [77], which lead the authors to speculate about the feasibility in few layer graphene.

Experimental Setup

One of the primary difficulties for generating coherent photocurrents is maintaining a stable phase relationship between the fundamental and second harmonic pulses. For pulsed laser sources, the relative phase, $\Delta\Phi$, needs to remain constant across the full duration of the pulse pair. Furthermore, increasing SNR through signal averaging or lockin techniques requires a stable $\Delta\Phi$ from one pulse pair to the next. The first criterion is achieved by frequency doubling a fundamental pulse in a phase-matched crystal. Any dispersion on a fundamental pulse will be replicated in the second harmonic pulse, ensuring a negligible relative phase between the fundamental, E_{ω}, and second harmonic, $E_{2\omega}$, pulses. The second criteria can be met by using all-reflective optics and requiring the beams to remain collinear so that any path length fluctuations are equally experienced by both beams. Additionally, the relative phase must be maintained uniformly across the beam cross-section, which requires all optics between frequency doubling crystal and the sample have a surface error below $\lambda/10$.

The samples consist of a multilayer epitaxial graphene film produced on the C-terminated face of single-crystal 4H-SiC by thermal desorption of Si. Four different samples with different thickness are used in this experiment: #8B2 (9 layers), #1104 (13 layers), #1133 (35 layers) and #7J8 (63 layers). Of the samples, #7J8 was the most homogeneous and repeatable and all data was taken on sample #7J8 unless otherwise specified. Details of the growth process and sample characterization can be found in ref [10]. Unlike exfoliate graphene, the layers in epitaxial graphene maintain a specific

rotation relative to one another. This rotation is believed to decouple the layers, so the electronic structure is similar to single-layer graphene. The bottom few layers are heavily doped and the doping density decreases to zero at the top of the stack. Prior mid-IR pump-probe experiments have measured the Fermi level of the bottom four layers at 365 meV, 220 meV, 140 meV, and 93 meV relative to the Dirac point.

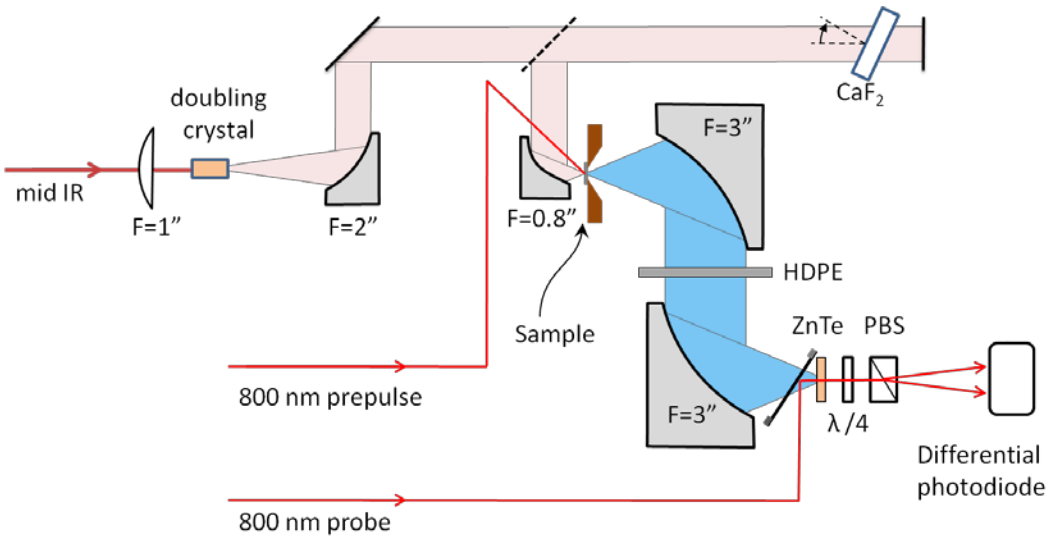

Figure 4.2 shows the experimental setup for generating and detecting coherent photocurrents

For our experiment, a commercial 250-kHz Ti:sapphire oscillator/amplifier operating at 800 nm is used to pump an optical parametric amplifier (OPA) followed by a differential frequency generator (DFG) to generate 200 fs pulses with an average power between 2–4 mW and centered at either 3.2 μm or 4.8 μm (ω beam). The horizontally polarized fundamental beam, (labeled mid-IR in Figure 4.2) is doubled in an $AgGeS_2$ or ZGP crystal to a vertically polarized 1.6 μm or 2.4 μm second harmonic beam with a 10% conversion efficiency. The two collinear beams are passed through a 1.5 mm CaF_2 plate. Tilting the plate allows adjustment of the relative phase through chromatic dispersion in the window. The beam is reflected back at a slight downward angle and makes a double pass through the same CaF_2 window. The accumulated phase through a double pass of the CaF_2 window at a tilt angle, θ_i, and thickness L, is derived in Appendix F and can be expressed as:

$$\Delta\Phi_{RT} = 2 * (2\Phi_1 - \phi_2)$$
$$= \left(\frac{4\omega L}{c}\right)\left(\sqrt{n_1^2 - 1 + \cos^2\theta_i} - \sqrt{n_2^2 - 1 + \cos^2\theta_i}\right) \quad (4.7)$$

where n_1 and n_2 are the phase indices of refraction at the fundamental and second harmonic frequency, respectively.

Asymmetric Fresnel reflection coefficients between the orthogonally polarized beams and mechanical vignetting by the window mount limit the maximum CaF_2 window tilt to 50°. The cross-polarized beams are overlapped on the sample with a 30 μm diameter (FWHM) spotsize, producing peak focus intensities for the 3.2 μm and 1.6 μm beams of 2.26 GW/cm^2 and 0.32 GW/cm^2, respectively, after losses from intermediate optics. Optionally, the graphene carrier density and temperature can be elevated with a 100 fs prepulse centered at 800 nm. This pulse arrives at a 46° incident angle which illuminates an elliptical 80 μm x 120 μm spot concentric with the mid-IR beams. The electron cooling rates and temperature were calibrated in collaboration with Dong Sun using mid-IR pump/probe data [89].

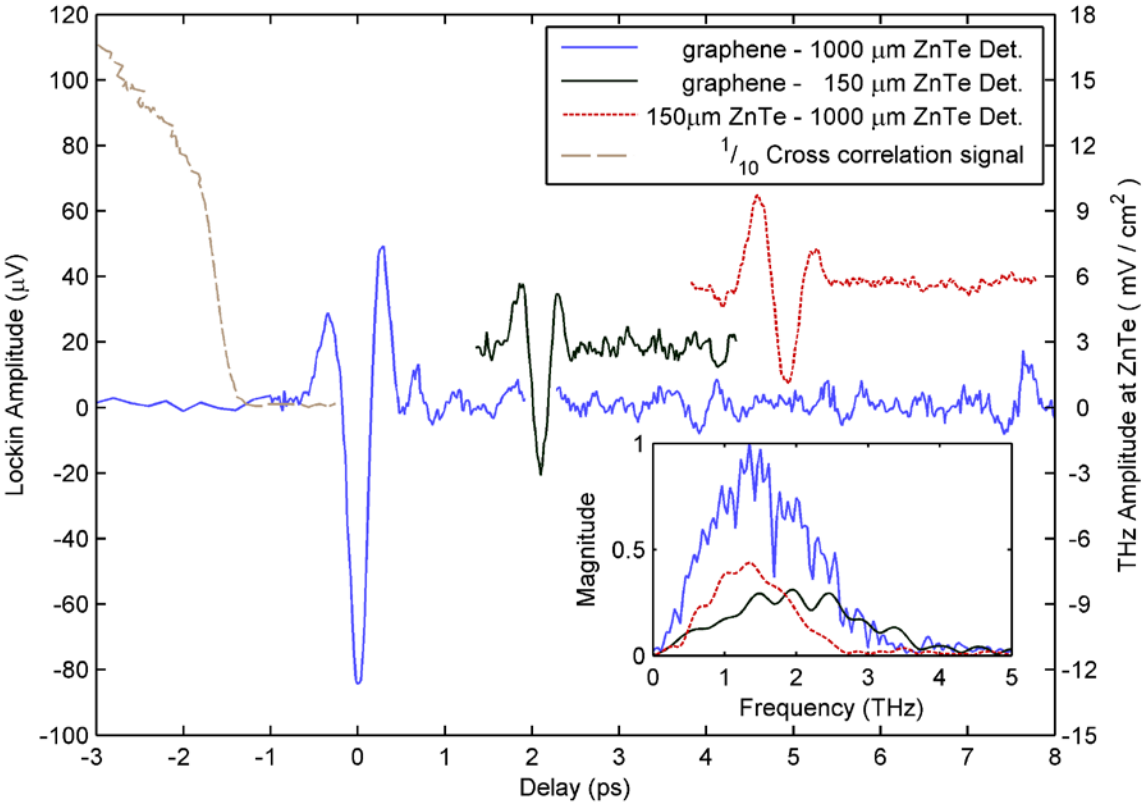

Figure 4.3 shows a comparison of the measured EO signals. The graphene signals are from the 63 layer sample (#7J8). The inset shows the spectrum of the measured signals.

Measurements of the photocurrent at room temperature are performed by measuring the emitted THz radiation. Generated THz passes through the SiC substrate and is reimaged onto a ZnTe crystal with a pair of 0.55 NA gold paraboloids. A 3 mm thick high density polyethylene (HDPE) slab was placed between the paraboloids to separate the collimated THz and any unabsorbed mid-IR by scattering the residual pump light. The focused THz is detected electrooptically as outlined on page 13. To increase the signal to noise ratio, the mid-IR beam was mechanically chopped at 1174 Hz and the THz waveform was slow scanned with a 300 ms lockin time constant. The chopping frequency was determined by scanning the frequency over the full mechanical chopper range (100 – 2000 Hz) and recording the effective SNR(f_{chop}). Two ZnTe crystals were available for detection; a thinner 150 μm and a thicker 1 mm crystal, which were able to measure up to 4 THz and 2 THz, respectively. As can be seen from Figure 4.3, the coherent control signal exceeds the bandwidth of the thicker ZnTe crystal; however the increase in SNR at lower frequencies justifies the loss of bandwidth. Unless otherwise

specified, the ZnTe crystal and optical sampling pulses are oriented to detect vertically polarized THz.

The conversion from lockin magnitude to absolute field is based on power measurements of the TeraSED using the liquid helium bolometer (Chapter 2), and the pinhole spot measurement technique outlined in Appendix B. The conversion factor is approximately 150 V/cm^2 per lockin volt for a 200 μW probe beam at 250 kHz. For small changes in the probe beam power (± 20%), the conversion factor is inversely proportional to the probe power. Probe powers outside this range require recalibration due to nonlinearity in the photodiode small-signal gain.

Interestingly, ZnTe appears well suited to optical rectification at mid-IR wavelengths. During the initial experiments, a large cross-correlation signal was detected between the unscattered pump beam at either 3.2 μm or 4.8 μm and the 800 nm sampling beam in the ZnTe detection crystal. This cross-correlation signal significantly aids spatial and temporal alignment of the detection system, as well as providing a detectable signal for optimizing the balanced detector. Due to dispersion in the SiC substrate, the signal arrives 1-2 ps before the THz and is shown at $1/_{10}$ scale in Figure 4.3. The signal has been temporally offset to correct for the path length change induced by the removal of the HDPE filter. For reference, the peak cross-correlation and coherent control signals are 30 dB and 70 dB smaller than the TeraSED waveform used in chapter 3.

The cross correlation signal is attributed to optical rectification inside the detection crystal. The signal showed a sinusoidal dependence on the polarization angle of the mid-IR and degenerate experiments at 800 nm show a similarly large coherent spike [133]. To test this theory, the graphene sample was replaced by the thinner 150 μm ZnTe crystal, and the radiated waveform is shown by the dashed curve in Figure 4.3. The 150 μm ZnTe crystal generated a comparable THz pulse with a peak field 40% smaller than the coherent control pulse from the 63-layer sample, despite 7,500 fold difference in thicknesses. Assuming a similar effective nonlinear coefficient, d_{eff}, and phase mismatch between pump pulses centered at 800 nm and 4.8 μm, the magnitude of the optical rectification signal is within an order of magnitude of the expected strength based on the

mid-IR intensity, which implies a ~10 mV/cm peak field in the detection plane. Although the absolute magnitude of the THz signal is weak by TD-THz standards, the relative strength of the coherent signal is remarkable.

Coherent Photocurrents

The radiated THz pulse as a function of the phase between the 3.2 μm and the 1.6 μm beams is shown in the large central panel of Figure 4.4. Vertical and horizontal traces show the THz amplitude at constant delay (t = 0 ps) and phase ($\Delta\Phi = 5.2\pi$), respectively. The time and phase axes have been corrected for temporal nonlinearity with respect to the CaF_2 tilt angle according to equation 4.7. For display purposes, the zero-tilt phase has been subtracted from the $\Delta\Phi$ axis ($\Delta\Phi_{\text{displayed}} = \Delta\Phi_\theta - \Delta\Phi_{0^o}$). For this data only, the 1.5 mm CaF_2 window was replaced with a thicker 5.0 mm window. The thicker window allows for a greater change in the relative phase, although it increases the temporal walkoff of the pulses and reduces the peak THz signal by 40%.

The obvious sign reversal of the THz field with a π change in the relative phase is a clear sign of a coherently controlled source. Furthermore, the agreement between the sinusoidal data in the top panel and the predicted oscillations based on equations 4.7 and 4.5 is astounding. The dispersion data for CaF_2 was taken from Corning [134] and interpolated where necessary. Otherwise, the only adjustment during fitting was an increase of the CaF_2 thickness from 5.000 mm to 5.090 mm, which is within the tolerances specified by the manufacturer. The slight reduction in signal at large phase differences is attributed to the increase in the CaF_2 Fresnel reflection loss at a 40° tilt angle. Temporally, the generated THz is nearly single cycle with slight oscillations after the main pulse. The shape of the THz pulse was highly variable from day to day, with the early experiments showing a unipolar signal as in Figure 4.3, while later experiments showed a more bipolar waveform as in Figure 4.4. Normally this would be attributed to misalignment of the focal distances in the imaging paraboloids. In a typical THz spectroscopy setup (Figure 3.4), the highly converging THz beam undergoes a phase shift as it passes through focus with different waveforms at focus and away. However, in order to meet the stringent requirements for efficient coherent control, all four parabolas

were aligned using a HeNe that was collinear with the mid-IR beam. The wavefront flatness and focal position in the sample and detection planes were verified by passing the HeNe through a 20 μm pinhole, where the depth of focus was less than ±50 μm. The longer wavelength of the THz ensures that the ZnTe detection crystal is well centered within the Rayleigh range of the THz beam ($2z_r = 1.5$ mm).

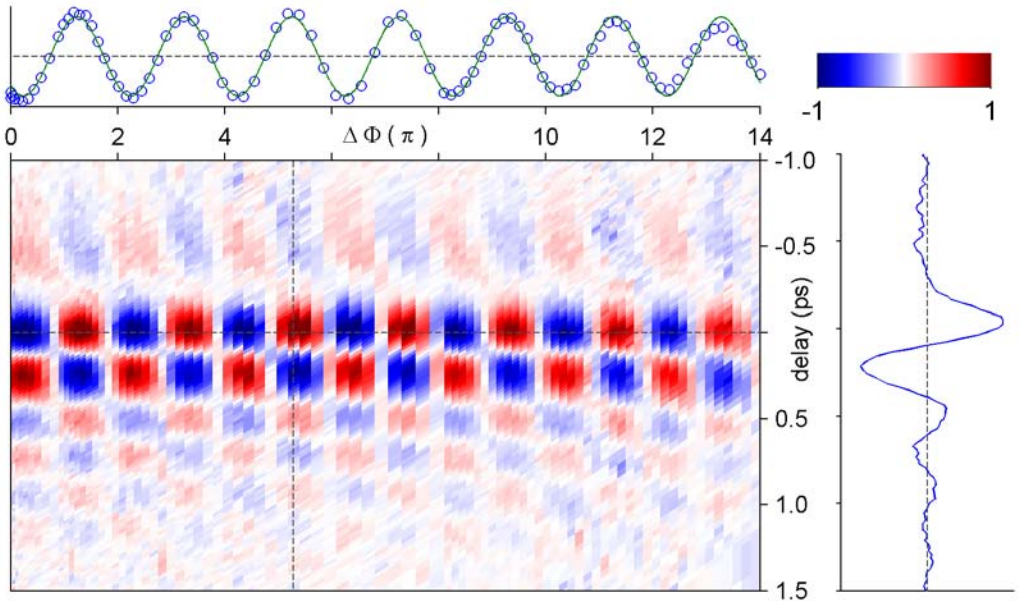

Figure 4.4 shows a phase-delay intensity plot of the coherently controlled THz signal at 3.2 μm - 1.6 μm pumping. The THz amplitude at constant delay and phase is shown in the top and right panels, respectively.

The variations in the waveform shape are more intriguing at 4.8μm / 2.4μm. Figure 4.5 shows a similar phase scan experiment, although at a much higher phase resolution. In the 3.2 μm scan, the time-domain shape of the pulse remains constant. This universal waveform is sinusoidally modulated as a function of Φ, with uniform peaks and zeros. However, at 4.8 μm there is no universal waveform. The phase scan shows periodicity and sign reversal, however the THz amplitude is a complex non-separable function of delay and phase. Furthermore, the peak THz magnitude shows a measureable reduction with increasing phase, unlike the nearly uniform modulation at 3.2 μm. There are several possible factors for this unusual behavior. First, the optical pulse at 4.8 μm may be strongly chirped. This would reduce the coherence length between the ω and 2ω pulses and lead to a nonuniform, time-dependent, phase difference for anything other than zero phase. Second, the optical pulses may be generating elliptically polarized THz. Recent

measurements of THz generation via high energy two-color filamentation in air also show similar phase-time behavior [135], which the authors attributed to elliptical generation. As will be shown later, the major axis of the THz polarization is at 30° to the detector axis. The projection of out-of-phase orthogonal components onto the linearly polarized detector could potentially explain the observed data. Third, the 'smeared' phase-time plot is characteristic of exciton effects in GaAs [136]. The zero effective mass of charge carriers prevents the formation of traditional excitons, however Coulomb interactions under coherent control conditions are not well studied and require further investigation.

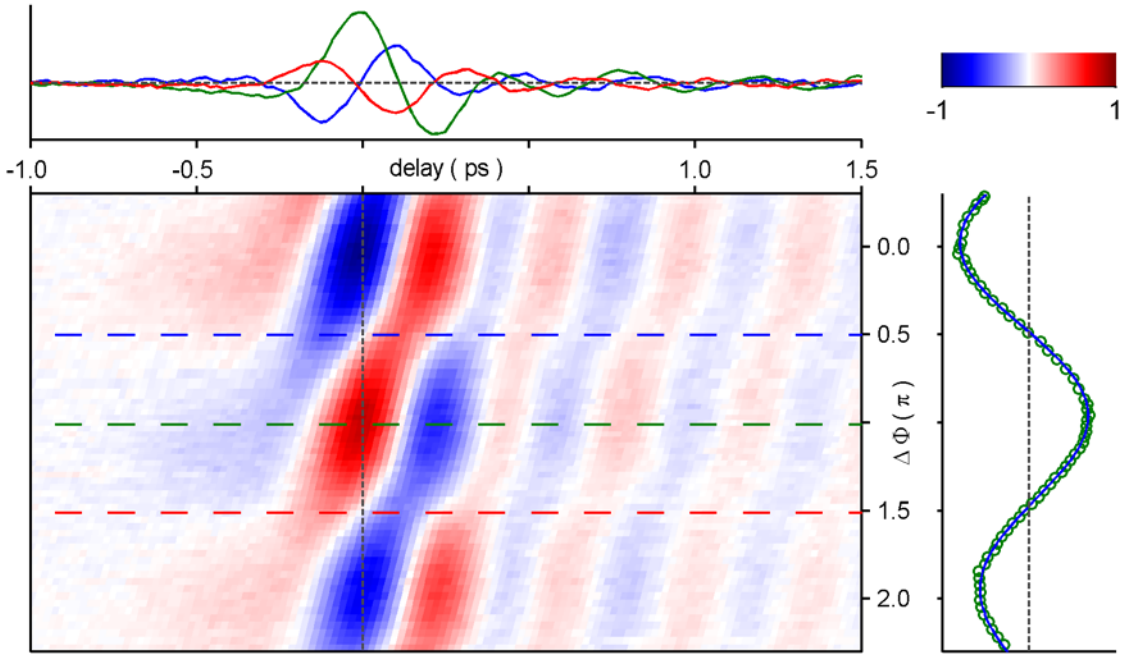

Figure 4.5 shows a high resolution phase scan at 4.8 μm with the 1.5 mm CaF_2 window. The phase and time axes are reversed from Figure 4.4. The three constant phase traces show the maximum and minimum THz-energy time-traces.

Polarization Dependence

Measurements of the photocurrent polarization dependence can provide a simple confirmation of the linear bandstructure. Unlike other semiconductors such as Si or GaAs, the photocurrent should be independent of the graphene crystal axis with strong generation for both co- and cross-polarized beams [124, 126]. For linearly polarized optical beams, the coherent current is linearly polarized with a sinusoid dependence on the relative angle between the ω and 2ω beams (eq. 4.5). For a horizontally polarized

fundamental beam and a vertically polarized second harmonic, one would expect a vertically polarized coherent current and THz pulse.

For strong THz signals, the simplest method for measuring the full polarization state of the THz pulse is to rotate the ZnTe detection crystal. For (110) ZnTe, the crystal is only sensitive to the component of the THz field perpendicular to the (001) axis, as described in equation **Error! Reference source not found.**. This, however, requires a erfectly isotropic crystal and commercially available ZnTe crystals tend to have a small but non-negligible birefringence. Early attempts to measure the coherent signal polarization using this method failed, due to the unusually large birefringence in our ZnTe detection crystals. Rotating our detection crystal unbalances the differential photodiode signal, complicating quantitative comparisons between the orthogonal components of the THz polarization.

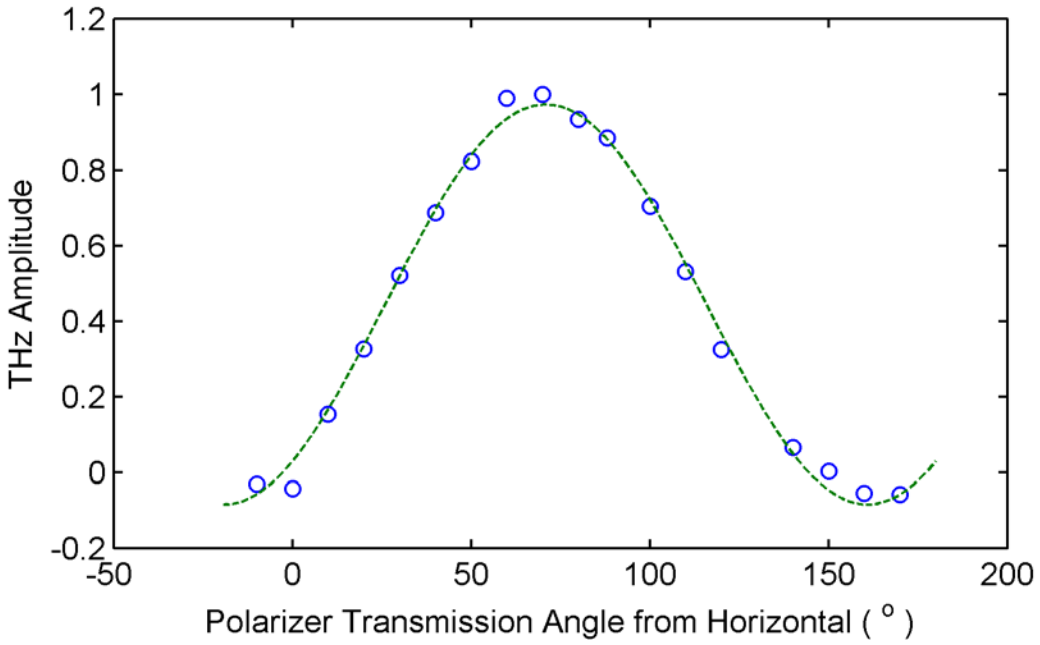

Figure 4.6 shows the magnitude of the transmitted THz through a polarizer. The best fit curve is for a linearly polarized THz pulse at 33° from the predicted vertical polarization.

To estimate the THz polarization state, we placed a wire-grid polarizer after the HDPE filter in the collimated THz beam between the paraboloid mirrors. A HeNe laser was diffracted off the wire grid, and the polarizer transmission angle was measured relative to the experimental horizontal plane. The polarizer was rotated and a waveform

trace was taken at each rotation. Using simple Jones calculus, one can calculate the transmission of an arbitrary linear polarization through a rotated polarizer and detected by a polarization-sensitive detector. Assuming the starting polarization is at an angle α relative to the horizontal, and the polarizer transmission-axis is at an angle θ, the detected polarization is proportional to:

$$E_{\text{detected}} = \cos(\theta)\sin(\theta)\cos(\alpha) + \sin^2(\theta)\sin(\alpha) \tag{4.8}$$

Figure 4.6 shows the peak THz signal as the polarizer is rotated. In order to increase the signal-to-noise, principle component analysis was used to compute the 'average' THz waveform, and the amplitude shown in the figure is the projection of each vector (waveform) onto the normalized PCA basis (average waveform). The numerical best fit using the above equation is shown by the green dashed curve in Figure 4.6. The best fit polarization is a linearly polarized THz beam at 57° from horizontal and a slight 2° misalignment to the ZnTe's vertical orientation.

There are several possible factors that can explain the rather large 33° difference between the predicted vertical polarization and the best fit model. First, the polarization of the fundamental beam from the DFG may not be horizontal. Later measurements of the DFG spot size (see Appendix F) confirmed a design flaw in DFG layout. The final collimating parabola was oriented backwards, which introduced significant coma and spherical aberration. In the original flawed configuration, the mid-IR beam was at a non-45° angle of incidence, which can cause polarization rotation when combined with other misalignments. Second, the fundamental beam may not be aligned to a birefringent axis within the frequency doubling crystal, which would lead to an elliptically polarized ω beam. The crystal was tweaked for maximum coherent control signal, not maximum conversion. In the experiment, the maximum coherent signal occurred at a small but measureable rotation from the optimal position for second harmonic conversion (~6°). Third, it is possible that the commercial ZnTe crystal was miscut. The vendor specified two axes, (110) and (001), to within 2°, but we are unequipped to verify this. Lastly, it is possible that the theory for the orientation of the graphene coherent current is incorrect.

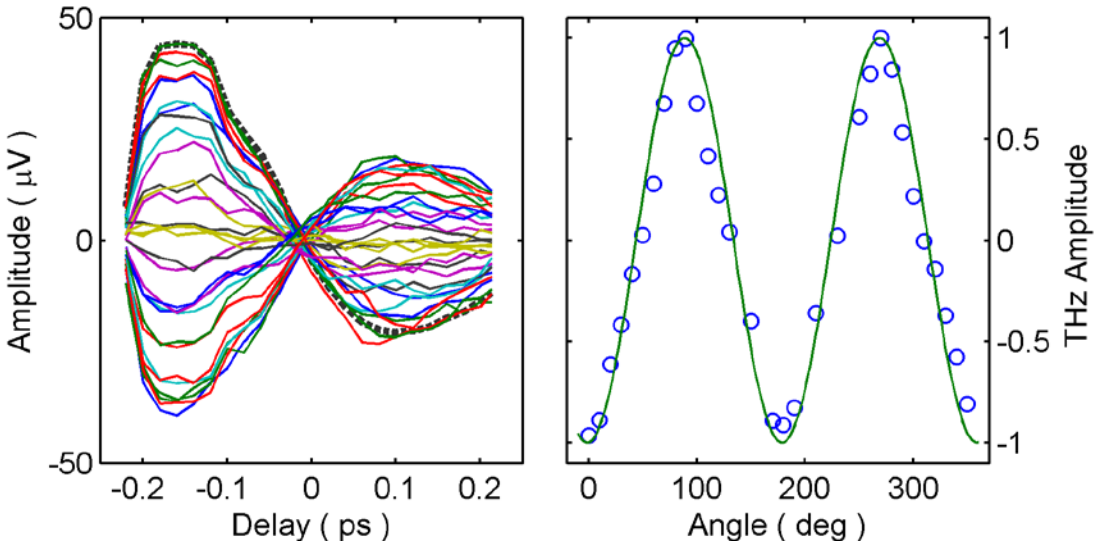

Figure 4.7 shows a rotation of the doubling crystal and a half waveplate.

An additional theoretical prediction is that the coherent current is independent of the graphene orientation. To test this theory, a half wave plate was placed before the doubling crystal and the two were rotated in a 1:2 ratio. At each rotation, a THz trace was taken and the raw data is shown in the left panel of Figure 4.7. The first principle component of the data set was computed and is indicated by a thick dashed line in the left panel. The normalized projection of each trace onto this component is shown in the right panel. As expected the THz trace varies sinusoidally with the waveplate rotation, which is exclusively due to the linear polarization sensitivity of the electrooptic detection system. The excellent agreement suggests that graphene is isotropic and the coherent current is independent of the ***sample*** axes. Unfortunately, the unique rotational stacking in epitaxial graphene creates a broad distribution of crystal axes in thick multilayer samples. It's likely that any crystal orientation dependence averages out for the 63 layer sample in Figure 4.7.

Power Scaling

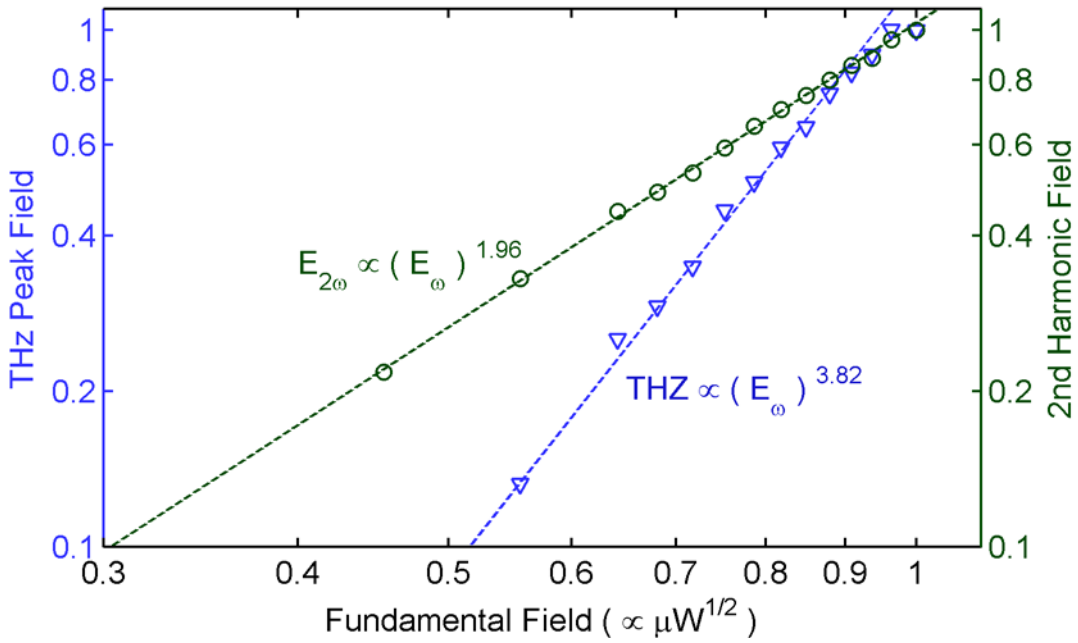

Figure 4.8 shows the dependence of the peak THz signal (triangles, left axis) and second harmonic power (circles, right axis) on the fundamental 3.2 μm power.

The coherent current magnitude is expected to vary linearly with the second harmonic field and quadratically with the fundamental field as described in equation 4.5. To verify the theoretical power relationship, ideally one would attenuate the ω and 2ω beams separately and establish the interdependent power relationship accordingly. However, the lack of neutral density filters at mid-IR wavelengths and the collinear experimental geometry prevents independent adjustment of the ω and 2ω power. The experiment is further complicated by the lack of commercial attenuators with λ/10 surface flatness. Although relative changes in the coherent signal amplitude are unaffected by wavefront error, the initial reduction following insertion of the attenuator will further reduce the poor SNR.

To address these limitations, a variable attenuator was used to reduce the pump power to the OPA, which in turn reduced the fundamental power from the DFG and the second harmonic from the doubling crystal. At each reduction, the fundamental power, second harmonic power, and peak THz signal were measured and the data is plotted in Figure 4.8. As expected, the peak THz amplitude dependence is very close to the theoretical $E_{THz} \propto J_{CC} \propto (E_{\omega})^{4.0}$.

Hot Carriers

To study the effect of background carriers, an 800 nm prepulse was used to inject hot carriers before the ω/2ω pulses, as shown in Figure 4.2 The prepulse delay and power are continuously tunable with a delay resolution of 70 fs and a maximum power of 26 mW. The hot carrier temperature and density are measured by removing the HDPE filter and sending the residual mid-IR light into a monochromator and using the prepulse in an 800 nm pump / mid-IR probe configuration. The mid-IR differential transmission was then calibrated against previous measurements [104].

Similar to the methodology in Chapter 3, two acquisition methods were used to measure changes in radiated THz field. First, either the direct or the differential THz waveform can be measured. For large changes, the direct THz waveform can be measured; however for small changes, measuring the differential change, by moving the mechanical chopper to the prepulse beam, yields a better SNR. This method is useful when the shape of the radiated THz wave needs to be monitored. The other acquisition method is to fix the sampling beam delay at the peak of the THz wave and measure the instantaneous change in the peak field. Since we don't need to scan out the THz waveform, the total acquisition time with this method is much shorter, making the data less susceptible to long term noise such as laser drift.

Figure 4.9 shows the radiated THz waveform at several prepulse power levels and delays. In this experiment, the prepulse delay is set manually, and the THz waveform is quickly scanned at maximum prepulse power. A variable attenuator is then used to attenuate the power to 15 levels, of which a subset is shown in Figure 4.9. After the 15 scans, the process is repeated at a new delay. This data illustrates some of the challenges facing longer acquisitions. Over a 2-hour experiment, we measured the unperturbed coherent signal four times ('no pump' @ delay = 0, ½, 1, or 2 ps). Ideally this waveform should be identical in all four plots, however, later measurements show a clearly increasing ringing after the main pulse. The evolution of the pulse shape and the appearance of ringing could easily be misidentified as an onset of space-charge effects if they happened to coincide with a reasonable source.

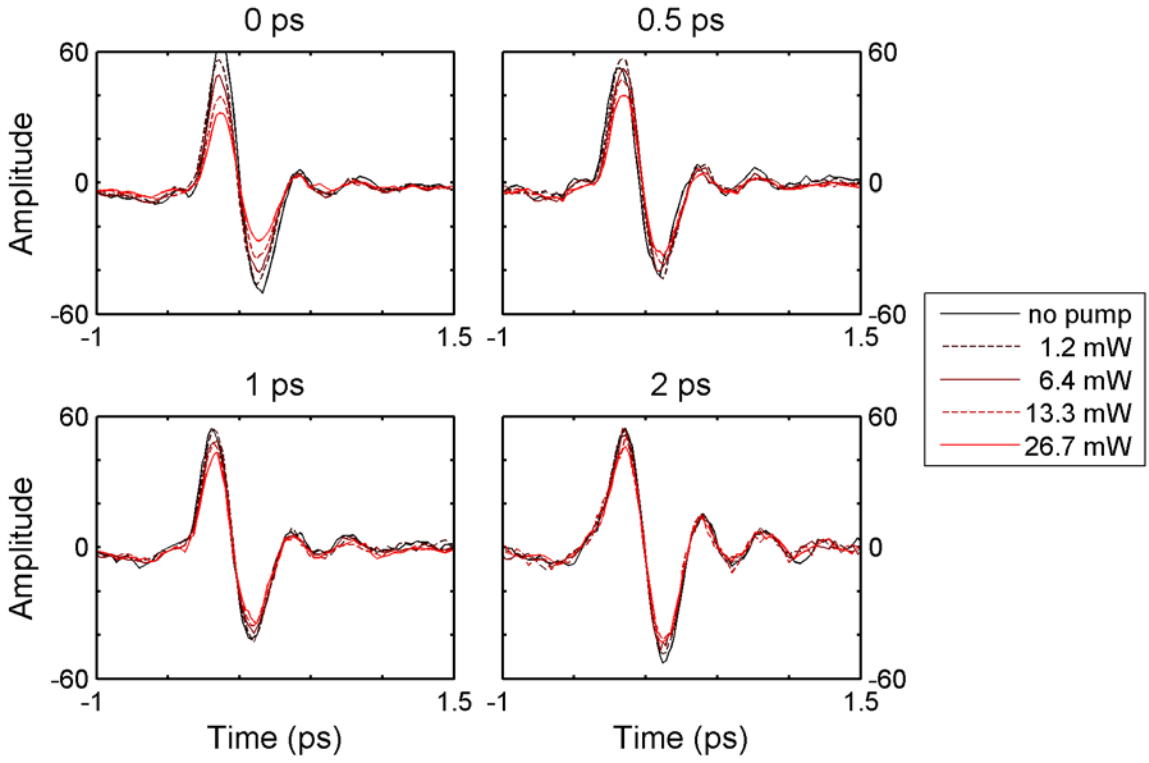

Figure 4.9. shows the effect of an optical prepulse on the THz waverform. Each subplot shows the radiated waveform for a fixed prepulse delay and select power levels. The prepulse delay is inverted with respect to the sampling pulse time axis, i.e. the '1 ps' 800 nm pulse arrives at t = -1 ps.

One might hypothesize that the increased conductivity associated with additional hot carriers would enhance any space charge effects if present. This would change the temporal behavior of the coherent photocurrent by increasing the decay rate, potentially leading to an underdamped response and current oscillations. However as Figure 4.9 shows, the THz signal decreases with increasing delay or increasing power but maintains a similar shape. The strong reduction, but similar pulse shape, suggests that any space-charge effects are minor as compared to other processes that affect the magnitude only, such as dephasing, Pauli blocking, or reabsorption of the generated THz by hot-carrier-increased conductivity.

To estimate the contributions from the different attenuation mechanisms, we monitored changes in the peak THz signal at two locations on sample #7J8 as a function of the prepulse delay as shown in Figure 4.10. The first position was taken at the same location as the data from Figure 4.9, while position 2 shows the maximum modulation depth we observed due to sample inhomogeneity. The data was fit with a biexponential

recovery that was lowpass filtered to account for the limited bandwidth of the ZnTe detection system. For comparison, the room temperature optically induced differential THz transmission from Chapter 3, is plotted by a slower green curve. In the green curve, the THz echo at 6.8 ps has been numerically removed for clarity.

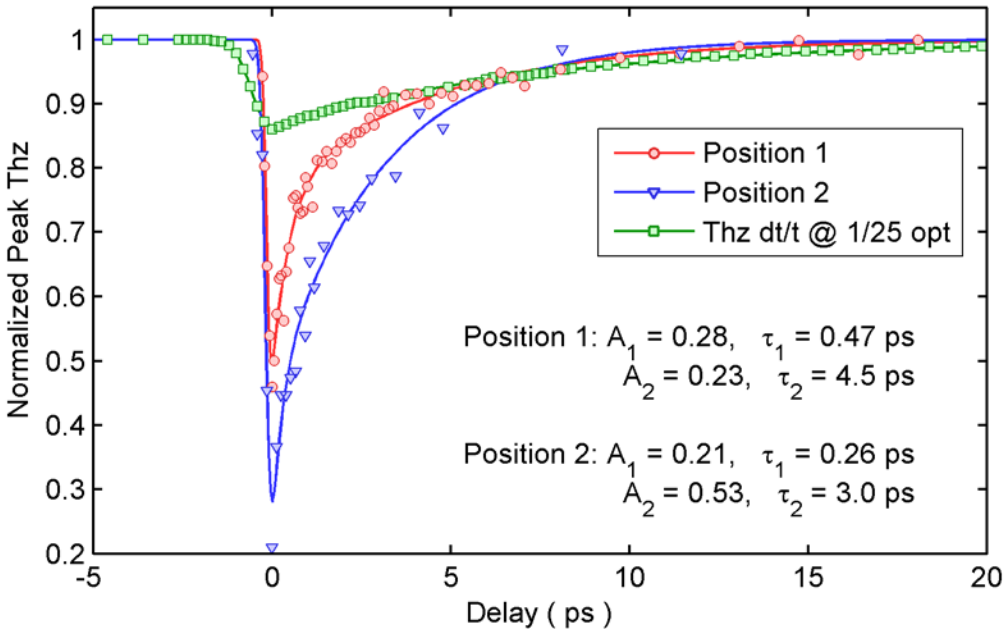

Figure 4.10 shows the effect of an 800nm optical pre-pulse on the peak THz signal.

The biexponential fit parameters at each position show a comparable contribution from a fast < 0.5 ps recovery (EO detection limited) and a longer 3-5 ps recovery. The magnitude and recovery time for the slower decay matches very well with THz reabsorption dynamics, assuming one extrapolates the lower fluence pumping from Chapter 3 to the tighter focusing geometry used here. Neglecting the obvious saturation trend, and extrapolating the THz-reabsorption intensity-dependence out 25x, the maximum reduction due to reabsorption is 20%. The contribution from Pauli blocking can be estimated using standard mid-IR pump / probe techniques outlined elsewhere [104]. In-situ measurements performed by Dong Sun characterized a 12% reduction attributable to Pauli blocking of the final state by hot carriers [104]. Since the total reduction attributable to space charge (<1%), THz reabsorption (20%) and Pauli blocking (12%) is much less than the observed attenuation (75%), dephasing of the coherent generation process must be the dominant mechanism. Identification of the decoherence process requires further study, but the mechanism must replicate several empirical traits.

Figure 4.10 shows that the decoherence process is fast, occurring on timescales shorter than 300 fs, and is more pronounced at elevated electron temperatures.

Sample Dependence

The dependence of the coherent photocurrent on an individual graphene layer's Fermi level and doping is theoretically unexplored. The theoretical background established at the beginning of this chapter assumes a perfectly undoped layer with the Fermi level at the Dirac point. To address this, we repeated the measurements on several samples with different layer thicknesses: #8B2 (9 layers), #1104 (13 layers), #1133 (35 layers) and different wavelength combinations, 2.4μm / 4.8 μm. Since the original 1.6 μm / 3.2 μm pump transition is right above the Fermi level of the most heavily doped layer, we expect the scattering of any injected electron to be significantly suppressed.

A simple model for estimating layer dependence begins with the assumption that the radiated THz field is the sum of *N* independent layers. As the number of layers increases, any generation in the top layers will have to pass through additional layers before transmitting through the substrate. Similarly, the optical pump beams will suffer attenuation in the top layers, reducing THz generation in the bottom layers. If the layers are numbered 1 to *N*, beginning with the highly doped bottom layer, the generation at layer *k*, can be expressed as $E_k = \eta_k\,(\text{THz loss})(\text{optical loss})$. Assuming both the optical beams and the THz field suffer the same universal absorption [99, 137], the total forward and backward propagating fields can be expressed as:

$$E_{THz,\ forward} = \sum_{k=1}^{N} \eta_k \underbrace{(x)^{k-1}}_{\text{THz loss}} \underbrace{(x)^{3(N-k)}}_{\text{Optical Loss}} = \sum_{k=1}^{N} \eta_k x^{3N-2k-1} \tag{4.9}$$

$$E_{THz,\ backward} = \sum_{k=1}^{N} \eta_k \underbrace{(x)^{N-k}}_{\text{THz loss}} \underbrace{(x)^{3(N-k)}}_{\text{Optical Loss}} = \sum_{k=1}^{N} \eta_k x^{4N-4k} \tag{4.10}$$

$$x = (1 - 2.3\%)^{\frac{1}{2}}$$

Here, *x* is the wavelength independent amplitude transmission and η_k is the generation efficiency of layer *k*, relative to an undoped layer. If we assume the highly doped bottom layers are more efficient due to the lack of 'bad' electrons or suppressed scattering,

$\eta_1 > 1$. Conversely, if the scattering or dephasing is stronger in the bottom layers, $\eta_1 < 1$.

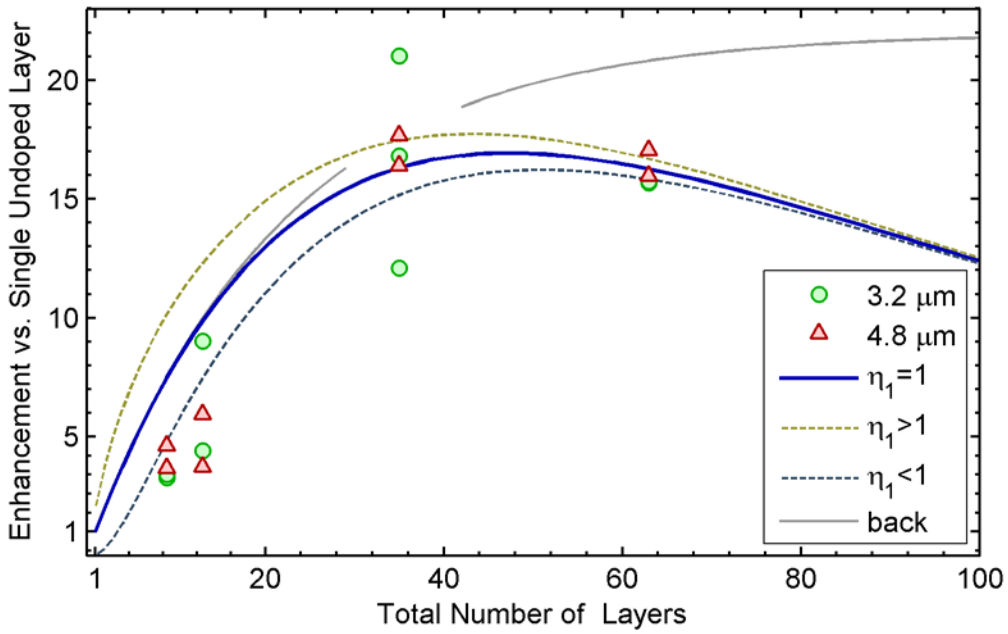

Figure 4.11 Signal scaling with graphene stack thickness. The peak THz field measured at several positions on each sample is shown by the filled markers. The enhancement of the forward propagating THz is shown by the dark blue and dashed lines. For comparison the enhancement curve for the backward propagating THz signal shown in light gray.

Figure 4.11 shows the measured THz amplitude at multiple positions on different samples. The absolute magnitude of the data was scaled to match with the model at 63 layers. For the model, either a uniform layer response was used, $\eta_1 = 1$, or an exponential decay was used $\eta = 1 \pm \exp\left(-\frac{k-1}{N_{screen}}\right)$, where N_{screen} is the measured Fermi level screening length [89]. Strangely, although the model follows the general trend of the data, the thin graphene samples suggest decreased generation in the bottom layers. We expected that the reduction of bad carriers in the doped layer would result in a significant enhancement of the coherent signal from the bottom layers. Unfortunately, the large spatial variability of the samples and the similarity between the 3.2 μm and 4.8 μm pumping makes a determination of the layer scaling difficult. One interesting note is the potential for increased signal in reflection geometry. Typically, one avoids measuring the backward propagating THz since the setup is more complicated to build,

difficult to align, and yields weaker signals [138]. However, in thick graphene stacks, the potential for increased signal may outweigh the difficulties in experimental design.

Conclusion

In conclusion, we have generated coherently controlled electrical currents in epitaxial graphene using mid-IR pulses. A theoretical description based on the tight binding model in an undoped layer was presented and the dependence of the coherent current on experimental parameters was measured. We were able to measure 14 oscillations of the coherent current verifying the $\Delta\Phi$ dependence. Measurements of the power dependence and polarization state generally agree with the theoretical model, although the small discrepancy in between the measured and predicted polarization state merits further study. We also used an ultrafast prepulse to demonstrate the increased dephasing associated with hot carriers. Lastly, a simple model for the layer dependence was presented in rough agreement with the data, although the model indicated decreased generation in the highly doped layer in contrast to expectations. These results are encouraging for all-optical generation of electrical currents in epitaxial graphene and may bring new understanding to optoelectronic functionalities in graphene.

Chapter 5
Conclusion

The work in this thesis began with two apparently independent aims. The first goal was to increase the signal-to-noise of a typical time domain THz system by drastically increasing the source power. Concurrently we were also trying to measure the THz dynamics of a truly novel material, epitaxial graphene. However, progress on the second aim was severely limited due to the weak interaction of a single atomic layer and the large pulse-to-pulse variations in a typical TD-THz system (both are ~2%). Early on, I hoped to merge these aims and a third aim, the optical generation of ballistic THz current pulses, into a combined method for measuring the THz dynamics of carriers in epitaxial graphene.

In Chapter 2, I described the development of a high power TD-THz system. The goal of this system was to drastically increase the source power, allowing us to use established noise reduction techniques, such as lockin amplifiers, to more accurately measure the transmission of the sample under study. To this end, I achieved an order of magnitude improvement in the average power of a THz pulse train vs. a conventional photoconductive / Ti:sapphire system. The designed system combines a low-loss phase-matched crystal with high power fiber laser to produce a high repetition rate, high average power TD-THz source. In order to improve the spatial overlap and interaction length between the diverging THz and the optical pump, a novel air clad waveguide geometry is proposed where the high permittivity of the GaP crystal is used to confine generated THz while allowing pseudo-free-space propagation of the optical pump beam. Confinement of the THz modifies the propagation by introducing several forms of dispersion: modal, waveguide, and polarization. A theoretical model for the THz generation is presented by combining the 1D generation equation with a numerical FDFD simulator which calculates the modes and propagation constants for the GaP waveguide. The theoretical model is confirmed by measuring the power generated in two 6 mm long

GaP waveguide with rectangular cross sections using a high average power fiber laser, and the generated waveforms and their spectra are shown to be in good agreement with the model.

An alternative to boosting the source power, one can simply generate the THz transients in situ and measure resulting radiated THz pulse. As the coherent-control / optical-prepulse experiment showed, it's possible to measure the scattering and dephasing effects without an incident THz pulse. In the coherent control scheme, photoexcited carriers are given a net average momentum in a controlled direction, giving rise to a macroscopic current. The ultrafast coherent current radiates a THz pulse. In chapter 4, I described the initial results from coherent generation of photocurrents in epitaxial graphene. The power scaling and polarization dependence on the fundamental and second harmonic beams were shown to be in agreement with theoretical predictions. Additionally, the coherent photocurrents are shown to be dependent on the temporal and spatial shape of the optical pump pulse. This creates the possibility of generating THz current pulses with spot sizes and bandwidth far beyond conventional free space photoconductive emitters.

Originally, we intended to use the two THz generation systems to answer two open questions about epitaxial graphene. First, does the linear dispersion of isolated graphene extend to the Dirac point in epitaxial samples, or is there a small bandgap opening? Previous experiments established a 10 meV upper limit for the bandgap size. Using a conventional THz spectroscopy system, we were able to reduce this limit by an order of magnitude, establishing a new 0.7 meV upper limit for the bandgap size. The second open question focused on the behavior of hot carriers in epitaxial graphene. From a device perspective, the operation and efficiency of many devices is critically dependent on parameters such as the recombination and cooling lifetimes. Measurements of the temperature-dependent recovery dynamics show that carriers in a room temperature lattice recover at rates consistent with Auger recombination. However at colder temperatures, following a partial recombination consistent with Auger recombination, the recovery slows significantly and we observe rates more consistent with a single population of carriers cooling via phonon emission. Measurements of the carrier cooling

dynamics and the nonlinearity threshold are encouraging for the further development of optoelectronic functionalities in graphene.

High Power Generation Summary

During the work for this thesis, the area of high power time domain THz saw a dramatic increase in both the generation efficiency and total power. This was achieved by either scaling to low pump repetition rates and high pulse energies, or maintaining the repetition rate but scaling to high average power either directly or through a resonant cavity. As a starting point, we measured the power generation from common generation schemes directly with the liquid helium bolometer.

- 1.2 μW at 76 MHz from a narrow gap photoconductive emitter at 10 V p-p bias.
- 5.2 μW at 250 kHz from a large area interdigitated photoconductive emitter at 10 V p-p bias.
- 1.4 μW at 250 kHz from a 1 mm ZnTe crystal.

Occasionally, much higher numbers have been reported in the literature. These methods use multistep indirect methods and are inherently less reliable. At the beginning of this work, the major achievements in time domain THz generation were:

- 40 μW at 72 MHz from a large gap photoconductive emitter (2mm gap, 800 V p-p bias). The power was indirectly inferred from the photodiode signal strength observed in a standard EO detection scheme [139].

Concurrent with our work, the following advancements were made in 2006 and 2007.

- 240 μW using the pulse-front-tilt method inside LiNbO3 using a 1 kHz Ti:sapphire regen [26].
- 1000 μW generation inside doubly resonant OPO using quasi-phasematched GaAs [140]. With a phase stabilized cavity, the circulating pump power was ~120 W at 50 MHz. The QPM-GaAs source produced narrowband (100 GHz) THz packets that were measured interferometrically.

Compared with the prior art and the above developments, the GaP waveguide source has several significant accomplishments

- 150 μW at 80 MHz generation inside the larger 1000 × 700 μm waveguide using a simple collinear geometry and a 10 W pump.
- The ability to tune the THz spectrum by controlling the waveguide dimensions.
- Simple theoretical model based on a standard FDFD mode solver and the 1D generation equation.

Graphene THz Spectroscopy Summary

Due to the recent isolation of single layer graphene and the establishment of alternative growth techniques, very little material characterization of epitaxial graphene was published prior to the beginning of my work. Unfortunately, two papers on the room temperature graphene THz transmission and recovery dynamics were published prior to the completion of the work in Chapter 3 [86, 98], limiting the potential impact. However the work in this thesis makes several significant contributions to the field of epitaxial graphene.

- The upper limit for a potential bandgap opening in our epitaxial graphene samples was reduced from 10 meV to below 1 meV
- The room temperature recovery of hot carriers is well modeled by a single exponential with lifetime consistent with Auger recombination (4 ps – 30 ps)
- Below 200K a second recovery process is observed with lifetimes between 50 and 500 ps, which is consistent with a single carrier distribution cooling via acoustic phonon emission.

Coherent Photocurrents Summary

Although optical coherent control is a mature and well established field, the demonstration of coherent photocurrents in epitaxial graphene offers several potential insights and contributions to the field. Prior to our work, the most relevant work was performed by van Driel's group on the thin graphite films and carbon nanotubes [77]. Our major contributions are:

- Verification of the theoretical polarization and power scaling relationships.
- Measurement of the effect of a background carrier density

Appendix A
Calibration of the Rapid Delay Stage

The Clark MXR ODL-150 rapid delay line is capable of scanning a large 150 ps window at a fast 10Hz rate, while still maintaining a high degree of linearity. As an indicator of the delay, the control electronics generate an analog voltage with an approximated 20 ps / V conversion factor. However since nonlinearities exist in both the stage control electronics and the digitizing electronics on the computer, it is important to know the magnitude of these nonlinearities.

To measure the true delay stage position, a Michelson interferometer was built using a simple HeNe laser. The interferometer transmission was measured using an amplified photodiode and the computer's National Instruments data acquisition board in parallel with 50Ω terminator. Simultaneously, the ODL-150 position voltage was measured by the computer with megaohm input impedance. The ODL-150 was scanned at 0.2 Hz over the full 160 ps window. This caused the interferometer fringes to oscillate at a maximum 41 kHz, well below the computer's 500 kHz sample rate. The scan was repeated 10 times and each fringe reading was converted to a delay using a simple mean-crossing algorithm, resulting in a stair-step pattern with a 2 fs step size. The ODL-150 proved to be very linear with any deviations below ± 60 fs. The uncorrected error from perfect linearity as a function of the delay voltage is shown in the upper panel of Figure A.1 and Figure A.2 As indicated, the repeatability between each scan is a few time the resolution of the system. To ensure the uncorrected error is below ± 20 fs, the CM809 and CM1106 stages require fourth and fifth order correction terms, respectively.

$$\text{Delay (ps)} = \sum_{k=1}^{N} a_k * (\text{ Voltage in volts})^k \tag{A.1}$$

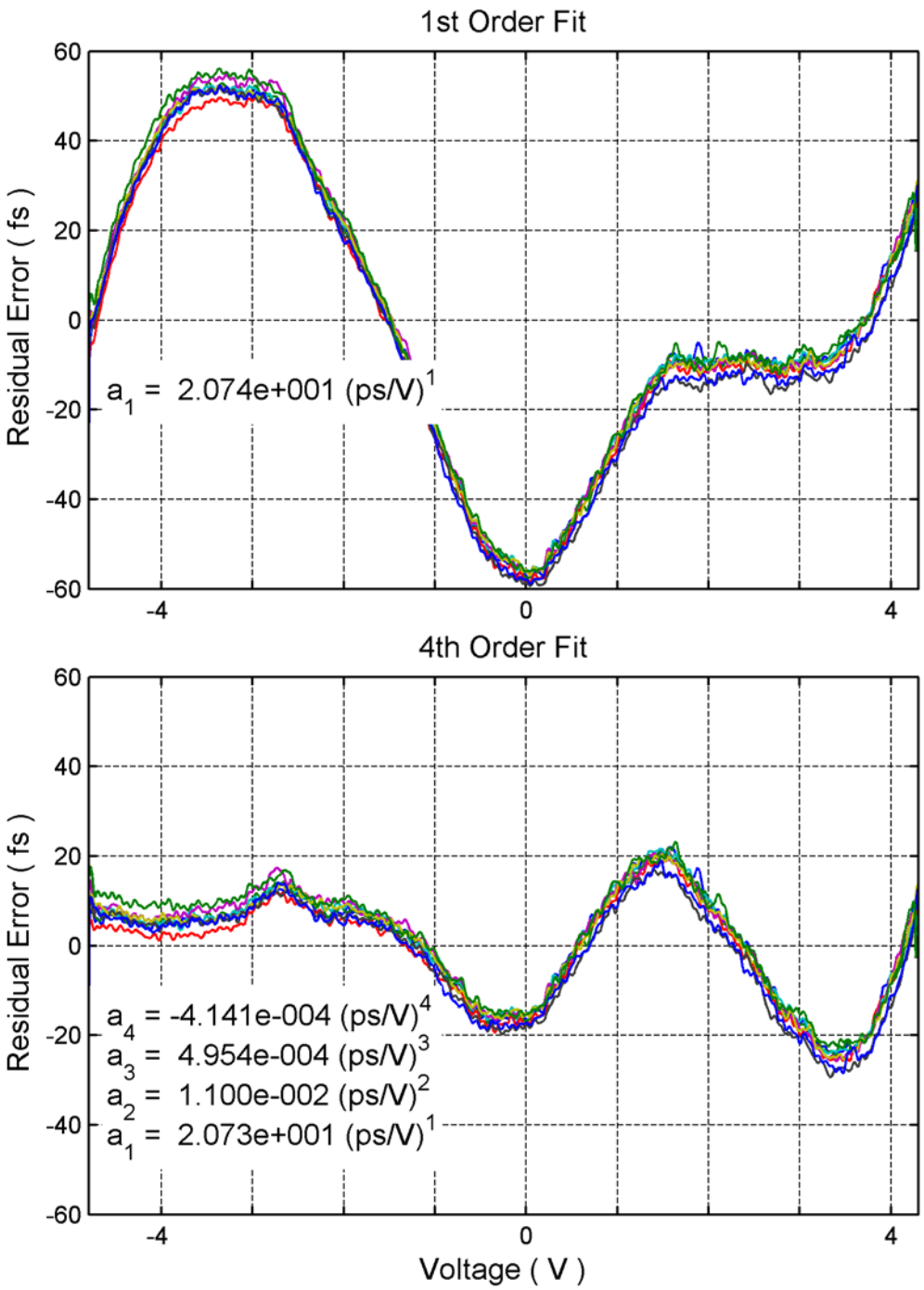

Figure A.1 shows the uncorrected delay error for stage **CM 809**. The error includes the limited precision (at 4 significant digits) in the lower left of each panel. Each line indicates a separate measurement, separated by 10 seconds.

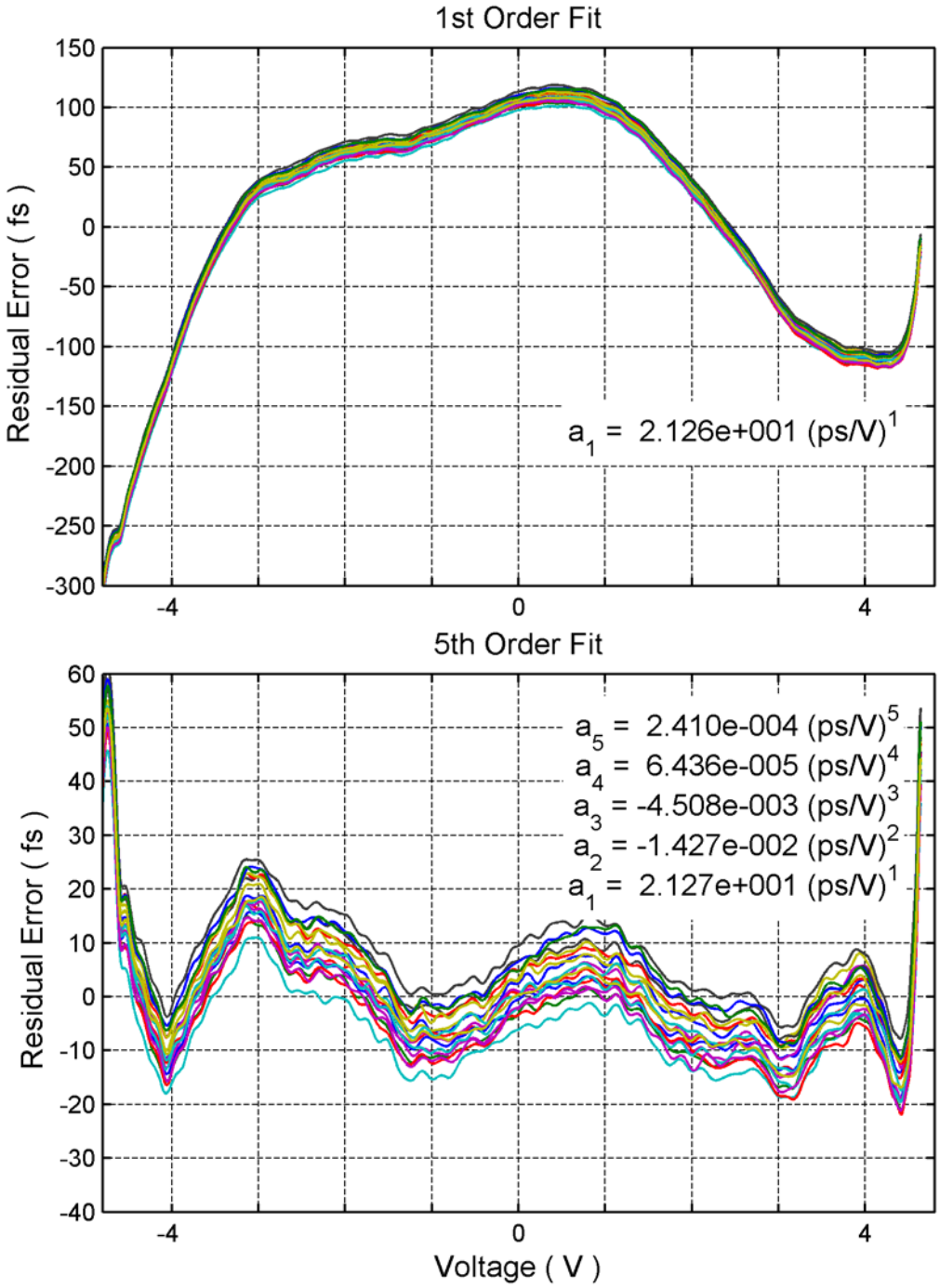

Figure A.2 shows the uncorrected delay error for stage **CM 1168**. There error includes the limited precision (at 4 significant digits) in the upper right of each panel. Each line indicates a separate measurement, separated by 10 seconds.

Appendix B
Measurements of THz Probe Spotsize

As with any pump-probe setup, it is important to measure the pump and probe spots and ensure their overlap on the sample. In a conventional setup with all optical beams, this is typically done with a camera if one is available at the relevant wavelengths. Alternatively, one can use a knife edge to measure the 10% and 90% power transmission in the sample plane.

Figure B.1 shows the results from a method similar to the traditional knife edge. A pinhole was placed in the sample plane and scanned across the optical and probe beams. At each point, the transmitted optical power and THz waveform was recorded. The raw un-deconvolved transmission for the optical and RMS THz through a small 200 μm (Figure B.1) and a large 950 μm pinhole (Figure B.2) is shown in the top center and right panels. The left panel shows an image taken with a small lenless CCD array. The obvious structure in the optical beam comes from diamond turning grooves in the gold paraboloid.

Attempts at numerical deconvolution via FFT produced unreliable results, so the raw data is shown instead. The right of each subfigure, the full width half maximum (FWHM) and the full beam waist ($2\omega_0$) are shown. Since these are measurements of the *convolved* data, they represent an upper bound on the true spot size. The time domain THz data was then Fourier transformed and beam cross section at different frequencies was plotted in the lower 9 panels.

The smaller pinhole is subwavelength at frequencies below 0.5 THz. One interesting manifestation of this is shown in the 0.4 THz image. At particular frequencies, it's possible for a subwavelength aperture to convert a linearly polarized beam into a radially polarized beam, although with very poor efficiency. The mode shown in the 0.4 THz

panel is the product of a radially polarized beam and a linearly polarized detector, i.e. the '01' mode.

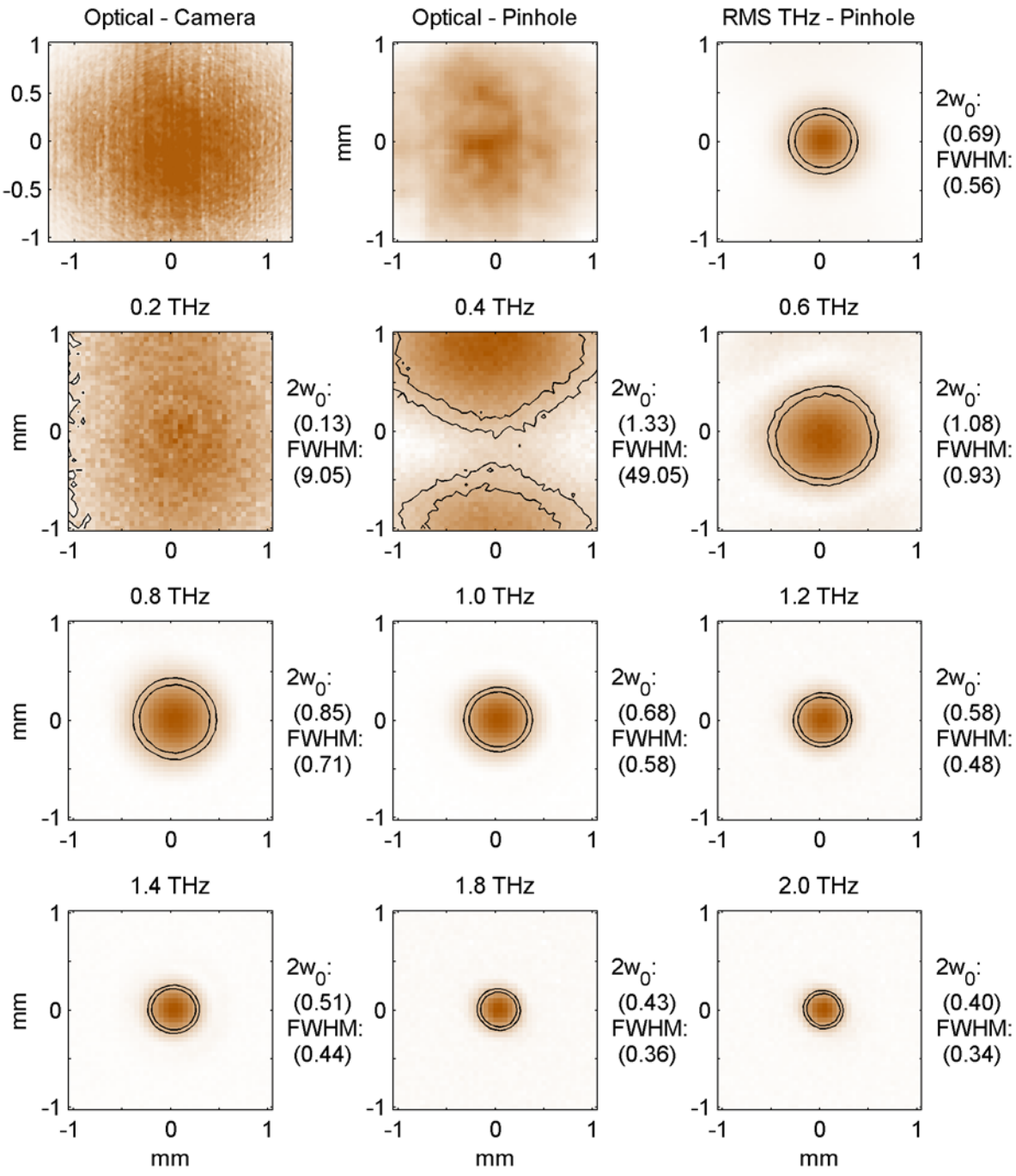

Figure B.1 shows the convolution of the detectable THz spot in the sample plane with the smaller 200 μm pinhole. Below 0.6 THz, the 200 μm pinhole is subwavelength, which creates a radially polarized far field diffraction pattern.

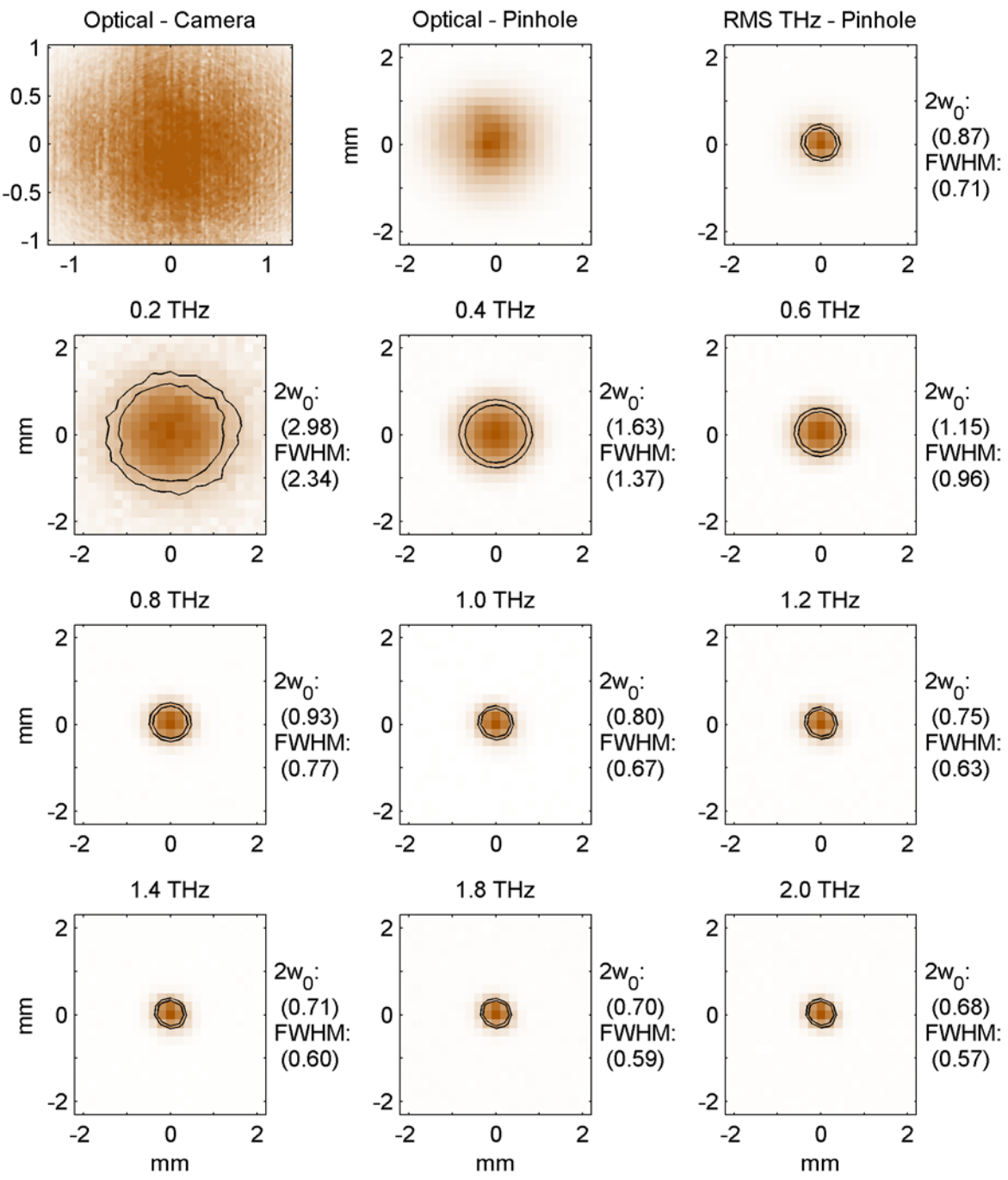

Figure B.2 shows the convolution of the detectable THz spot in the sample plane with the large 950 µm pinhole.

Appendix C
TeraSED Divergence Angle

The TeraSED divergence angle was measured using a THz imaging setup courtesy of Malakeh Musheinish. The detection side of this system consists of a pair of parabolic mirrors which images a free space point onto a ZnTe crystal for standard electrooptic detection. One parabolic mirror is on a translation stage that is aligned with the collimated beam between the paraboloids. This allows the image point of her paraboloids to be horizontally scanned across an object. The TeraSED was placed on a second translation stage perpendicular to the paraboloid scan axis. By scanning both stages, the diverging THz wavefront was mapped out. The figure below shows the peak-to-peak THz as a function of propagation and lateral distance. Each cell in the intensity plot underneath the divergence curves is the RMS THz amplitude at that point. The RMS TeraSED beam waist diverges at a ±12° angle.

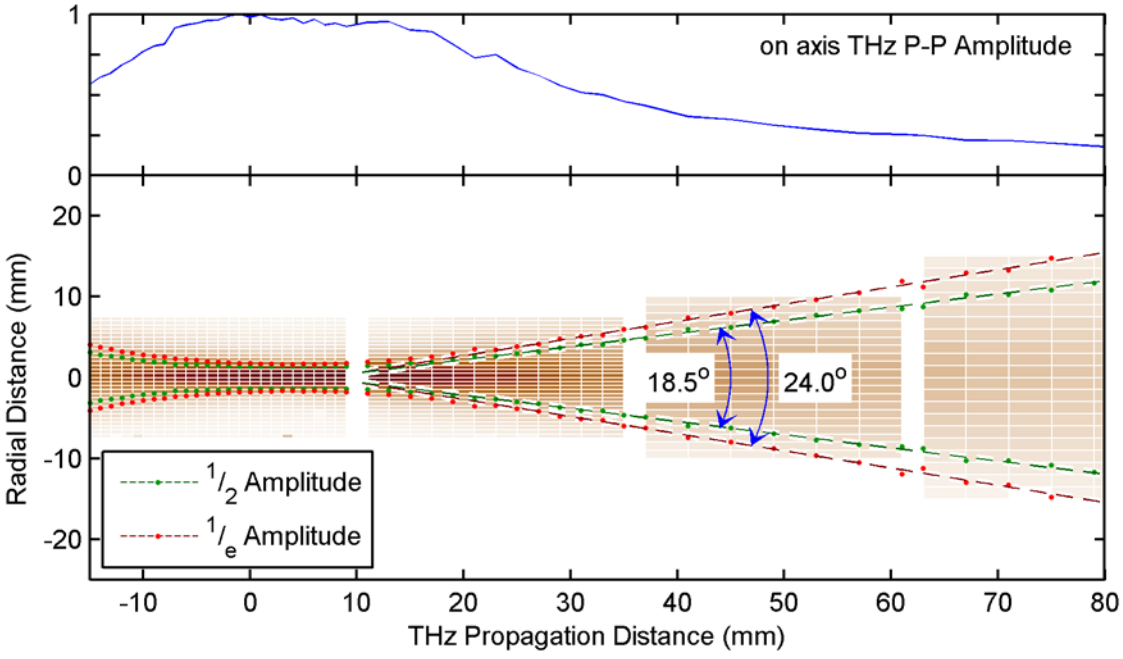

Figure C.1 shows the TeraSED divergence.

Appendix D
Noise Floor in THz differential Transmission Setup

Similar with nearly all lockin based experiments, the choice of chopping frequency can dramatically affect the noise floor of the system. When new students are introduced to phase sensitive detection techniques, they are generally advised to chop at the highest possible frequency. While this is true for ideal 1/f noise, it may not be appropriate for the real noise spectrum encountered in situ.

Ideally, the experimental noise spectrum would be measured by setting the sampling and prepulse delays to coincide with the THz probe peak and look at small fluctuations in the peak dt signal as a function of the chopping frequency. Initially this was attempted, but small fluctuations in the path length on hour time scales proved to be a bigger source of noise than any chopping-frequency dependent noise spike encountered in the lab. Therefore, the prepulse was delayed until after the arrival of the THz probe. From the perspective of the signal, this is equivalent to turning off the prepulse beam, however it leaves the possibility of detecting scattered pump light, a strong potential noise source.

To measure the noise spectrum the chopping frequency was scanned in 25Hz steps from 50Hz to the chopper limit, 3700Hz. At each frequency step, 10 seconds of data was taken after an appropriate settling period and a 10 ms lockin time constant. The noise is then Fourier transformed and the frequency-frequency spectrogram is shown in the top panel of Figure D.1. An ideal monochromatic noise source, will appear as a DC signal when its frequency coincides with the chopping frequency. As the chopping frequency is shifted slightly lower or higher, the offset shifts the noise higher in the demodulated spectrum, giving rise to a sharp ‘V’ appearance in the spectrogram (for example 1.3 kHz). As the noise spike bandwidth increases, the V shape becomes less distinct (1.8 kHz).

From the spectrogram, we can numerically calculate the effective noise floor at reduced lockin bandwidths. In the lower panel, the noise floor for an ideal 0.1 s and 1 s

time constant is shown. As indicated, there is a large low noise region between 1000 Hz and 1300 Hz. While the noise is slightly lower in other regions, the close proximity to strong noise spikes means that any small drift in the chopping frequency can result in drastic changes to the system noise.

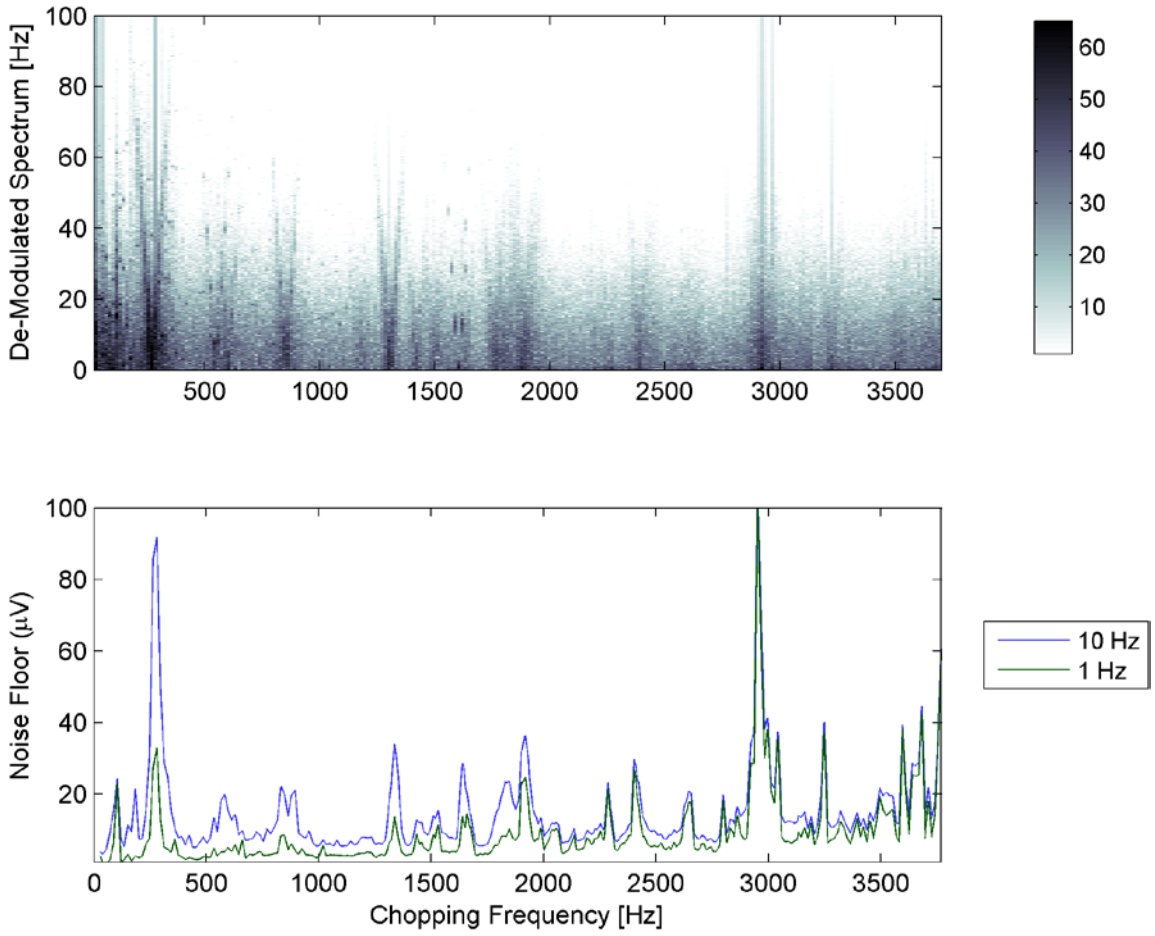

Figure D.1 Noise Floor of the optical pump, THz probe system.

Appendix E
Effect of Purge Box Enclosure

Often, when comparing different time domain THz generation schemes, one is tempted to examine the trailing edge of the THz pulse to look for signs of excessive ringing. Sometimes the ringing originates from dispersion and phonon resonances within the optical crystal, such as in ZnTe shown in Figure 2.2. Other times the ringing can originate from other fundamental physical processes, such as the potential space charge effects in graphene (Figure 4.5). However if the experimental setup contains long (>10 cm) free space paths in atmosphere, the ringing more likely originates from the more mundane reason, water vapor absorption.

As mentioned in Chapter 3, one of the initial THz experiments on graphene was to hunt for a bandgap opening. Phenomenologically, we were looking for a nonuniformity in the graphene transmission spectrum, or the appearance of ringing after the main pulse. Due to the weak interaction of few layer graphene samples (N ~3 to 5) measurements of the transmission spectrum required significant signal averaging. Over the course of an evening, ringing would appear and fade from data traces, without any correlation to experimental parameters. Eventually the ringing was isolated as humidity fluctuations and absorption at water vapor lines.

To minimize the effects of humidity fluctuations, a dry nitrogen purge box was built around the setup, and the effects of a reduction in the relative humidity at 70F, as shown in Figure E.1. As can be seen in the expanded view, the ringing is drastically reduced by removing moisture from the air. Spectrally, the complicated time domain ringing is the interference between a few discrete absorption lines.

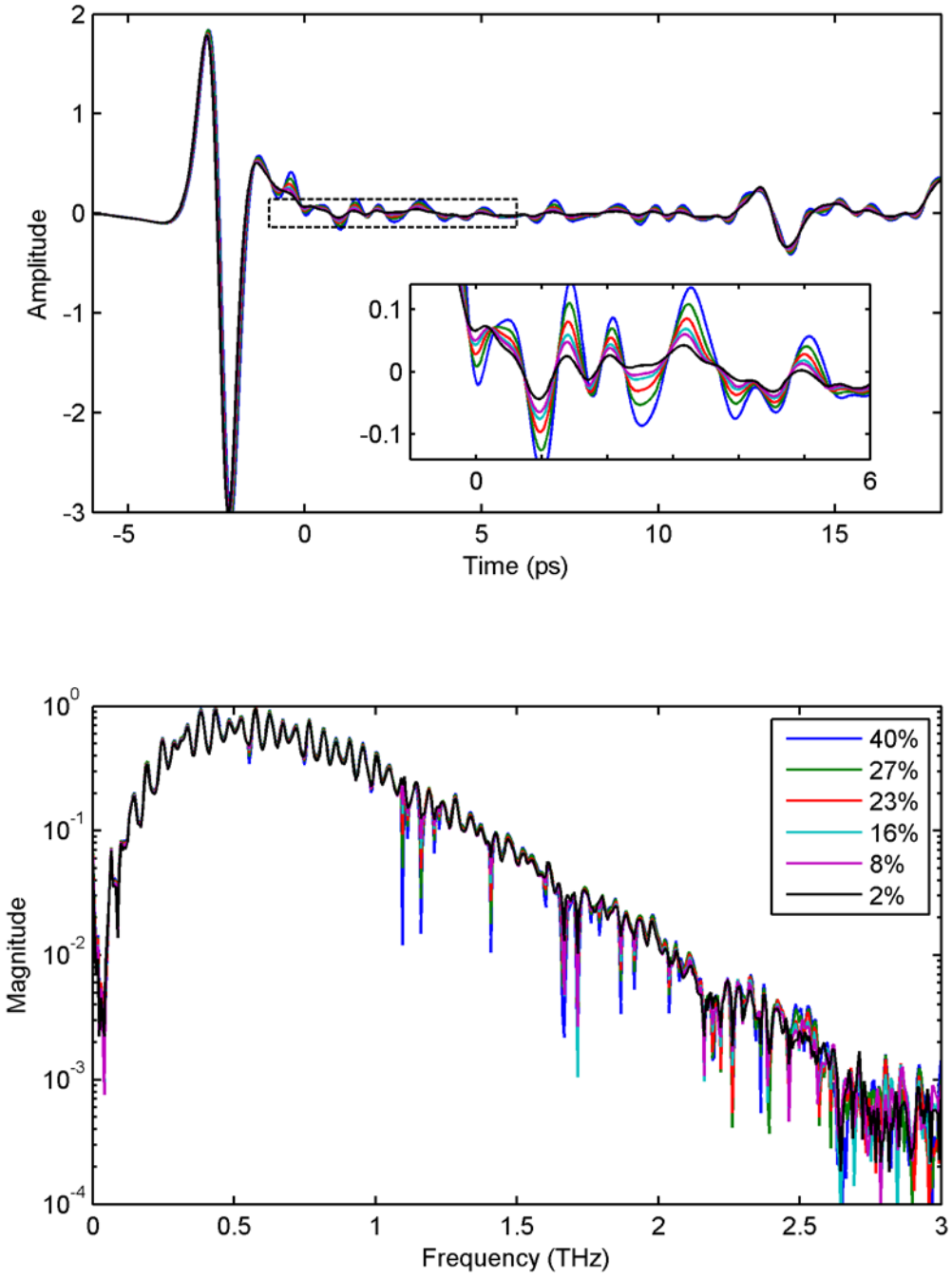

Figure E.1 shows the effect of a humidity enclosure on the THz waveform. The room temperature relative humidity was measured using a portable RH83 Hygrometer on loan from John Whitaker.

Appendix F
CaF_2 Phase Delay

In this section we derive the phase delay due to a tilted CaF_2 window. As shown in Figure F.1, the following relationships are defined as

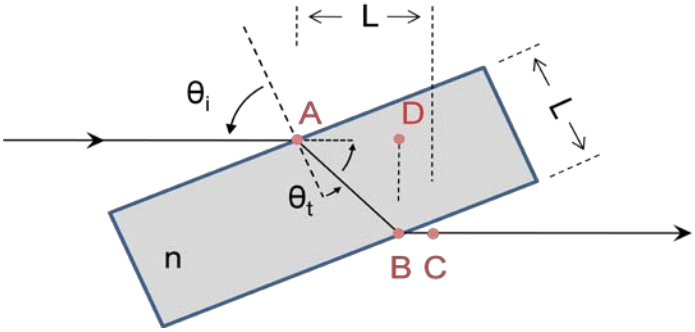

Figure F.1 shows a diagram for calculating the phase delay due to a tilted window

$$\begin{aligned} \theta_t &= \sin^{-1}\left(\frac{\sin\theta_i}{n}\right) \\ \overline{AB} &= L/\cos(\theta_t) \\ \overline{AD} &= \overline{AB}\cdot\cos(\theta_i-\theta_t) \\ \overline{BC} &= L-\overline{AD} \end{aligned} \tag{F.1}$$

With these definitions, the change in path length, $\Delta P.L.$, and the change in phase, $\Delta\Phi$, due to the CaF_2 window can be defined as:

$$\begin{aligned} \Delta \mathrm{P.L.} &= \mathrm{n}\cdot\overline{AB}+\overline{BC}-L \\ &= L\left(\sqrt{n^2-1+\cos^2(\theta_i)}-\cos\theta_i\right) \\ \Delta\Phi(\omega,\theta_i) &= \left(\frac{\omega}{c}\right)(\Delta P.L.) \end{aligned} \tag{F.2}$$

The round trip coherent control phase is then,

$$\begin{aligned} \Delta\Phi_{\mathrm{RT}} &= 2*(2\Phi_1-\Phi_2) \\ &= \left(\frac{4\omega L}{c}\right)\left(\sqrt{n_1^2-1+\cos^2\theta_i}-\sqrt{n_2^2-1+\cos^2\theta_i}\right) \end{aligned} \tag{F.3}$$

where ω is the fundamental frequency, and n_1 and n_2 are the phase index at the fundamental and second harmonic frequencies.

Appendix G
Measurement of the DFG Pump Size

In the coherent control experiment, the large polarization angle error (33°) and the unusual time-phase results at 4.8 µm inspired us to measure the beam profile beyond a simple knife edge experiment. Using a method similar to the THz spot measurement in Appendix B, a 100 µm pinhole was fixed to the front of the cooled MCT detector and the entire unit was scanned across the beam profile with a 150 µm step size. The profile was measured 10 cm from the exit port of the DFG and the original cross section is shown in the left panel of Figure G.1. The measured profile shows signs of significant coma, which is indicative of a misaligned paraboloidal reflector. We attempted to measure the spot farther from the DFG; however the spatial wings of the beam quickly extended past the range of our detection window. After removing the original mount and reversing the orientation of the collimating paraboloid, most of the aberrations disappeared, as shown in the right panel.

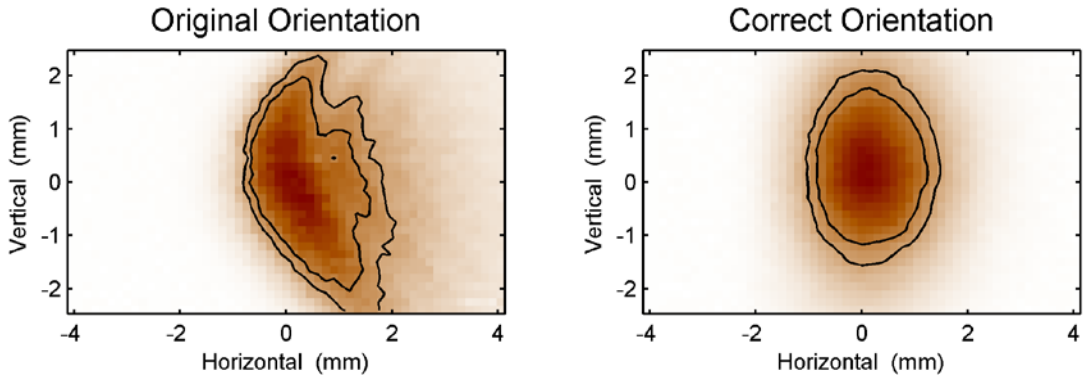

Figure G.1 shows the DFG beam cross section at 6.1 µm. The left panel shows the beam profile used during the coherent control experiments and the right panel shows the profile after reversing the collimation parabola. The contour lines show the half max and 1/e diameters.

Bibliography

1. Communications, L. *Automated Explosvies Detectors, TSA-Certified EDS, Advanced Technology - L3 Communications*. 2009 [cited 2009 April 15, 2009]; Available from: http://www.dsxray.com/products/mmwave.htm.
2. TSA. *TSA: Millimeter Wave*. 2009 [cited 2009 April 15, 2009]; Available from: http://www.tsa.gov/approach/tech/mwave.shtm.
3. Stahl, L., *60 Minutes: Are Our Airports Safer?*, in *60 Minutes*. 2008, CBS. p. 45:00.
4. Sughrue, K. *Anatomy Of An Uproar: What's The Big Deal*. 2008 [cited 2009 April 15, 2009]; Available from: http://www.cbsnews.com/stories/2008/12/23/60minutes/main4684318.shtml.
5. Cai, Y., et al., *Coherent terahertz radiation detection: Direct comparison between free-space electro-optic sampling and antenna detection.* Applied Physics Letters, 1998. **73**(4): p. 444-446.
6. Hussain, A., et al., *Dynamic range of ultrabroadband terahertz detection using GaAs photoconductors.* Applied Physics Letters, 2006. **88**(14).
7. Grossman, E., et al. *Terahertz Imaging and Security Applications*. in *APS March Meeting*. 2005.
8. Balandin, A.A., et al., *Superior Thermal Conductivity of Single-Layer Graphene.* Nano Letters, 2008. **8**(3): p. 902-907.
9. Areshkin, D.A., et al., *Ballistic Transport in Graphene Nanostrips in the Presence of Disorder: Importance of Edge Effects.* Nano Letters, 2007. **7**(1): p. 204-210.
10. Berger, C., et al., *Ultrathin Epitaxial Graphite: 2D Electron Gas Properties and a Route toward Graphene-based Nanoelectronics.* The Journal of Physical Chemistry B, 2004. **108**(52): p. 19912-19916.
11. Ryzhii, V., et al., *Negative dynamic conductivity of graphene with optical pumping.* Journal of Applied Physics, 2007. **101**(8).
12. Franken, P.A., et al., *Generation of Optical Harmonics.* Physical Review Letters, 1961. **7**(4): p. 118.
13. Bass, M., et al., *Optical Rectification.* Physical Review Letters, 1962. **9**(11): p. 446.
14. Yang, K.H., et al., *Generation of Far-Infrared Radiation by Picosecond Light Pulses in LiNbO[sub 3]*. Applied Physics Letters, 1971. **19**(9): p. 320-323.
15. Auston, D.H., et al., *Cherenkov Radiation from Femtosecond Optical Pulses in Electro-Optic Media.* Physical Review Letters, 1984. **53**(16): p. 1555.
16. van Exter, M., et al., *High-brightness terahertz beams characterized with an ultrafast detector.* Applied Physics Letters, 1989. **55**(4): p. 337-339.
17. Katzenellenbogen, N., et al., *Efficient generation of 380 fs pulses of THz radiation by ultrafast laser pulse excitation of a biased metal-semiconductor interface.* Applied Physics Letters, 1991. **58**(3): p. 222-224.
18. Ohtake, H., et al. *Intense THz-radiation generation from an intracavity saturable Bragg reflector in a magnetic field*. in *Lasers and Electro-Optics, 1998. CLEO 98. Technical Digest. Summaries of papers presented at the Conference on*. 1998.

19. You, D., et al., *Generation of high-power sub-single-cycle 500-fs electromagnetic pulses.* Opt. Lett., 1993. **18**(4): p. 290.
20. Löffler, T., et al., *Large-area electro-optic ZnTe terahertz emitters.* Opt. Express, 2005. **13**(14): p. 5353-5362.
21. Verghese, S., et al., *Highly tunable fiber-coupled photomixers with coherent terahertz output power.* Microwave Theory and Techniques, IEEE Transactions on, 1997. **45**(8): p. 1301-1309.
22. Stepanov, A., et al., *Scaling up the energy of THz pulses created by optical rectification.* Opt. Express, 2005. **13**(15): p. 5762-5768.
23. Yeh, K.L., et al., *Generation of 10 uJ ultrashort terahertz pulses by optical rectification.* Applied Physics Letters. **90**: p. 171121.
24. Blanchard, F., et al., *Generation of 1.5 ÂµJ single-cycle terahertz pulses by optical rectification from a large aperture ZnTe crystal.* Opt. Express, 2007. **15**(20): p. 13212-13220.
25. Chang, G., et al., *Power scalable compact THz system based on an ultrafast Yb-doped fiber amplifier.* Optics Express, 2006. **14**(17): p. 7909-7913.
26. Hebling, J.n., et al., *Generation of high-power terahertz pulses by tilted-pulse-front excitation and their application possibilities.* J. Opt. Soc. Am. B, 2008. **25**(7): p. B6-B19.
27. Wallace, P.R., *The Band Theory of Graphite.* Physical Review, 1947. **71**(9): p. 622.
28. Neto, C., et al., *The electronic properties of graphene.* Reviews of Modern Physics, 2009. **81**(1).
29. Novoselov, K.S., et al., *Two-dimensional gas of massless Dirac fermions in graphene.* Nature, 2005. **438**(7065): p. 197-200.
30. Novoselov, K.S., et al., *Electric Field Effect in Atomically Thin Carbon Films.* Science, 2004. **306**(5696): p. 666-669.
31. Lemme, M.C., et al., *A Graphene Field-Effect Device.* IEEE Electron Device Letters, 2007. **28**: p. 282-284.
32. Zhang, Y., et al., *Experimental observation of the quantum Hall effect and Berry's phase in graphene.* Nature, 2005. **438**: p. 201-204.
33. Ossipov, A., et al., *Reentrance effect in a graphene n-p-n junction coupled to a superconductor.* Physical Review B, 2007. **75**: p. 241401.
34. Gusynin, V.P., et al., *Unusual Microwave Response of Dirac Quasiparticles in Graphene.* Physical Review Letters, 2006. **96**(25).
35. Seoánez, C., et al., *Dissipation in graphene and nanotube resonators.* Physical Review B, 2007. **76**: p. 125427.
36. Han, M.Y., et al., *Energy Band-Gap Engineering of Graphene Nanoribbons.* Physical Review Letters, 2007. **98**: p. 206805.
37. Brey, L., et al., *Electronic states of graphene nanoribbons studied with the Dirac equation.* Physical Review B, 2006. **73**: p. 235411.
38. Dresselhaus, M.S., et al., *Intercalation compounds of graphite.* Advances in Physics, 2002. **51**(1): p. 1-186.
39. Simpson, C., et al., *Synthesis of a Giant 222 Carbon Graphite Sheet.* Chemistry - A European Journal, 2002. **8**(6): p. 1424-1429.

40. Reina, A., et al., *Large Area, Few-Layer Graphene Films on Arbitrary Substrates by Chemical Vapor Deposition.* Nano Letters, 2009. **9**(1): p. 30-35.
41. Gomez De Arco, L., et al., *Synthesis, Transfer, and Devices of Single- and Few-Layer Graphene by Chemical Vapor Deposition.* Nanotechnology, IEEE Transactions on, 2009. **8**(2): p. 135-138.
42. Campos-Delgado, J., et al., *Bulk Production of a New Form of sp2 Carbon: Crystalline Graphene Nanoribbons.* Nano Letters, 2008. **8**(9): p. 2773-2778.
43. De Arco, L.G., et al., *Synthesis, Transfer, and Devices of Single- and Few-Layer Graphene by Chemical Vapor Deposition.* Nanotechnology, IEEE Transactions on, 2009. **8**(2): p. 135-138.
44. Shelton, J., *Equilibrium segregation of carbon to a nickel (111) surface: A surface phase transition.* Surface Science, 1974. **43**: p. 493-520.
45. Eizenberg, M., *Carbon monolayer phase condensation on Ni(111).* Surface Science, 1979. **82**: p. 228-236.
46. Nagashima, A., et al., *Electronic states of monolayer graphite formed on TiC(111) surface.* Surface Science, 1993. **291**(1-2): p. 93-98.
47. Van Bommel, A.J., et al., *LEED and Auger electron observations of the SiC(0001) surface.* Surface Science, 1975. **48**(2): p. 463-472.
48. de Heer, W.A., et al., *Epitaxial graphene.* Solid State Communications, 2007. **143**: p. 92-100.
49. Hass, J., et al., *Interface structure of epitaxial graphene grown on 4H-SiC(0001).* Phys. Rev. B, 2008. **78**(20): p. 205424-10.
50. Hass, J., et al., *Why Multilayer Graphene on 4H-SiC(000[overline 1]) Behaves Like a Single Sheet of Graphene.* Physical Review Letters, 2008. **100**(12): p. 125504-4.
51. Ohta, T., et al., *Controlling the Electronic Structure of Bilayer Graphene.* Science, 2006. **313**(5789): p. 951-954.
52. Varchon, F., et al., *Electronic Structure of Epitaxial Graphene Layers on SiC: Effect of the Substrate.* Physical Review Letters, 2007. **99**(12): p. 126805.
53. Berger, C., et al., *Electronic Confinement and Coherence in Patterned Epitaxial Graphene.* Science, 2006. **312**(5777): p. 1191-1196.
54. Sadowski, M.L., et al., *Magnetospectroscopy of epitaxial few-layer graphene.* Solid State Communications, 2007. **143**(1-2): p. 123-125.
55. Sadowski, M.L., et al., *Landau Level Spectroscopy of Ultrathin Graphite Layers.* Physical Review Letters, 2006. **97**(26): p. 266405.
56. Chan, W., et al., *Imaging with terahertz radiation.* Reports on Progress in Physics, 2007. **70**(8): p. 1325-1379.
57. Woolard, D.L., et al., *Terahertz Frequency Sensing and Imaging: A Time of Reckoning Future Applications?* Proceedings of the IEEE, 2005. **93**(10): p. 1722-1743.
58. Han, P.Y., et al., *A direct comparison between terahertz time-domain spectroscopy and far-infrared Fourier transform spectroscopy.* Journal of Applied Physics, 2001. **89**(4): p. 2357-2359.
59. Nagai, M., et al., *Generation and detection of terahertz radiation by electro-optical process in GaAs using 1.56 mu m fiber laser pulses.* Applied Physics Letters, 2004. **85**(18): p. 3974-3976.

60. Imeshev, G., et al., *High-power source of THz radiation based on orientation-patterned GaAs pumped by a fiber laser.* Opt. Express, 2006. **14**(10): p. 4439-4444.
61. Matthäus, G., et al., *Surface-emitted THz generation using a compact ultrashort pulse fiber amplifier at 1060nm.* Optics Communications, 2006. **261**(1): p. 114-117.
62. Schneider, A., et al., *High efficiency generation and detection of terahertz pulses using laser pulses at telecommunication wavelengths.* Opt. Express, 2006. **14**(12): p. 5376-5384.
63. Chang, G., et al., *Generation of radially polarized terahertz pulses via velocity-mismatched optical rectification.* Optics Letters, 2007. **32**(4): p. 433-435.
64. Syouji, A., et al., *Evaluation of a terahertz wave spectrum and construction of a terahertz wave-sensing system using a Yb-doped fiber laser.* Journal of the Optical Society of America B, 2007. **24**(8): p. 2006-2012.
65. Planken, P.C.M., et al., *Measurement and calculation of the orientation dependence of terahertz pulse detection in ZnTe.* Journal of the Optical Society of America B: Optical Physics, Volume 18, Issue 3, March 2001, pp.313-317, 2001. **18**: p. 313-317.
66. Wahlstrand, J., et al., *Coherent phonon-polaritons and subluminal Cherenkov radiation.* Physica B: Condensed Matter, 2002. **316-317**: p. 55-61.
67. Shoji, I., et al., *Absolute scale of second-order nonlinear-optical coefficients.* J. Opt. Soc. Am. B, 1997. **14**(9): p. 2268-2294.
68. Ding, Y.J., *Quasi-single-cycle terahertz pulses based on broadband-phase-matched difference-frequency generation in second-order nonlinear medium: high output powers and conversion efficiencies.* Selected Topics in Quantum Electronics, IEEE Journal of, 2004. **10**(5): p. 1171-1179.
69. Palik, E., *Handbook of optical constants of solids II*. 1991: Academic Press.
70. Xu, J.Z., et al., *Optical rectification in an area with a diameter comparable to or smaller than the center wavelength of terahertz radiation.* Optics Letters, 2002. **27**: p. 1067-1069.
71. Nishizawa, J.I., et al., *THz Generation From GaP Rod-Type Waveguides.* Photonics Technology Letters, IEEE, 2007. **19**(3): p. 143-145.
72. Wu, Q., et al., *7 terahertz broadband GaP electro-optic sensor.* Applied Physics Letters, 1997. **70**(14): p. 1784-1786.
73. Zhu, Z., et al., *Full-vectorial finite-difference analysis of microstructured optical fibers.* Opt. Express, 2002. **10**(17): p. 853-864.
74. Fermann, M.E., et al., *Self-Similar Propagation and Amplification of Parabolic Pulses in Optical Fibers.* Physical Review Letters, 2000. **84**(26): p. 6010.
75. Bitzer, A., et al., *Beam-Profiling and Wavefront-Sensing of THz Pulses at the Focus of a Substrate-Lens.* Selected Topics in Quantum Electronics, IEEE Journal of, 2008. **14**(2): p. 476-481.
76. Howard, J., *Imaging properties of off-axis parabolic mirrors.* Appl. Opt., 1979. **18**(15): p. 2714-2722.
77. Newson, R.W., et al., *Coherently Controlled Ballistic Charge Currents Injected in Single-Walled Carbon Nanotubes and Graphite.* Nano Letters, 2008. **8**(6): p. 1586-1589.

78. Boyle, W.S., et al., *Band structure and infrared absorption of graphite.* Physical Review, 1958. **3**(3): p. 782-785.
79. Jackson, J.B., et al., *Terahertz imaging for non-destructive evaluation of mural paintings.* Optics Communications, 2008. **281**(4): p. 527-532.
80. Falkovsky, L.A., et al., *Space-time dispersion of graphene conductivity.* The European Physical Journal B - Condensed Matter and Complex Systems, 2007. **56**(4): p. 281-284.
81. Falkovsky, L.A., et al., *Optical far-infrared properties of a graphene monolayer and multilayer.* Physical Review B (Condensed Matter and Materials Physics), 2007. **76**(15).
82. Gusynin, V.P., et al., *Transport of Dirac quasiparticles in graphene: Hall and optical conductivities.* Physical Review B (Condensed Matter and Materials Physics), 2006. **73**(24).
83. Gusynin, V.P., et al., *Anomalous Absorption Line in the Magneto-Optical Response of Graphene.* Physical Review Letters, 2007. **98**(15): p. 157402-4.
84. Gusynin, V.P., et al., *Sum rules for the optical and Hall conductivity in graphene.* Physical Review B (Condensed Matter and Materials Physics), 2007. **75**(16): p. 165407-12.
85. Gusynin, V.P., et al., *AC Conductivity Of Graphene: From Tight -Binding Model To 2 + 1-Dimensional Quantum Electrodynamics.* International Journal of Modern Physics B, 2007. **21**(27): p. 4611-4658.
86. Choi, H., et al., *Broadband electromagnetic response and ultrafast dynamics of few-layer epitaxial graphene.* Applied Physics Letters, 2009. **94**(17): p. 172102-3.
87. Stauber, T., et al., *Optical conductivity of graphene in the visible region of the spectrum.* Physical Review B (Condensed Matter and Materials Physics), 2008. **78**(8): p. 085432-8.
88. Dawlaty, J.M., et al., *Measurement of ultrafast carrier dynamics in epitaxial graphene.* Applied Physics Letters, 2008. **92**(4): p. 042116.
89. Sun, D., et al., *Ultrafast Relaxation of Excited Dirac Fermions in Epitaxial Graphene Using Optical Differential Transmission Spectroscopy.* Physical Review Letters, 2008. **101**(15).
90. Bistritzer, R., et al., *Electronic Cooling in Graphene.* Physical Review Letters, 2009. **102**(20): p. 206410-4.
91. Rana, F., *Electron-hole generation and recombination rates for Coulomb scattering in graphene.* Physical Review B (Condensed Matter and Materials Physics), 2007. **76**(15): p. 155431-5.
92. Rana, F., et al., *Carrier recombination and generation rates for intravalley and intervalley phonon scattering in graphene.* Physical Review B (Condensed Matter and Materials Physics), 2009. **79**(11): p. 115447-5.
93. Butscher, S., et al., *Hot electron relaxation and phonon dynamics in graphene.* Applied Physics Letters, 2007. **91**(20): p. 203103-3.
94. Hanno. 2009.
95. Hanson, G.W., *Dyadic Green's functions and guided surface waves for a surface conductivity model of graphene.* Journal of Applied Physics, 2008. **103**(6): p. 064302.

96. Nuss, M., et al., *Terahertz surface impedance of thin YBa[sub 2]Cu[sub 3]O[sub 7] superconducting films.* Applied Physics Letters, 1991. **58**(22): p. 2561-2563.
97. Dawlaty, J.M., et al. *Measurement of the Optical Properties of Graphene from THz to Near-IR.* in *Conference on Lasers and Electro-Optics/Quantum Electronics and Laser Science Conference and Photonic Applications Systems Technologies*. 2008: Optical Society of America.
98. George, P.A., et al., *Ultrafast Optical-Pump Terahertz-Probe Spectroscopy of the Carrier Relaxation and Recombination Dynamics in Epitaxial Graphene doi:10.1021/nl8019399.* Nano Letters, 2008. **8**(12): p. 4248-4251.
99. Nair, R.R., et al., *Fine Structure Constant Defines Visual Transparency of Graphene.* Science, 2008. **320**(5881): p. 1308-.
100. Giovannetti, G., et al., *Substrate-induced band gap in graphene on hexagonal boron nitride: Ab initio density functional calculations.* Physical Review B (Condensed Matter and Materials Physics), 2007. **76**(7): p. 073103-4.
101. Peng, X., et al., *Symmetry Breaking Induced Bandgap in Epitaxial Graphene Layers on SiC.* Nano Letters, 2008. **8**(12): p. 4464-4468.
102. Zhou, S.Y., et al., *Substrate-induced bandgap opening in epitaxial graphene.* Nat Mater, 2007. **6**(10): p. 770-775.
103. Zhou, S.Y., et al., *Erattum: Substrate-induced bandgap opening in epitaxial graphene.* Nat Mater, 2007. **6**(11): p. 916-916.
104. Sun, D., in *Physics*. 2009, University of Michigan: Ann Arbor.
105. Takenaka, M., et al., *Simulation study on cascaded terahertz pulse generation in electro-optic crystals.* Optics Express, 2007. **15**(13): p. 8076-8093.
106. Mikhailov, S.A., et al., *Nonlinear electromagnetic response of graphene: frequency multiplication and the self-consistent-field effects.* Journal of Physics: Condensed Matter, 2008. **20**(38): p. 384204.
107. Naftaly, M., et al., *Linearity calibration of amplitude and power measurements in terahertz systems and detectors.* Opt. Lett., 2009. **34**(5): p. 674-676.
108. Siders, C.W., et al., *Generation and characterization of terahertz pulse trains from biased, large-aperture photoconductors.* Optics Letters, 1999. **24**: p. 241-243.
109. Gurevich, G.L., et al., *Measurements of optical phase variations using interfering multiphoton ionization processes.* Sov. Phys. JEPT, 1967. **24**: p. 1012.
110. Jackson, D.J., et al., *Resonance-enhanced multiphoton ionization: Interference effects due to harmonic generation.* Physical Review A, 1983. **28**(2): p. 781.
111. Miller, J.C., et al., *Resonantly Enhanced Multiphoton Ionization and Third-Harmonic Generation in Xenon Gas.* Physical Review Letters, 1980. **45**(2): p. 114.
112. Chen, C., et al., *Interference between optical transitions.* Physical Review Letters, 1990. **64**(5): p. 507.
113. Muller, H.G., et al., *Above-threshold ionisation with a two-colour laser field.* Journal of Physics B, 1990. **23**: p. 2761-2769.
114. Yin, Y.-Y., et al., *Asymmetric photoelectron angular distributions from interfering photoionization processes.* Physical Review Letters, 1992. **69**(16): p. 2353.
115. Wang, F., et al., *Product State Control through Interfering Excitation Routes.* Physical Review Letters, 1996. **77**(12): p. 2416.

116. Brumer, P., et al., Accounts of Chem. Res., 1989. **22**: p. 407.
117. Charron, E., et al., Phys. Rev. Lett., 1993. **71**: p. 692.
118. Krause, J.L., et al., J. Chem. Phys., 1989. **92**: p. 1126.
119. Sheehy, B., et al., Physi. Rev. Lett., 1995. **74**: p. 4799.
120. Shnitman, A., et al., Phys. Rev. Lett., 1996. **76**: p. 2886.
121. Tannor, D.J., et al., Adv. Chem. Phys., 1988. **70**: p. 441.
122. Zhu, L., et al., Science, 1995. **270**: p. 77.
123. Dupont, E., et al., *Phase-Controlled Currents in Semiconductors.* Physical Review Letters, 1995. **74**(18): p. 3596.
124. Atanasov, R., et al., *Coherent Control of Photocurrent Generation in Bulk Semiconductors.* Physical Review Letters, 1996. **76**(10): p. 1703.
125. Hach, A., et al., *Observation of Coherently Controlled Photocurrent in Unbiased, Bulk GaAs.* Physical Review Letters, 1997. **78**(2): p. 306.
126. Costa, L., et al., *All-optical injection of ballistic electrical currents in unbiased silicon.* Nat Phys, 2007. **3**(9): p. 632-635.
127. Mele, E.J., et al., *Coherent control of photocurrents in graphene and carbon nanotubes.* Physical Review B, 2000. **61**(11): p. 7669.
128. Rioux, J., et al., Private Communication, 2008.
129. Tan, Y.W., et al., *Measurement of Scattering Rate and Minimum Conductivity in Graphene.* Physical Review Letters, 2007. **99**(24): p. 246803-4.
130. Auston, D.H., et al., *Topics in Applzed Physics Vol. 60: Ultrashort Laser Pulses and Applications*: Springer-Verlag. 189.
131. Stevens, M.J., et al. *Coherent control of an optically-injected ballistic spin-polarized current in bulk GaAs.* in *Quantum Electronics and Laser Science Conference, 2002. QELS '02. Technical Digest. Summaries of Papers Presented at the*. 2002.
132. Cote, D., et al., *THz emission from coherently controlled photocurrents in GaAs.* Applied Physics Letters, 1999. **75**(25): p. 3959-3961.
133. Stevens, T.E., et al., *Cherenkov radiation at speeds below the light threshold: phonon-assisted phase matching.* Science, 2001. **291**(5504): p. 627-630.
134. Corning. *H0607_CaF2_Product_Sheet.pdf*. [CaF2 Product Sheet] 2003 [cited 2009 April 15, 2009]; Available from: http://www.corning.com/docs/specialtymaterials/pisheets/H0607_CaF2_Product_Sheet.pdf.
135. Wen, H., et al., *Coherent Control of the Polarization of Ultrafast Terahertz Pulses*, in *Conference on Laser and Electrooptics*. 2009, OSA: Baltimore.
136. van Driel, H.M., *Coherence Control of Spin and Charge Currents*, in *Conference on Lasers and Electrooptics*. 2009, OSA: Baltimore.
137. Min, H., et al., *Universal Interband Conductivity in Graphene Multilayers.* 2009.
138. Lee, Y.S., et al., *Generation of narrow-band terahertz radiation via optical rectification of femtosecond pulses in periodically poled lithium niobate.* Applied Physics Letters, 2000. **76**(18): p. 2505-2507.
139. Zhao, G., et al., *Design and performance of a THz emission and detection setup based on a semi-insulating GaAs emitter.* Review of Scientific Instruments, 2002. **73**(4): p. 1715-1719.

140. Vodopyanov, K.L., et al. *Tunable THz source based on frequency conversion in quasi-phase-matched GaAs*. 2006. USA: SPIE - The International Society for Optical Engineering.